

# UNIVERSITÀ DEGLI STUDI DI PAVIA

---

Facoltà di Scienze MM. FF. NN.  
Corso di Laurea Magistrale in Scienze Fisiche

## PROTOTYPE STUDIES OF FIBER CALORIMETRY WITH DUAL-READOUT

Relatore:

**Chiar.mo Prof. Michele Livan**

Candidato:

**Silvia Fracchia**

Correlatore:

**Dott. Silvia Franchino**



There's real poetry in the real world.  
Science is the poetry of reality.

— Richard Dawkins

To see a World in a Grain of Sand  
And a Heaven in a Wild Flower,  
Hold Infinity in the palm of your hand  
And Eternity in an hour.

— William Blake, from "Auguries of Innocence"



## SOMMARIO

Nel corso dello svolgimento del lavoro finalizzato alla stesura della mia tesi di laurea magistrale ho partecipato alle attività della Collaborazione DREAM, nell'ambito dell'esperimento R&D 52 del CERN. Quest'ultimo è un esperimento di "Ricerca e Sviluppo", finalizzato alla progettazione e alla costruzione di un nuovo prototipo di calorimetro adronico.

La calorimetria riveste un ruolo fondamentale nei moderni esperimenti di fisica delle alte energie. Il principio base con cui operano i calorimetri è l'assorbimento dell'energia delle particelle che lo attraversano, le quali danno luogo a cascate adroniche ed elettromagnetiche.

Le prestazioni dei calorimetri risultano tuttavia essere limitate da una serie di fattori intrinseci. In particolare, nel caso dei calorimetri adronici, il fenomeno dell'*energia invisibile* e la produzione di mesoni  $\pi^0$  nelle cascate adroniche influenzano fortemente la risoluzione e la linearità della risposta calorimetrica.

Il primo fenomeno consiste nel rilascio di nucleoni nel corso delle reazioni nucleari indotte dalle particelle dello sciame adronico. L'energia utilizzata per liberare i nucleoni non va quindi a contribuire al segnale calorimetrico e per questo motivo è detta *invisibile*. Le fluttuazioni nell'energia invisibile rappresentano il limite ultimo alla risoluzione energetica ottenibile con i calorimetri adronici.

I  $\pi^0$  prodotti nelle cascate adroniche danno origine a sciame elettromagnetici, a causa del loro decadimento in due  $\gamma$ . Ogni cascata adronica possiede pertanto una componente elettromagnetica, la quale trasporta una frazione dell'energia dello sciame. Questa frazione elettromagnetica dipende dall'energia dello sciame adronico e proprio a causa di questa dipendenza i calorimetri risultano essere non lineari per la rivelazione degli adroni.

Il metodo a *doppia lettura* si propone di ottimizzare la risoluzione dei calorimetri adronici mediante la misurazione della frazione elettromagnetica evento per evento. Questo metodo si basa sulla rivelazione simultanea della luce Cherenkov e della luce di scintillazione prodotte dalle particelle che attraversano il calorimetro. La luce Cherenkov, infatti, è quasi esclusivamente prodotta dalla componente elettromagnetica della cascata adronica, poiché gli elettroni e i positroni che la compongono sono relativistici fino a circa 0.2 MeV, mentre i protoni di spallazione responsabili della componente non elettromagnetica del segnale sono tipicamente non relativistici.

Nella mia tesi, dapprima mi focalizzo sugli aspetti fisici generali necessari alla comprensione delle funzionalità dei calorimetri, descrivendo i meccanismi di interazione delle particelle con la materia, la risposta energetica dei calorimetri e le fluttuazioni nei processi di deposito di energia.

Il capitolo successivo è dedicato alla presentazione del metodo a doppia lettura. In particolare, l'esperimento DREAM viene descritto approfonditamente, dalla sua nascita fino agli sviluppi odierni. Vengono presentati i principali risultati ottenuti con il primo calorimetro di rame e fibre, nonché quelli ottenuti utilizzando cristalli di diversi tipi.

Il terzo e il quarto capitolo della mia tesi sono dedicati alla presentazione del lavoro da me svolto nell'ambito della Collaborazione DREAM su due fronti: l'analisi dei dati ottenuti dal test di un prototipo di calorimetro di piombo e fibre, costruito a Pavia nel 2011, nonché la partecipazione alla costruzione di alcuni moduli di piombo e fibre avvenuta a Pavia a partire dall'inizio del 2012.

I dati che ho analizzato sono stati raccolti durante due periodi di test su fascio (avvenuti nel novembre 2011 e nel luglio 2012) effettuati presso la linea H8 del Super Proton Synchrotron (SPS) del CERN. Durante i test su fascio, le prestazioni del modulo NewDREAM sono state studiate per mezzo di fasci di elettroni e pioni di energia nota.

L'analisi dei dati è stata effettuata mediante l'utilizzo del software ROOT.

Ho partecipato attivamente al periodo di test avvenuto nel luglio 2012, collaborando alla presa dati.

Ho inoltre collaborato con il personale tecnico dell'INFN di Pavia, partecipando alle attività di costruzione di alcuni moduli di piombo e fibre iniziate nei primi mesi del 2012. Il terzo capitolo della mia tesi è dedicato alla descrizione delle varie fasi dell'assemblaggio dei moduli, nonché delle caratteristiche dei materiali utilizzati e delle motivazioni che hanno portato alla loro scelta. Vengono inoltre presentate alcune idee in corso di sviluppo per l'ottimizzazione della lettura del segnale dei moduli.

# CONTENTS

1	CALORIMETRY IN HIGH-ENERGY PHYSICS	5
1.1	Brief history of calorimetry	5
1.2	Detection mechanisms	7
1.2.1	Ionization	7
1.2.2	Bremsstrahlung	10
1.2.3	Cherenkov radiation	11
1.2.4	Scintillation	12
1.3	Photon interactions	13
1.3.1	Photoelectric effect	13
1.3.2	Rayleigh scattering	13
1.3.3	Compton scattering	14
1.3.4	Pair production	15
1.4	The physics of shower development	17
1.4.1	Electromagnetic showers	18
1.4.2	Hadronic showers	25
1.5	The energy response of calorimeters	35
1.5.1	Non-linearity for electromagnetic showers	36
1.5.2	Homogeneous calorimeters	37
1.5.3	Sampling calorimeters	40
1.5.4	Compensation	43
1.6	Fluctuations	46
1.6.1	Signal quantum fluctuations	48
1.6.2	Sampling fluctuations	49
1.6.3	Instrumental effects	50
1.6.4	Shower leakage	52
1.6.5	Fluctuations in hadronic showers	53
1.6.6	The shape of the response function	54
1.7	Summary	55
2	THE DREAM PROJECT	57
2.1	New approaches to calorimetry	57
2.1.1	The energy flow method	57
2.1.2	Dual-readout calorimetry	58
2.2	The dual-readout method	58
2.2.1	The DREAM detector	58
2.2.2	Dual-readout with crystals	69
2.2.3	The NewDREAM module	80
3	CONSTRUCTION OF LEAD/FIBERS MODULES	81
3.1	Choice of materials	81
3.1.1	Lead plates	82
3.1.2	Fibers	84
3.2	Construction	86
3.2.1	Thickness non-uniformity of lead layers	90

## CONTENTS

3.2.2	Differences in energy resolution	92
3.3	Readout	94
3.3.1	Ideas for readout optimization	96
4	DATA ANALYSIS ON NEWDREAM LEAD MODULE	99
4.1	October/November 2011 testbeam	99
4.1.1	The H8 beamline	99
4.1.2	Experimental setup	100
4.1.3	Data analysis	103
4.2	July 2012 testbeam	116
4.2.1	Module readout	116
4.2.2	Data analysis	117
5	CONCLUSIONS	133

## LIST OF FIGURES

- Figure 1 The stopping power  $dE/dx$  as a function of energy for different particles. [2] 9
- Figure 2 Cross section for the photoelectric effect as a function of the  $Z$  value of the absorber (data for 100 keV and 1 MeV  $\gamma$ s). [1] 14
- Figure 3 Cross section the Compton scattering as a function of the  $Z$  value of the absorber, for  $\gamma$ s of 0.1 and 1.0 MeV. [1] 15
- Figure 4 Cross section for the processes through which the particles composing electromagnetic showers lose their energy, in various absorber materials. 16
- Figure 5 The energy domains in which photoelectric effect, Compton scattering and pair production are the most likely processes to occur, as a function of the  $Z$  value of the absorber material. [1] 17
- Figure 6 The energy deposit as a function of depth, for 1, 10, 100 and 1000 GeV electron showers developing in a block of copper. 19
- Figure 7 The composition of em showers. 19
- Figure 8 Comparison of the longitudinal ( $a$ ) and lateral ( $b$ ) profiles of the energy deposited by electrons and positrons in 10 GeV em showers developing in lead. 20
- Figure 9 Energy deposit as a function of depth, for 10 GeV electron showers developing in aluminium, iron and lead, showing approximate scaling of the longitudinal shower profile, when expressed in units of radiation length,  $X_0$ . Results of EGS4 calculations. [1] 22
- Figure 10 Radial energy deposit profiles for 10 GeV electrons showering in aluminium, copper and lead. Results of EGS4 calculations. [1] 23
- Figure 11 Average energy fraction contained in a block of matter with infinite transverse dimensions, as a function of the thickness of this absorber. 24
- Figure 12 The average em shower fraction in pion-induced showers measured in the SPACAL lead/fiber calorimeter. 28

## List of Figures

- Figure 13 Cross sections for nuclides produced by spallation of  $^{238}\text{U}$ , induced by a 2 GeV hadron. [30] 30
- Figure 14 Signal distributions for 75 GeV  $\pi^-$  and  $e^-$  in a very simple preshower detector. [5] 33
- Figure 15 Average lateral profile of the energy deposited by 80 GeV  $\pi^-$  showering in the SPACAL detector. 33
- Figure 16 Lateral profiles for pion-induced showers, measured at different depths, with the ZEUS calorimeter. Data from [7]. 34
- Figure 17 Longitudinal profiles for 4 different showers induced by 270 GeV pions in a lead/iron/plastic-scintillator calorimeter. Data from [6]. 35
- Figure 18 The em calorimeter response as a function of energy, measured with the QFCAL calorimeter, before (a) and after (b) precautions were taken against PMT saturation effects. Data from [21]. 36
- Figure 19 The relation between the calorimeter response ratio to em and non-em energy deposition,  $e/h$ , and the measured  $e/\pi$  signal ratios. [1] 39
- Figure 20 The  $e/mip$  ratio as a function of the thickness of the absorber layers, for uranium/PMMA and uranium/LAr calorimeters. 41
- Figure 21 The calculated response of iron/LAr and lead-/LAr calorimeters to pions, as a function of energy. [1] 43
- Figure 22 Pion/electron response ratio as a function of the hydrogen content of the gas mixture. [10] 45
- Figure 23 Typical signals for 150 GeV electrons (a) and pions (b) measured with the SPACAL calorimeter. 45
- Figure 24 The em energy resolution and the separate contributions to it, for the ATLAS EM calorimeter. [20] 47
- Figure 25 The energy resolution for electron detection with the QFCAL prototype detector, as a function of energy. 48
- Figure 26 The em energy resolution of sampling calorimeters as a function of the parameter  $(d/f_{\text{samp}})^{1/2}$ . [22] 49
- Figure 27 The em energy resolution (see right scale) as a function of the sampling fraction for various representative plastic-scintillator calorimeters (a) or for scintillating-fiber calorimeters (b). [22] 50

- Figure 28 Lateral cross section of SPACAL (a). The SPACAL signal as a function of the  $y$ -coordinate of the impact point (b). Data for 80 GeV electrons. [23] 51
- Figure 29 The effects of longitudinal and lateral shower leakage on the energy resolution, as measured for 15 GeV electrons (a) and pions (b) by the CHARM Collaboration in a low- $Z$  calorimeter. [24, 25] 52
- Figure 30 A comparison of the effects caused by different types of shower leakage. 53
- Figure 31 Signal distributions for 10 GeV (a) and 200 GeV (b) electrons showering in the CMS quartz-fiber calorimeter. 54
- Figure 32 Signal distributions for 300 GeV pions and protons detected with a quartz-fiber calorimeter. 55
- Figure 33 (a) The basic building block of the DREAM calorimeter is a  $4 \times 4$  mm<sup>2</sup> extruded hollow copper rod of 2 meters length, with a 2.5 mm diameter central hole. (b) Layout of the DREAM calorimeter. 59
- Figure 34 Fiber bunches exiting from the rear face of the DREAM calorimeter. 60
- Figure 35 The response for electrons entering the DREAM calorimeter oriented in the tilted position ( $\phi=3^\circ$ ,  $\theta=2^\circ$ ), as a function of energy. 61
- Figure 36 The energy resolution as a function of energy, measured with the scintillating (squares) and the Cherenkov fibers (circles), for electrons entering the calorimeter in the tilted position ( $\phi=3^\circ$ ,  $\theta=2^\circ$ ). [14] 62
- Figure 37 Signal distributions for 100 GeV  $\pi^-$  recorded by the scintillating (a) and Cherenkov (b) fibers of the DREAM calorimeter, oriented in the un-tilted position ( $\phi=2^\circ$ ,  $\theta=0.7^\circ$ ). [15] 63
- Figure 38 Cherenkov signals versus scintillator signals for 100 GeV  $\pi^-$ . [15] 64
- Figure 39 Cherenkov signal distribution for 100 GeV  $\pi^-$  (a) and distributions for subsamples of events selected on the basis of the measured  $f_{em}$  value, using the Q/S method (b). [15] 65
- Figure 40 Signal distributions for high-multiplicity "jets" in DREAM before and after corrections on the basis of the observed Q/S ratio were applied. [5] 66

## List of Figures

- Figure 41 The energy resolution for single pions as a function of energy, before and after corrections made on the basis of the measured Q/S signal ratio (*a*). Comparison of the corrected resolutions for jets and single pions (*b*). [15] 66
- Figure 42 The calorimeter response to single pions and high-multiplicity jets, before and after corrections made on the basis of the measured Q/S signal ratio. [15] 67
- Figure 43 Average time structure of the Cherenkov and scintillation signals recorded for 200 GeV "jets" developing in the DREAM calorimeter. [28] 68
- Figure 44 Scatter plot for 200 GeV "jets". 69
- Figure 45 Experimental setup in which the beam tests of the crystals were performed. 71
- Figure 46 Time structures of the PMT signal from 50 GeV electrons traversing a PbWO<sub>4</sub> crystal at angles  $\theta=30^\circ$  and  $-30^\circ$ , respectively, and the difference between these two time distributions. [17] 72
- Figure 47 Left-right response asymmetry measured for 10 GeV electrons showering in a 2.5 X<sub>0</sub> thick PbWO<sub>4</sub> crystal, as a function of the orientation of the crystal (the angle  $\theta$ ). 73
- Figure 48 Average time structure of the signals from a PbWO<sub>4</sub> crystal doped with 1% of molybdenum, generated by 50 GeV electrons. 74
- Figure 49 Ratio of the signals from the light transmitted by the UV and the yellow filters, as a function of the angle of incidence of the beam particles. 75
- Figure 50 The time structure of a typical 50 GeV electron signal measured in the BGO crystal equipped with a yellow filter (*a*), and with an UV filter (*b*). 76
- Figure 51 The UV BGO signals were used to measure the relative contributions of scintillation light (gate 2) and Cherenkov light (gate 1). 76
- Figure 52 The Cherenkov signal distribution for 200 GeV jet events detected in the BGO/fiber calorimeter system (*a*) together with the distributions for subsets of events selected on the basis of the C/S ratio (*b*). [19] 77
- Figure 53 (*a*) The BGO matrix, consisting of 100 tapered crystals. (*b*) The 0.3% Mo-doped PbWO<sub>4</sub> matrix consisted of 7 crystals with dimensions of  $3 \times 3 \times 20$  cm<sup>3</sup>. 78

Figure 54	Energy resolution for electrons showering in the $\text{PbWO}_4$ crystal matrix, as a function of energy.	79
Figure 55	A 3-dimensional representation of the 3x3 modules matrix, which will be tested in November 2012.	81
Figure 56	A scheme of the extruded profile of lead plates.	82
Figure 57	The fiber pattern used in the modules construction.	83
Figure 58	Comparison of self-absorption of PS and PMMA fibers.	85
Figure 59	Comparison of scintillation and Cherenkov signals obtained from the test of two modules with PS and PMMA fibers, respectively.	86
Figure 60	Detail of the lead reel ( <i>a</i> ), of the cutting of the rolled lead ( <i>b</i> ), of its stretching with the roller ( <i>c</i> ) and of the redefinition of the grooves profile with the comb ( <i>d</i> ).	87
Figure 61	Details of the fixing of the layers during construction: the front end of the module ( <i>a</i> ), the rear end ( <i>b</i> ) and the fiber bunches departing from the rear end ( <i>c</i> ).	88
Figure 62	A picture of the module fixed and pressed by clamps for the night.	88
Figure 63	Detail of the wrapping of the module with the lead tape ( <i>a</i> ) and of its moving from the worktable ( <i>b</i> ). Some completed modules are shown in ( <i>c</i> ).	89
Figure 64	The "S" shape of the lead plates, caused by the non-uniformity of their thickness.	90
Figure 65	The lead plate profile seen with the microscope.	90
Figure 66	Thickness of lead layers as a function of the position on the plate (number from 1 to 5 correspond to a position varying from 0 to 9.3 cm) ( <i>a</i> ). Measurements of different samples of the new layers ( <i>b</i> ), old layers ( <i>c</i> ) and the comparison between their average values ( <i>d</i> ) are shown.	91
Figure 67	A schematic representation of how we calculated $f_{samp}$ ( <i>a</i> ). $t_f$ and $t_p$ indicate the equivalent height of the fibers and the lead layers, respectively. The filling fraction of the fibers ( <i>b</i> ).	93
Figure 68	Fiber bunches departing from the rear end of the module before milling ( <i>a</i> ), after milling ( <i>b</i> ) and their connection to the PMTs.	95

## List of Figures

- Figure 69 A 3-dimensional representation of the mechanical structure used to connect the photomultiplier tubes to the fiber bunches. 96
- Figure 70 The experimental setup used to test the performance of the Pavia NewDREAM module. The figure is not in scale. 100
- Figure 71 Picture of DREAM testbeam area, which is placed downstream the calorimeter. The auxiliary detectors are indicated (the hodoscope wasn't discussed because it wasn't used in this analysis). The beampipe, from which the beam comes, is also visible. 102
- Figure 72 The tower structure of the module and its positioning (a); the scheme of the structure of the Pavia module (b). 103
- Figure 73 Spatial uniformity of a photomultiplier tube. 104
- Figure 74 The four real towers (in red) to be calibrated and the five virtual towers (in white) surrounding them. 105
- Figure 75 ADC counts distribution of the muon counter, the tail catcher and the preshower detector for the 80 GeV electron beam. 107
- Figure 76 The beam profile obtained from DWC<sub>1</sub>, for 30 GeV electrons. 108
- Figure 77 The scatter plot of the Cherenkov ADC counts as a function of the x and y coordinates for the electron beam run of 30 GeV. The cuts applied are marked by the solid lines. The DWC y coordinate is reversed with respect to the module point of view. 108
- Figure 78 Signal distribution of the Cherenkov channels for each electron beam energy, fitted with a Gaussian. 109
- Figure 79 Signal distribution of the scintillation channels for each electron beam energy, fitted with a Gaussian. 110
- Figure 80 The energy resolution for electrons entering in Tower 4 near the center of the Pavia module, as a function of  $1/\sqrt{E}$ . The three diagrams represent the results for Cherenkov (a), scintillation (b) and the sum of all fiber signals (c). The data have been fitted with the relation  $\sigma/E = p_0 + p_1/\sqrt{E}$ . 112
- Figure 81 PMTs linearity for Cherenkov (a) and scintillation (b) signals. 113
- Figure 82 The beam spot subdivision. 114

- Figure 83 The average calorimeter response for all 16 quadrants (blue circles) and for the four central quadrants (red squares), as a function of the electron energy. 114
- Figure 84 The calorimeter response in Tower 4 as a function of the electron energy, for all 16 quadrants. 115
- Figure 85 ADC distribution of the muon counter (*a*) and the preshower detector (*b*) for the run at 10 GeV. 118
- Figure 86 Average pulse shapes of the oscilloscope signals obtained with a 10 GeV electron beam sent in the center of the calorimeter module. Shown are the pulse shapes of Cherenkov and scintillation signals readout by the low gain PMT channels ((*a*) and (*b*)) and by the high gain PMT channels ((*c*) and (*d*)). One may notice that the signal amplitudes for the high gain channels are 10 times those for the low gain channels. 118
- Figure 87 Integral distributions of Cherenkov and scintillation signals obtained with a 10 GeV electron beam sent in the center of the calorimeter module for signals readout by the low gain PMT channels, after the calibration. 119
- Figure 88 Integral distributions of Cherenkov and scintillation pedestal channels obtained with a 4 GeV electron beam sent in the center of the calorimeter module. 119
- Figure 89 Response linearity for Cherenkov signals detected with PMTs equipped with standard bases (*a*), tapered bases (*b*) and tapered bases with an independent voltage generator on the last dynode (*c*). The big error bars for the points at 20 GeV in (*b*) and (*c*) are owed to the very low statistics at that energy. 121
- Figure 90 Scatter plots representing the distribution of the minimum of the Cherenkov signal time structures event-by-event as a function of the *x* (*a*) and *y* (*b*) coordinates of  $DWC_1$ . 122
- Figure 91 Subdivision of the selected area of the beam spot. 122
- Figure 92 Mean values of the response as a function of the number of the corresponding subdivided area. Results for three readout configurations: without light mixers (*a*), with 2 cm (*b*) and 4 cm thick light mixers(*c*). 123

## List of Figures

- Figure 93 The four areas selected by means of DWC1. 124
- Figure 94 The mean scintillation signals (*a*) and the same signals normalized to the beam energy (*b*) for regions 0-2 and 2-2 as a function of the beam energy. 125
- Figure 95 Contour plots of the average response over the total surface of the NewDREAM lead/fibers module for the Cherenkov (*a*) and scintillation (*b*) channels. The colour scale represents the values of the average response. 126
- Figure 96 A scheme of the electronic board with the amplifier applied to the readout chain of the PMT. 127
- Figure 97 The average pulse shape of a scintillation signal readout by the G=10 channel. The presence of an overshoot after the signal peak is highlighted. 128
- Figure 98 Energy resolution for the Cherenkov channels, obtained by integrating the signals over two different ns gates. Data points from 4 to 15 GeV have been fitted with the relation  $\sigma/E = p_0 + p_1/\sqrt{E}$ . Data from G=1 and G=10 channels are plotted. 129
- Figure 99 Energy resolution for the scintillations channels, obtained by integrating the signals over two different ns gates. Data points from 4 to 15 GeV have been fitted with the relation  $\sigma/E = p_0 + p_1/\sqrt{E}$ . Data from G=1 and G=10 channels are plotted. 130
- Figure 100 Response linearity for the Cherenkov channels, obtained by integrating the signals over two different ns gates. Data from G=1 and G=10 channels are plotted. 131
- Figure 101 Response linearity for the scintillations channels, obtained by integrating the signals over two different ns gates. Data from G=1 and G=10 channels are plotted. 132

## LIST OF TABLES

Table 1	Energy deposit and composition of the non-em component of hadronic showers in lead and iron. The listed number of particles are per GeV of non-em energy. [1] 30
Table 2	Different properties of Cherenkov and scintillation light. [5] 70
Table 3	Electron beam energies and statistics of the runs used in the analysis. 104
Table 4	Electron beam energies and statistics of the runs used in the analysis, taken with the beam sent in the center of the calorimeter module. 124
Table 5	Comparison between mean scintillation signals in areas 0-2 and 2-2, corresponding to a shift of 2 cm of the impact point of the beam. 125



# INTRODUCTION

In the past three decades, the role played by calorimeters in particle physics experiments has become increasingly important. It's a matter of fact that, nowadays, almost all of such experiments rely strongly on calorimetry.

Originally invented for the study of cosmic-ray phenomena, calorimeters found then their application in accelerator-based particle physics experiments, where they perform a number of crucial tasks.

Calorimeters can be roughly defined as blocks of instrumented material, in which energetic particles are absorbed. Such particles deposit their energy in the calorimeter volume and this energy is then converted into a measurable quantity. A shower of secondary particles whose energy is progressively degraded is the result of the interactions occurring between the particles and the detector. These interactions may be ruled by electromagnetic (em) or strong processes, thus giving rise to em or hadronic showers. The energy deposited in the active medium of a calorimeter is detected in the form of charge or light and provides information about the energy of the incident particle.

The first distinction one has to do is that between electromagnetic and hadronic calorimeters. The former ones are mainly devoted to the detection of electrons and photons through their electromagnetic interactions, while the latter ones are used to detect hadrons through their strong and electromagnetic interactions.

Calorimeters may also be distinguished in homogeneous or sampling, depending on whether their entire volume or only a part of it (the active medium) contributes to the generation of signals, respectively.

The increasingly high energies reached in particle physics experiments and the aim of recording complete event information led calorimeters to be key instruments for particle detection. Nevertheless, one has to cope with some limitations in the performance of such detectors.

The energy resolution of hadronic calorimeters is actually limited by two effects which are peculiar of the hadronic shower development. The *invisible energy* phenomenon is a consequence of the occurrence of nuclear reactions, in which nucleons are released from nuclei. Nuclear binding energy has to be provided for this to happen, and such energy doesn't contribute to the calorimeter signals and is lost for detection. Therefore the response to hadrons results to be smaller than the one to electrons and the calorimeter is said to be *non-compensating*. Besides, the presence of electromagnetically decaying

particles (mostly  $\pi^0$ s) in hadronic showers originates an electromagnetic shower fraction ( $f_{em}$ ) which is energy dependent, thus resulting in calorimeter's non-linearity for hadron detection.

There are several projects which are currently working on the attempt of improving the energy resolution of hadronic calorimeters. I performed the work finalized to the preparation of my Master thesis in the context of one of these projects, namely the CERN R&D 52 Experiment, also known as DREAM (Dual-REAdout Method) Project.

The aim of the DREAM Collaboration is the realization of a full containment hadronic calorimeter which exploits the dual-readout method. The latter relies on the fact that Cherenkov light in hadronic showers is almost exclusively originated by electromagnetic shower particles, since electrons and positrons through which em shower energy is deposited are relativistic down to  $\sim 0.2$  MeV. On the other hand, spallation protons which dominate the non-em calorimeter signals are generally non-relativistic. Therefore, the simultaneous detection of Cherenkov and scintillation light allows the measurement of  $f_{em}$  in hadronic showers on an event-by-event bases. Once the value of  $f_{em}$  is determined, one may correct the measured signals for the effects of non-compensation.

The DREAM Collaboration has been exploring the potential of dual-readout since 2003. The starting point was the study of the performance of a calorimeter prototype consisting of copper and optical fibers as passive and active media, respectively. The encouraging results obtained with this device have led to further studies in the context of fiber calorimetry and a prototype module consisting of lead and fibers (the so called NewDREAM module) has been built in Pavia and tested in the last two years at the H8 beamline of CERN SPS (Super Proton Synchrotron).

The possibility of using crystals for dual-readout purposes has also been investigated in the last years by the DREAM Collaboration, because of the advantages offered by their homogeneity (*e.g.* the possibility of having a higher Cherenkov light yield with respect to the fiber calorimeter). Different types of crystals, such as pure and doped  $\text{PbWO}_4$ , BGO and BSO crystals have been tested at the CERN SPS, as well as a calorimeter combination consisting of a matrix of crystals as electromagnetic part and the first DREAM copper/fibers module as hadronic part.

The final aim of the DREAM Project is the construction and test of a full containment lead/fiber calorimeter. A part of this calorimeter will be tested in November 2012 and will consist of nine modules, each of them similar to the first NewDREAM prototype. Such modules have been built during 2012 in Pavia.

The first chapter of my thesis represents an introductory part, necessary for the understanding of the working principles of calorimetry. The physics of detection mechanisms and the main properties of calorimeters will be the main content of this part.

In the second chapter, a brief overview of the most important results obtained by the DREAM Collaboration in the last years will be given.

The last two chapters are devoted to the description of the work I performed within the DREAM Project. I collaborated with the Pavia DREAM Group on two fronts, namely the analysis of data taken at testbeams during November 2011 and July 2012 and the construction of the previously mentioned lead/fibers modules which will constitute part of the full containment calorimeter.

In the third chapter I will describe the techniques used to build the modules, the characteristics of the materials which have been used and the reasons that led to their choice. Several pictures taken during the construction period will illustrate the stages and the details of the process. Some ideas for the optimization of the calorimeter readout, which were implemented during the July 2012 testbeam, are also presented in this chapter.

Finally, the fourth and last chapter is devoted to the description of the results I obtained from the analysis of data taken with the first NewDREAM module. My analysis covered various topics, such as the study of response non-uniformities over the module surface, as well as the investigation of the effects of changes in the readout.

A preliminary analysis of the November 2011 data highlighted the presence of a constant term in the plot of energy resolution as a function of the energy of the incident beam for the scintillation signals. This term could be justified, among other effects, with the presence of non-uniformities in the response owed to the dependence of the PMTs collection efficiency from the position of incidence on the photocathode. I therefore investigated these non-uniformities, as well as the response linearity of the module.

In the second part of the last chapter I present the results of the test of various configurations of the readout scheme (such as different PMT bases, light mixers and amplification stages) as well as those of the study of the response uniformity over the module surface.



# 1

## CALORIMETRY IN HIGH-ENERGY PHYSICS

### 1.1 BRIEF HISTORY OF CALORIMETRY

In nuclear and high-energy physics, the technique of detecting particles and measuring their properties through total absorption in a block of matter is referred to as calorimetry. The common feature of calorimeters, even though they exist in a wide variety of types, is the destructivity of the process through which the particle properties are measured. This means that particles are no longer available for inspection by other devices after their passage in the calorimeter. An exception to this rule is given by muons, which may penetrate the amount of matter represented by a calorimeter, thus providing an effective way of identifying them.

The origin of the term "calorimetry" looks back to thermodynamics, since almost all the particle energy is eventually converted into heat. However, the rise in temperature of the block that absorbs the particle is, for all practical purposes, negligible and more sophisticated methods are needed to determine the particle properties.

Calorimetric particle detection started when, after World War II, scintillation counters and photomultiplier tubes (PMT) made their appearance. In fact, the fluorescence light emitted by ionizing particles in scintillation detectors can be converted into electric signals in the PMT, making it possible to measure the energy released in the scintillating material. Anthracene and thallium doped sodium iodide crystals were the most common scintillators used in the past and the latter played the main role in  $\gamma$ -ray spectroscopy until the development of semiconductor crystals, such as lithium doped silicon or germanium, which offered a huge improvement in energy resolution.

Until about 1970, particle physics experiments were mostly of fixed-target type. The main goal of such experiments was to measure the four-vectors of all particles produced in these events, in order to reconstruct the details of interactions. One could obtain this by tracking charged reaction products in a magnetic field, thus determining the momentum and the charge sign of the particle from the curvature of the track and the particle's mass from the ionization density ( $dE/dx$ ).

Unfortunately, this technique can't be applied to electrically neutral particles, such as neutrons and photons. The latter ones mostly resulted from  $\pi^0$  decay ( $\pi^0 \rightarrow \gamma\gamma$ ), being  $\pi^0$  production present in almost every reaction.

In order to inspect the properties of the photons and their  $\pi^0$  parents, different kinds of experiments were performed, such as bubble

chamber experiments, in which some fraction of  $\gamma$ s were observed because of their conversion ( $\gamma \rightarrow e^+e^-$ ) inside the volume of the chamber, or counter experiments in which thin sheets of material were installed with the purpose of converting photons into  $e^+e^-$  pairs, whose properties could then be measured in the magnetic field. Both these methods, anyway, are characterized by low efficiency of  $\pi^0$  reconstruction.

A way to overcome this problem is represented by *shower counters*, which became popular after their successes in  $\gamma$ -ray spectroscopy: with the pioneering use of NaI(Tl) in particle physics experiments it became possible to achieve  $\pi^0$  reconstruction with high efficiency, thus starting a long tradition in crystal calorimetry. In order to overcome the problem of NaI(Tl) hygroscopicity, other crystals were used and developed, e.g. CsI.

The lead-glass detector, a different type of shower counter, became popular in the 1960s. Lead-glass, a mixture of  $\text{SiO}_2$  and (up to 70%) PbO, is characterized by high density and transparency: it doesn't scintillate, but relativistic charged particles can be detected through the *Cherenkov* light that these generate in it.

A first important distinction one has to do when talking about calorimeters is that between *homogeneous* and *sampling* ones.

In homogeneous calorimeters, such as the shower counter mentioned above, the entire volume of the counter is sensitive to particles and may contribute to the signals generated by the detector. The material which composes the counter performs thus two functions: absorbing the particles and detecting the signals produced in this process. In order to exercise the first function efficiently, it needs to have a high density.

On the other hand, in sampling calorimeters, the functions of absorbing particles and detecting signals are performed by different materials. The absorber, called *passive medium*, is typically a high-density material, such as lead, iron, copper or uranium. In the *active medium* signals are generated, even if only a small fraction of the energy of the incoming particle is deposited in it. For this reason, energy resolution of sampling calorimeters is considerably worse with respect to that of homogeneous ones.

The role of calorimeters in particle physics experiments grew gradually in importance with the development of particle accelerators and the continuous overcoming of energy frontier. One reason for this is that the precision of calorimeters response improves with increasing energy, while the precision of momentum measurement decreases.

All the experiments at the major accelerator facilities of last years, such as LEP and LHC at CERN, the Tevatron at Fermilab and the SLC at SLAC have put great emphasis on calorimetry, giving the main attention to obtain hermetic coverage.

## 1.2 DETECTION MECHANISMS

Calorimeter signals can be generated from different mechanisms, the most common of which are *ionization*, *Cherenkov radiation* and *scintillation*. Such mechanisms will be described in the following paragraphs.

### 1.2.1 Ionization

A charged particle traversing matter loses energy by interacting electromagnetically with the Coulomb fields generated by the constituents of that matter. One of the possible consequences of this energy loss is the ionization of atoms of which the material is made of. As a result of this process, one or more electrons are released from their Coulomb fields and a ionized atom is created. Free electrons can thus be collected, after a possible amplification, generating in this way the detector signal. In order to describe the ionization mechanism it is necessary to distinguish between the energy loss of electrons or positrons and that of heavy particles, *i.e.* particles heavier than the electron, such as muons, pions, protons,  $\alpha$ -particles and other light nuclei.

#### 1.2.1.1 Heavy particles ionization loss

Heavy particles energy loss is almost completely due to inelastic collisions with the atomic electrons. Even if the amount of energy transferred in each collision is typically a small fraction of the total kinetic energy of the particle, the cumulative energy loss is usually considerable even in relatively thin layers of material, owing to the fact that the number of collisions per unit path length is large.

Atomic collisions are usually divided into *soft* collisions, where the result is only an excitation, and *hard* collisions, where the amount of energy transferred is enough to ionize the atom. In some of the hard reactions this amount is so high that the released electron can cause secondary ionization. These high-energy recoil electrons are called  $\delta$ -rays.

Heavy particles can also be subject to energy loss by elastic scattering from nuclei, even if this process is less frequent than electron collisions and the amount of energy transferred is much smaller since the mass of nuclei is usually larger than that of the incident particle.

Inelastic collisions are statistical in nature and verify with a certain quantum mechanical probability. The fluctuations in total energy loss are nevertheless small, because of the fact that the number of inelastic collisions per macroscopic path length is generally large. It is thus useful to introduce the concept of average energy loss per unit path

length, usually referred to as *stopping power* or simply  $dE/dx$ . This quantity was first calculated classically by Bohr and later using quantum mechanics by Bethe, Bloch and others. In the calculation they assumed that the electron is free and at rest and, after the collision, the incident particle is essentially undeviated from its original trajectory because of its larger mass.

The formula obtained, in which the energy transfer is parametrized in terms of the momentum transfer, is commonly known as *Bethe-Bloch formula* and is the fundamental formula used for energy loss calculations:

$$-\frac{dE}{dx} = 2\pi N_a r_e^2 m_e c^2 \rho \frac{Z}{A} \frac{Z}{\beta^2} \left[ \ln \left( \frac{2m_e \gamma^2 v^2 W_{max}}{I^2} \right) - 2\beta^2 - \delta - 2\frac{C}{Z} \right], \quad (1)$$

where

- $2\pi N_a r_e^2 m_e c^2 = 0.1535 \text{ MeV cm}^2/\text{g}$ ;
- $W_{max}$  is the maximum energy transfer in a single collision, which is produced by a knock-on collision ( $\delta$ -rays);
- $I$  is the mean excitation potential;
- $\delta$  and  $C$  are the density and shell correction respectively.

The density correction  $\delta$  to the Bethe-Bloch formula is important at high energies and is related to the fact that the electric field of the particle also tends to polarize the atoms along its path, thus shielding the electrons far from the path of the particle from the full electric field intensity. The shell correction  $C$ , instead, is important at low energies and accounts for the effects which arise when the velocity of the incident particle is comparable or smaller than the orbital velocity of the bound electrons.

The typical energy dependence of  $dE/dx$  can be seen in Figure 1, in which the Bethe-Bloch formula is plotted as a function of kinetic energy for some different particles. The  $1/\beta^2$  factor is predominant in the region of non-relativistic energies and  $dE/dx$  decreases until reaching a minimum value roughly corresponding to a velocity  $v = 0.96 c$ . Particles at this point are known as *minimum ionizing* and the minimum value of  $dE/dx$  is almost the same for all particles. Increasing the energy, the logarithmic term becomes the dominant one, being  $1/\beta^2$  almost constant, and the  $dE/dx$  curve has a *relativistic rise* until energies at which the density correction becomes effective.

#### 1.2.1.2 Electrons and positrons ionization loss

The Bethe-Bloch formula is also suitable to describe the collision energy loss of electron and positrons, even if with some modifications. These two particles have in fact a smaller mass with respect to heavy charged ones and the assumption that the incident particle

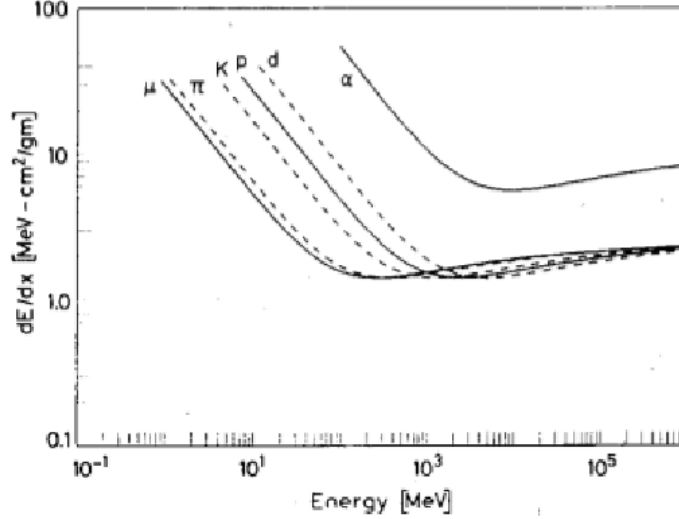


Figure 1: The stopping power  $dE/dx$  as a function of energy for different particles. [2]

remains undeflected during the collision process is therefore invalid. Moreover, calculations must take into account the indistinguishability of identical particles in the case of electrons collisions. Taking the calculations with the proper corrections, the Bethe-Bloch formula eventually becomes:

$$-\frac{dE}{dx} = 2\pi N_a r_e^2 m_e c^2 \rho \frac{Z}{A} \frac{1}{\beta^2} \left[ \ln \frac{\tau(\tau+2)}{2(I/m_e c^2)^2} + F(\tau) - \delta - 2\frac{C}{Z} \right], \quad (2)$$

where  $\tau$  is the kinetic energy of the particle in units of  $m_e c^2$  and  $F(\tau)$  is a function which depends on  $\beta$  and is different for electrons and positrons.

There is a wide variety of particle detectors which use the ionization process as a source of the signal. An example is given by calorimeters based on noble liquids as active medium, such as xenon, argon and krypton. These elements are chosen since all the electronic shells of their atoms are filled, so that they don't capture loose electrons. Between all, liquid argon (LAr) is preferred since it's cheap, abundantly available and with the requested purity levels easy to achieve and maintain. Even if more expensive than LAr, krypton and xenon are used in some experiments in which a higher density is required. Another quality of noble liquids is their radiation hardness, *i.e.* their high resistance to ionizing radiation, which is much higher than that of scintillating crystals.

**IONIZATION DETECTORS** A very important class of ionization detectors is the one based on gaseous media, such as wire chambers and

drift chambers. There is a wide variety of such detectors, but they are all based on the same working principle: the electrons produced in the ionization process are subject to multiplication before being collected at the anode. In fact, while electrons experiment the acceleration due to the electric field between anode and cathode, they may acquire enough energy to ionize other atoms, thus releasing secondary (and possibly tertiary, etc.) electrons. At the end, an *avalanche* of electrons reaches the anode, constituting the signal.

Gaseous ionizing detectors, such as wire chambers, are often the best choice to detect charged particles, especially when one wants to cover large surface areas.

Also semiconductors, such as silicon, germanium and gallium arsenide, have been used for particle detection through ionization, in the form of the so called solid state devices, such as silicon strips. Because of the narrowness of the energy gap between the valence and conduction bands, typically of the order of 1 eV, very little energy is required for the production of one electron-hole pair (e.g. 3.6 eV for silicon). This energy is usually one and two order of magnitude less than that needed to produce one electron-ion pair in gases and one photoelectron in scintillating counters, respectively. This means that semiconductor crystals may offer excellent energy resolution in detectors in which fluctuations in the number of primary charge carriers are the limiting factor. Semiconductor crystals may also be considerably faster than other ionizing detectors because of their greater density and compact structure.

### 1.2.2 Bremsstrahlung

Besides collision loss, there is another mechanism of energy loss which comes into play in the case of electrons and positrons: the emission of electromagnetic radiation arising from scattering in the electric field of a nucleus. This process, known as *bremsstrahlung*, can be classically understood as radiation arising from the acceleration of the electron or positron, being it deviated from its straight-line path by the electrical attraction of the nucleus.

The probability of emission of bremsstrahlung radiation increases rapidly with energy and above a certain critical value (usually of the order of tens of MeV) the energy loss by radiation completely dominates over the collision loss. The *critical energy*  $\epsilon_c$  is that value at which the loss by radiation and ionization are equal.

The total energy loss of electrons and positrons is therefore the sum of ionization and bremsstrahlung radiation loss:

$$\left(\frac{dE}{dx}\right)_{tot} = \left(\frac{dE}{dx}\right)_{rad} + \left(\frac{dE}{dx}\right)_{ion} \quad (3)$$

The critical energy scales roughly as the inverse of the  $Z$  value of the absorbing medium:

$$\epsilon_c \propto \frac{1}{Z} \quad (4)$$

At energies below few hundred GeV the emission of bremsstrahlung radiation plays an important role only for electrons and positrons, since the cross section of this process scales with the inverse square of the particle mass:

$$\sigma_{rad} \propto r_e^2 = \left( \frac{e^2}{mc^2} \right)^2 \quad (5)$$

This fact means that, for example, radiation loss by muons, the next lightest particle, is about 40000 times smaller than that by electrons.

### 1.2.3 Cherenkov radiation

The result of the process involving a charged particle moving faster than the speed of light in a medium is the emission of *Cherenkov radiation*. The condition is therefore

$$v_{particle} > \frac{c}{n},$$

being  $c$  the speed of light in vacuum and  $n$  the index of refraction of the medium. If such condition is satisfied, an electromagnetic shock wave is generated with a conical coherent wavefront emitted at a well-defined angle known as Cherenkov angle, dependent on the speed of the particle and the frequency of the emitted radiation  $\omega$ :

$$\theta_c = \arccos \left( \frac{1}{\beta n(\omega)} \right)$$

The peculiar  $1/\lambda^2$  dependence of the Cherenkov light spectrum causes the visible part of it is to be perceived as blue light and the process is instantaneous, differently from the case of scintillation, which is characterized by one or more time constants (see next). This latter characteristic makes a detector based on Cherenkov effect a useful device in experiments which require high signal speed.

Even if Cherenkov light emission is only a small source of energy loss with respect to collision and radiation loss, the Cherenkov mechanism can be a precious one to provide particle identification. Because of the dependence of Cherenkov emission on the velocity of the particle, it can be used indeed to determine the mass of particles of which the momentum is known by means of deflection in magnetic field. At present there are a lot of devices developed to perform particle identification exploiting this effect, such as threshold Cherenkov counters, differential Cherenkov counters and ring imaging Cherenkov detectors (RICH).

### 1.2.4 Scintillation

The scintillation process occurs when an atom or molecule of a medium, after the passage of a charged particle, is brought into an excited state. Since such states are unstable, usually the excited atom or molecule rapidly returns on its ground state, releasing the excitation energy in form of one or more photons with a timescale determined by the excitation energy, by the number of available return paths and by the quantum numbers of the states involved. Scintillator materials exhibit the property known as *luminescence*, *i.e.* when they are exposed to a certain form of energy, such as light, heat, radiation, etc., they absorb and re-emit the energy in the form of visible light. If the re-emission takes place within  $10^{-8}$  s the process is called *fluorescence*.

The time evolution of the re-emission process is described by a two component exponential law (a simple exponential decay at first approximation):

$$N = Ae^{-t/\tau_f} + Be^{-t/\tau_s}, \quad (6)$$

where  $N$  is the number of photons emitted at time  $t$ ,  $\tau_f$  and  $\tau_s$  are the decay constants.  $A$  and  $B$ , which vary from material to material, are the relative magnitudes of the *fast* and *slow* (or the *prompt* and *delayed*) components, as they are usually defined, since one component is usually much faster than the other.

Simple inorganic scintillating crystals, such as NaI(Tl) and BGO, have decay time of several hundred of nanoseconds, about 2-3 orders of magnitude slower than complex organic scintillators, such as the plastics anthracene and polystyrene.

Scintillation, which was the first physics process used to produce calorimetric signals, is still exploited as a source of information in many particle experiments.

The development of scintillator-based calorimetry has been made possible by the invention of two fundamental devices: the PhotoMultiplier Tube (PMT) and the wavelength shifters. The basic element of a scintillation detector consists, in fact, in a scintillating material optically coupled to a PMT usually via a light guide. The PMT provides the conversion of scintillation light into electric signals and, since the emission spectrum of a scintillator often peaks at UV wavelengths, while the PMT has a maximum in the visible range, sometimes it is useful to add a wavelength shifter plate, *i.e.* a material which absorbs light at one frequency and reemit it at another, in order to make the spectrum of emitted light more compatible with the PMT cathode.

More recently the design of scintillator calorimeters has been strongly influenced by the development of plastic optical fibers, usually made of a polystyrene core surrounding one or more layers of cladding. These fibers are both the source of the light, which is isotropically generated, and the medium through which this light is transported

until it is converted into electric signals.

The use of scintillating fibers offers considerable advantages, including:

- the possibility of obtaining an hermetic calorimeter structure;
- high signal speed;
- the very high sampling frequency that can be obtained using fibers as active medium, which means good energy and position resolution;
- high light yield and excellent cost/performance ratio;
- arbitrary granularity allowed by the fiber structure.

### 1.3 PHOTON INTERACTIONS

There are four processes affecting the propagation of photons in matter: the photoelectric effect, coherent (Rayleigh) scattering, incoherent (Compton) scattering and electron-positron pair production.

#### 1.3.1 Photoelectric effect

This process consists in an atom absorbing the photon and emitting an electron and is the most probable at low energies. The atom is thus left in an excited state and returns to the ground state by the emission of Auger electrons or X-rays. The photoelectric cross section is strongly dependent on the  $Z$  value of the absorber material, namely on the available number of electrons, as it can be seen in Figure 2. More precisely,

$$\sigma \sim Z^n, \quad (7)$$

where  $n$  varies from 4 to 5. The cross section also shows a significant dependence on the photon energy, scaling as  $E^{-3}$ , so that photoelectric effect gradually becomes less important as the energy increases, as it can be seen in Figure 5. For example, in uranium, which is the material used in calorimeter construction with the highest  $Z$  value, photoelectric effect is the dominant process below 700 keV, while in iron is only 100 keV.

#### 1.3.2 Rayleigh scattering

This process, also important at low energies, only affects the spatial distribution of the energy deposition, since the photon doesn't lose energy, but it is only deflected by the atomic electrons.

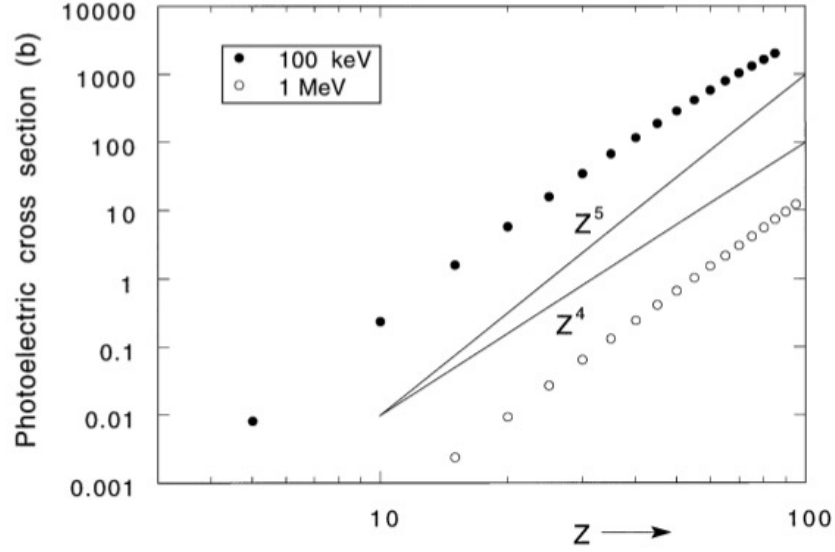


Figure 2: Cross section for the photoelectric effect as a function of the  $Z$  value of the absorber (data for 100 keV and 1 MeV  $\gamma$ s). [1]

### 1.3.3 Compton scattering

In all but the highest- $Z$  absorber materials, the Compton process is the most probable in the energy range between a few hundred keV and  $\sim 5$  MeV. It consists in the scattering of a photon by an atomic electron with the transfer of momentum and energy to the struck electron sufficient to put it in an unbound state.

Compton scattering is a key process to understand calorimetry: in the absorption process of multi-GeV electrons, positrons or photons, at least half of the total energy is indeed deposited by Compton  $\gamma$ s.

The cross section of Compton process is given by the *Klein-Nishina* formula and was one of the first to be calculated using Quantum Electrodynamics:

$$\frac{d\sigma}{d\Omega} = \frac{r_e^2}{2} \frac{(1 + \cos^2\theta)}{[1 + \zeta(1 - \cos\theta)]^2} \left\{ 1 + \frac{\zeta^2(1 - \cos\theta)^2}{(1 + \cos^2\theta)[1 + \zeta(1 - \cos\theta)]} \right\} \quad (8)$$

where  $\zeta$  is the photon energy in units of the electron restmass ( $\zeta = E_\gamma/m_e c^2$ ) and  $\theta$  is the scattering angle of the photon.

In the limit of zero energy, the Klein-Nishina formula reduces to the classical expression for *Thomson* scattering:

$$\frac{d\sigma}{d\Omega} = \frac{r_e^2}{2} (1 + \cos^2\theta) \quad (9)$$

Many  $\gamma$ s in the MeV energy range are absorbed in a sequence of Compton scattering processes, decreasing their energy step by step down to a value where the final absorption in a photoelectric process

can occur.

The dependence of Compton cross section on the  $Z$  value of the absorber material is much less significant than in the photoelectric process: as illustrated in Figure 3, the cross section is almost proportional to  $Z$ , namely to the number of target electrons in the nuclei.

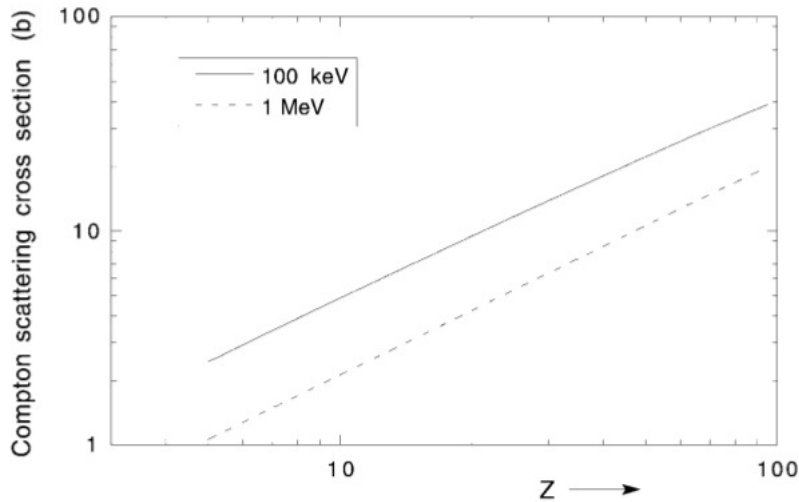


Figure 3: Cross section the Compton scattering as a function of the  $Z$  value of the absorber, for  $\gamma$ s of 0.1 and 1.0 MeV. [1]

Concerning the energy dependence, the Compton cross section decreases with increasing photon energy, but less steeply than for photoelectric effect: the scaling is now as  $1/E$ . This can be seen in Figure 4. As a consequence, there will be a threshold energy above which the Compton scattering becomes more likely than photoelectric absorption to occur. The threshold energy varies from 20 keV for carbon ( $Z=6$ ) to 700 keV for uranium ( $Z=92$ ).

#### 1.3.4 Pair production

When the photon energy overcomes the value of two electron rest masses, the creation of an electron-positron pair becomes possible. This process can occur only in the field of a charged particle, because of the restrictions imposed by conservation of energy and momentum. Nuclear electromagnetic fields are usually responsible of more than 99% of the  $\gamma \rightarrow e^+e^-$  conversions, but in the case of low- $Z$  elements and at high energies also the fields of atomic electrons give a significant contribute to the total pair production cross section.

Once created,  $e^+$  and  $e^-$  produce bremsstrahlung radiation and ionization while passing through matter. The positron annihilates with an electron producing two new photons with 511 keV of energy each

(the electron rest mass), assuming that the annihilation occurs when the positron has come to rest. The newly created  $\gamma$ s which satisfy the energy requirements will in turn produce  $e^+e^-$  pairs, thus originating an electromagnetic shower, as it will be discussed in the next section.

Pair production is the most likely process to occur at high energies, since its cross section rises with energy, as well as with  $Z$ , reaching an asymptotic value above 1 GeV, as it can be seen in Figure 4.

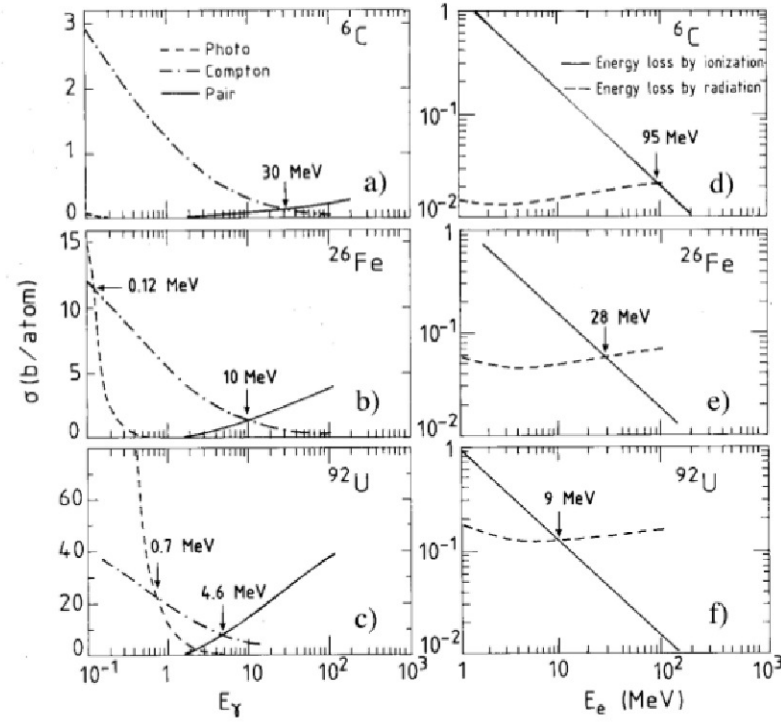


**Figure 4:** Cross section for the processes through which the particles composing electromagnetic showers lose their energy, in various absorber materials. On the left the cross sections for pair production, Compton scattering and photoelectric effect in carbon (a), iron (b) and uranium (c) are shown. On the right the fractional energy losses by radiation and ionization are given as a function of the electron energy in carbon (d), iron (e) and uranium (f). [1]

Figure 4 shows the cross section for the three processes through which photons lose energy in matter, *i.e.* photoelectric effect, Compton scattering and pair production, as a function of energy for carbon ( $Z=6$ ), iron ( $Z=26$ ) and uranium ( $Z=92$ ).

Figure 5 summarizes the energy domains of the three processes: photoelectric effect dominates at low energies for high- $Z$  absorbers, Compton scattering dominates in the low-intermediate region, even if its importance decreases with increasing  $Z$  of the absorber.

Another consideration to do concerns the angular distribution. Pair production is characterized by a highly directional distribution, while

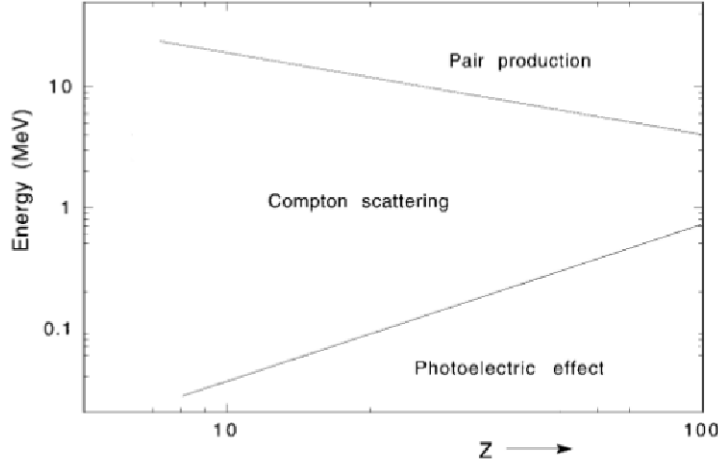


Figure 5: The energy domains in which photoelectric effect, Compton scattering and pair production are the most likely processes to occur, as a function of the Z value of the absorber material. [1]

Compton electrons and photoelectrons are isotropically distributed with respect to the direction of the initial  $\gamma$ .

There is a remarkable difference between charged particles and photons interactions. The former lose energy continuously. For example, a multi-GeV electron traversing one cm of lead usually radiates thousands of photons, the majority of which are very soft, with energies in the eV-keV-MeV range. A multi-GeV photon, instead, can traverse the same thickness of lead without being affected. For such a photon the *mean free path*  $\lambda$ , that is the mean distance traveled by the particle without interacting, can thus be introduced and the probability of interaction after a distance  $x$  can be expressed as

$$P_{int}(x) = 1 - e^{-x/\lambda} \quad (10)$$

In the case of lead  $\lambda=7.2$  mm, so the probability of conversion of the mentioned multi-GeV photon in one cm of material is about 75%.

## 1.4 THE PHYSICS OF SHOWER DEVELOPMENT

The interaction processes occurring when a particle traverses the matter depend on the energy and the nature of the particle, as we have seen in the previous sections. These processes are the result of the electromagnetic (em), the strong and, more rarely, the weak forces which act among the constituents of matter.

In this section the shower development characteristics will be discussed, as well as the effects of electromagnetic and strong interac-

tions and the consequences of differences between these interactions for the calorimetric energy measurement of electrons and hadrons.

#### 1.4.1 Electromagnetic showers

Since bremsstrahlung is the principal source of energy loss by high-energy electrons (and positrons), a primary, multi-GeV electron traversing a detector usually radiates thousands of photons, which are then mainly absorbed through Compton scattering and photoelectric effect. Nevertheless, photons with more than 5-10 MeV can create  $e^+e^-$  pairs. If their energy is higher than the critical energy (remember Equation 4), electrons and positrons generated in the latter process may in turn radiate more photons, which can convert in  $e^+e^-$  pairs and so forth, giving rise to a shower composed by electrons, positrons and photons.

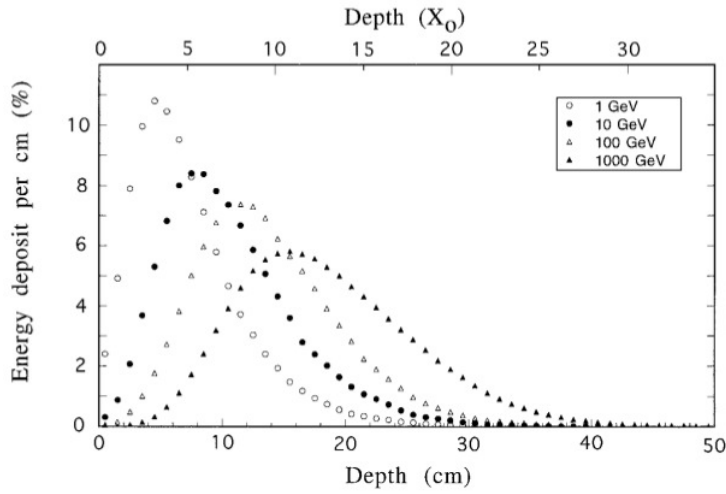
The number of electrons and positrons initially increases with increasing shower depth, as well as the amount of energy deposited. Nevertheless, as the shower develops, the energy of the shower particles decreases, and at a certain depth there is no more multiplication. This depth is called the *shower maximum* and, beyond it, the shower photons on average produce with higher probability a single electron (through Compton or photoelectric interactions) than a  $e^+e^-$  pair. In the same way, at this point electrons and positron prefer to lose their energy through ionization. In conclusion, beyond the shower maximum there is a decrease of the number of shower particles and thus of the energy deposited in the detector.

Figure 6 shows the energy deposited as a function of depth, for em showers originated from electrons of different energies in a block of copper. It can be seen that the higher the initial energy of the showering particle, the longer the particle multiplication phase continues.

As it was previously said, most of the shower particles are very soft, as it is illustrated in Figure 7. This means that most of energy is deposited through Compton and photoelectric effect. The number of positrons, which are only produced in pair production, results to be considerably minor than that of electrons, produced in all the three photon interaction processes. However, the number of positrons produced per unit of energy increases from lower to higher Z values of the absorber medium: that's because in showers developing in high-Z materials one has particle multiplication down to lower energies with respect to low-Z materials.

Positrons usually deposit one quarter of the total electromagnetic shower energy, electrons deposit the remaining part. Figure 8 shows the difference between spatial profiles of the energy deposited by electrons and positrons. This difference is considerable especially in the lateral profile, meaning that, on average, electron energy is deposited

twice as far from the shower axis with respect to positrons.



**Figure 6:** The energy deposit as a function of depth, for 1, 10, 100 and 1000 GeV electron showers developing in a block of copper. The integral of these curves have been normalized at the same value, in order to compare the energy deposit profiles. The vertical scale gives the energy deposit per cm of copper, as a percentage of the energy of the showering particle. Results of EGS4 calculations. [1]

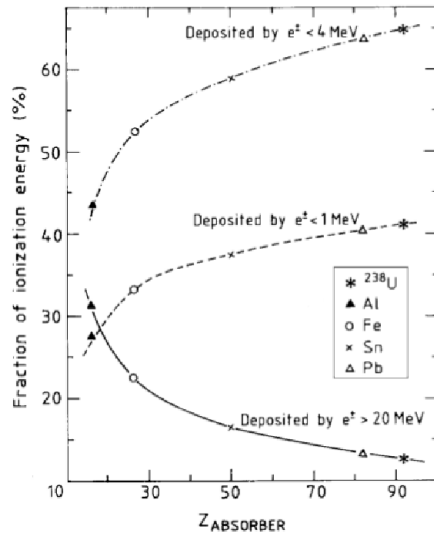


**Figure 7:** The composition of em showers. Shown are the percentages of the energy of 10 GeV electromagnetic showers deposited through shower particles with energy below 1 MeV (the dashed curve), below 4 MeV (the dash-dotted curve) or above 20 MeV (the solid curve), as a function of Z of the absorber material. Results of EGS4 simulations. [1]

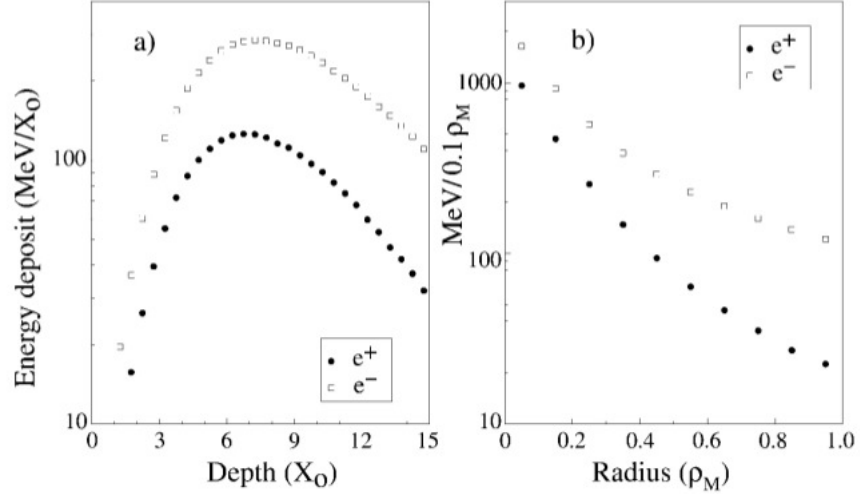


**Figure 8:** Comparison of the longitudinal (a) and lateral (b) profiles of the energy deposited by electrons and positrons in 10 GeV em showers developing in lead. The vertical scale is logarithmic. Results of EGS4 simulations. [1]

#### 1.4.1.1 Radiation length and Molière radius

In order to describe the shower characteristics without any dependence from the material, it is useful to introduce two scaling variables concerning the shower dimensions, *i.e.* the *radiation length*  $X_0$  for the longitudinal development and the *Molière radius*  $\rho_M$  for the lateral one.

The radiation length  $X_0$  is defined as the distance over which a high-energy electron or positron (with energy  $\gg 1$  GeV) loses, on average, 63.2% (*i.e.*  $1 - e^{-1}$ ) of its energy to bremsstrahlung.

The usefulness of this definition can be quickly understood if one observes that, by expressing the dimension of the absorber structure in units of  $X_0$ , material-dependent effects are, in first approximation, eliminated. For example, high-energy electrons lose the same amount of energy in 18 cm of water and in 2.8 mm of lead, both corresponding to  $0.5 X_0$ .

It can be shown that the asymptotic cross section for photon interactions is related to  $X_0$  as

$$\sigma(E \rightarrow \infty) = \frac{7}{9} \frac{A}{N_A X_0}, \quad (11)$$

where  $X_0$  is expressed in  $\text{g cm}^{-2}$  (in order to eliminate the differences in material density) and the ratio of Avogadro's number  $N_A$  and the atomic weight  $A$  denotes the number of atoms per gram of material. This implies that the mean free path of very-high-energy photons

equals  $9/7X_0$ .

An expression of  $X_0$ , valid for approximate calculations is given by:

$$X_0 = \frac{716.4 A}{Z(Z+1)\ln(287/\sqrt{Z})} g \text{ cm}^{-2} \quad (12)$$

The Molière radius  $\rho_M$ , on the other hand, hasn't a well defined physical meaning. It is used to describe, in an approximately material-independent way, the transverse development of em showers and it's defined, in term of  $X_0$  and the critical energy  $\epsilon_c$  (see Equation 4), in this way:

$$\rho_M = m_e c^2 \sqrt{4\pi/\alpha} \left( \frac{X_0}{\epsilon_c} \right) = 21.2 \text{ MeV} \left( \frac{X_0}{\epsilon_c} \right), \quad (13)$$

where  $\alpha$  is the fine-structure constant ( $\alpha \sim 1/137$ ).

On average, 90% of the shower energy is deposited in a cylinder with radius  $\rho_M$  around the shower axis. The Molière radius has a weaker  $Z$  dependence with respect to the radiation length, as can be seen from Equations 4, 12 and 13. For example, the radiation lengths for copper ( $Z=29$ ) and lead ( $Z=82$ ) have a factor 3 of difference, being 14.3 mm and 5.6 mm respectively, while the Molière radii are quite similar, being 15.2 mm for copper and 16.0 mm for lead. In the construction of a calorimeter, it takes about three times as much copper as lead (in cm) to contain these showers longitudinally, while laterally the showers have about the same dimension.

#### 1.4.1.2 A simple model of em shower development

Finally, a simple model of the development of the em cascade is described. This model can be applied both to a photon and an electron as starting particle. We suppose to begin with a photon of energy  $E_0$ , with  $E_0$  larger than the threshold for pair production. On average it will convert in a  $e^+e^-$  pair after one radiation length, each member of the pair having an energy equal to  $E_0/2$ . The electron and the positron will each emit a bremsstrahlung photon after two radiation length, with roughly half of the energy of the charged particle. So, after two radiation lengths, there will be four particles, each with  $E_0/4$ . Reasoning in this way, at the end of  $t$  radiation lengths, the total number of particles present will be  $N \simeq 2^t$ , each with an average energy of  $E(t) \simeq E_0/2^t$ . In this model the shower maximum can be found by assuming that the shower stops at the critical energy

$$E(t_{max}) = \frac{E_0}{2^{t_{max}}} = \epsilon_c, \quad (14)$$

thus finding for  $t_{max}$ :

$$t_{max} = \frac{\ln \frac{E_0}{\epsilon_c}}{\ln 2} \quad (15)$$

The maximum number of particles produced is then:

$$N_{max} \simeq \frac{E_0}{\epsilon_c} \quad (16)$$

However, in order to get a more precise picture of a shower development, being this model only approximative, it is necessary to recourse to more refined techniques, such as Monte Carlo simulations.

#### 1.4.1.3 Electromagnetic shower profiles

The longitudinal development of 10 GeV electron showers in aluminium, in iron and in lead is showed in Figure 9, where the horizontal axis is expressed in units of  $X_0$ . Even if, at a first look, the three profiles seem very similar, there are two substantial differences among the absorber materials, thus causing the profiles to not scale perfectly with  $X_0$ .

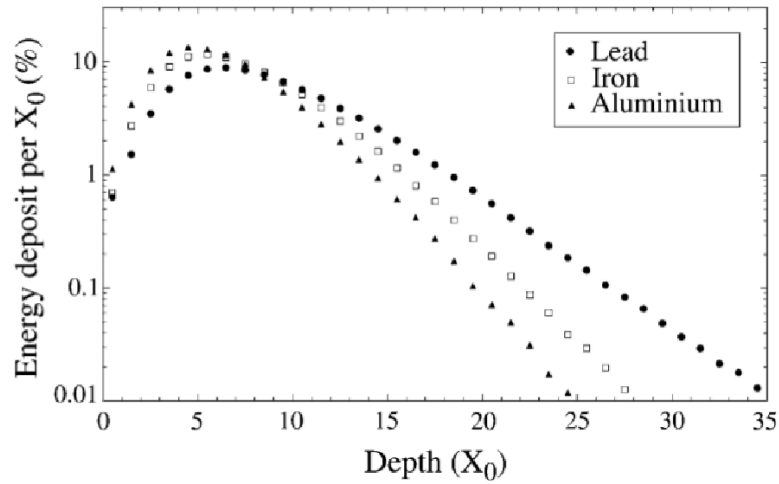


**Figure 9:** Energy deposit as a function of depth, for 10 GeV electron showers developing in aluminium, iron and lead, showing approximate scaling of the longitudinal shower profile, when expressed in units of radiation length,  $X_0$ . Results of EGS4 calculations. [1]

In fact, it can be observed that, with increasing  $Z$  values, the shower maximum shifts to greater depth and the shower profiles decay more slowly beyond the shower maximum. The consequence of this phenomenon is that one needs more radiation lengths to contain a given electromagnetic shower in lead than in iron or in aluminium. For example, it takes 25  $X_0$  of lead, *vs.* 21  $X_0$  of iron and 18  $X_0$  of aluminium, to contain 10 GeV electron showers, on average, at the 99% level. The differences among the longitudinal shower profiles in the three absorber materials, as previously said regarding the strong increase of the number of positrons with the  $Z$  value of the absorber material, are

related to the fact that in high-Z materials shower particle multiplication continues down to much lower energies than in low-Z materials and decays more slowly beyond the shower maximum.

The lateral spread of em showers is substantially caused, in the early stages of the shower development, by multiple scattering of electrons and positrons, which are moved away from the shower axis. Beyond the shower maximum, and particularly in high-Z media, lateral spread is mostly caused by the isotropy of Compton and photoelectric processes. Electrons and photons produced in such processes thus move away from the shower axis, as well as, to a lesser extent, bremsstrahlung photons emitted by electrons travelling at a certain distance from the shower axis. Figure 10 shows the results from EGS4 Monte Carlo simulations for the radial energy deposit profiles for 10 GeV electrons showering in lead, copper and aluminium, denoting a much smaller dependence from the material with respect to the longitudinal profile. Also here, the scaling with  $\rho_M$  isn't perfect. Deviation from scaling as observed in these figures are caused by phenomena which occur at energies below the critical energy, that is Compton scattering and photoelectric effect. For example, in lead more than 40% of the shower energy is deposited by particles with energy below 1 MeV, while the critical energy is about 7 MeV. Both the two processes mentioned above dominate at energies far below the critical energy, thus not being suitably described by the variables  $X_0$  and  $\rho_M$ , which are defined in the asymptotic energy regime ( $>1$  GeV).

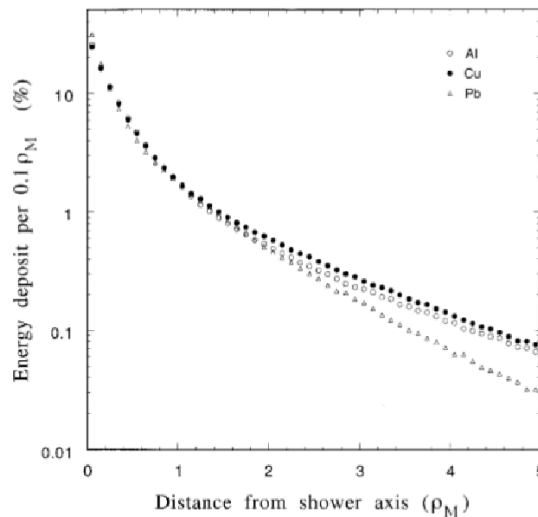
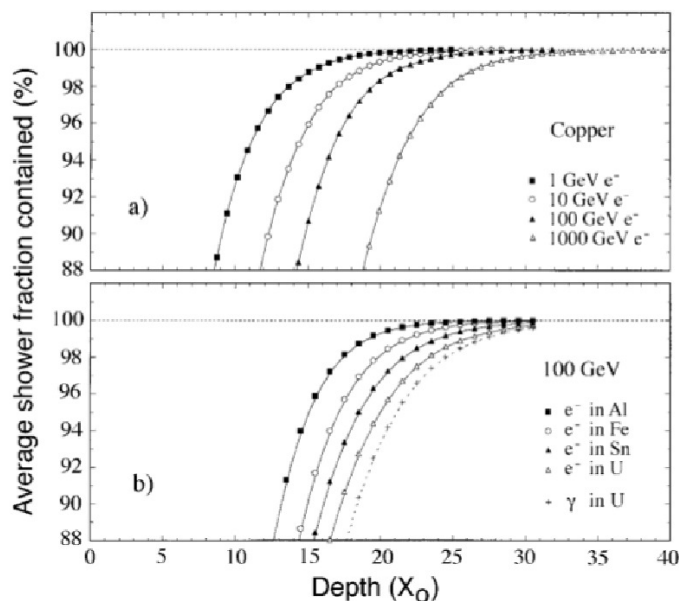


Figure 10: Radial energy deposit profiles for 10 GeV electrons showering in aluminium, copper and lead. Results of EGS4 calculations. [1]

The fact that, in em showers, photo- and Compton electrons contribute in a major way to energy deposit in the calorimeter and that

these processes have isotropic angular distributions results in the possibility to orient the active layers in any direction in a sampling calorimeter. The original belief that only a *sandwich* type calorimeter would have worked has been fully disproved and nowadays there is a wide variety of geometries in use, such as fiber structures with fibers oriented in the same direction of the showering particles. This is, in particular, the idea at the base of the NewDREAM detector, which will be largely described in the following chapters. Such alternative configurations generally offer various advantages, for example in terms of hermeticity or signal speed.

There's a difference in the early stage of showers generated by electrons or photons. In fact, high-energy electrons start to irradiate as soon as they encounter material and they may emit thousands of bremsstrahlung photons in few mm of material. High-energy photons instead don't always convert in the same amount of material. This effect doesn't influence the shower containment, anyway. It takes in fact relatively little extra material to contain a  $\gamma$ -induced shower with respect to an electron-induced one with the same energy, as it can be seen in Figure 11.



**Figure 11:** Average energy fraction contained in a block of matter with infinite transverse dimensions, as a function of the thickness of this absorber. Shown are results for showers induced by electrons of various energies in a copper absorber (a) and results for 100 GeV electron showers in different absorber materials (b). The lower figure also shows the results for 100 GeV  $\gamma$  showers in  $^{238}\text{U}$ . Results of EGS4 calculations. [1]

For example, a 20 GeV photon travels, on average,  $9/7$  radiation lengths before converting into an  $e^+e^-$ -pair of 10 GeV each. Therefore, it takes only an extra  $9/7 X_0$  to contain twice as much em shower energy, implying a logarithmic energy dependence of the longitudinal shower profiles.

#### 1.4.2 Hadronic showers

Hadronic showers, in which the strong interactions between the shower particles and the nuclei of the absorber medium also play an important role, are much more complex than electromagnetic ones, just because of the nature of this kind of interactions. In fact, much more processes may occur, with respect to the electromagnetic case, both at the particle level and involving the struck nucleus.

The wide variety of processes which determine the developing of hadronic showers is responsible for two main effects:

- the production of hadronic shower particles, about the 90% of which are pions. Among them,  $\pi^0$ s decay in two  $\gamma$ s, which develop em showers;
- the occurrence of nuclear reactions, with the release of neutrons and protons from atomic nuclei. The fraction of the shower energy used to provide nuclear binding energy doesn't contribute to the calorimeter signals, creating the so called *invisible energy* phenomenon.

In the interaction of hadrons with matter, what happens is a combination of all the various processes previously seen for charged particles and photons.

Charged hadrons will continuously ionize the atoms of the absorber medium. At a certain depth a strong interaction between the hadron and an atomic nucleus will occur. In this nuclear reaction, the hadron may change its identity, *e.g.* turning into tens of hadrons. The struck nucleus may lose in turn some neutrons and protons, thus ending up in an excited state, which decays by emitting several  $\gamma$ s.

Nuclear reactions are the only possibility for losing energy in the case of neutral hadrons. Neutrons, in particular, a lot of which are originated in the hadronic shower development, deposit their kinetic energy differently from charged shower particles, with important implications for calorimetry.

Mesons, nucleons or  $\gamma$ s which are typically produced in the starting nuclear reaction will in turn produce ionization of the medium and/or induce new nuclear reactions: this is the way in which the hadronic shower develops. The concept of shower maximum can be usefully introduced also in this context. At the beginning of the shower development, one has the multiplication process and, therefore, an increase of the number of shower particles, as well as of the

energy deposited by them. At a certain depth, anyway, a further multiplication is counteracted by the absorption of shower particles and beyond this shower maximum one has the decreasing of both the number of shower particles and their energy deposit.

#### 1.4.2.1 Nuclear interaction length

A major difference between hadronic and em showers is represented by the *scales* of shower development, which are different to an extent determined by the differences between the cross sections for strong and em reactions. In this contest, the shower dimensions are governed by the *nuclear interaction length*  $\lambda_{int}$ , *i.e.* the average distance a hadron has to travel inside the absorber medium before inducing a nuclear interaction.  $\lambda_{int}$ , which is also expressed in  $\text{g cm}^{-2}$ , scales with  $\sqrt[3]{A}$ , differently from  $X_0$  which scales with  $A/Z^2$ .

The probability for a particle to traverse a distance  $z$  in the absorber material without interacting is:

$$P_{int} = e^{-z/\lambda_{int}}, \quad (17)$$

being this definition equivalent to the one for the mean free path of high-energy photons, which was found to be equal to 9/7 of a radiation length (Equation 11). So, just as the mean free path of photons is inversely proportional to the total cross section for photon-induced reactions,  $\lambda_{int}$  is inversely proportional to the total cross section for nuclear interactions in this way:

$$\sigma_{tot} = \frac{A}{N_A \lambda_{int}} \quad (18)$$

On average, hadronic shower profiles look very similar to em ones, even if the scale factor is much larger. For example, in the case of copper,  $X_0$  amounts to 1.4 cm, while  $\lambda_{int}$  is equal to 15 cm.

The different components of hadronic showers and their properties will now be described.

#### 1.4.2.2 The electromagnetic component

At the earlier stages of the shower development,  $\pi^0$ s and other electromagnetically decaying particles (such as  $\eta$ s) are produced. From their decay in two  $\gamma$ s, an electromagnetic component originates in hadronic showers. The fraction of the initial hadron energy converted into  $\pi^0$ s has strong event-to-event variations and therefore the fraction of the shower which propagates electromagnetically, known as the *electromagnetic fraction*  $f_{em}$ , fluctuates strongly event by event. Moreover, being the  $\pi^0$ s production an irreversible process, the  $f_{em}$  gradually increases with energy, as it will be explained later.

Since, on average,  $\pi^0$ s represent roughly one third of the mesons

produced in the first interaction, a simple model can be introduced in order to estimate the electromagnetic fraction. Assuming that all available shower energy is used for mesons production, and  $\pi^0$ s are one third of the mesons produced in the nuclear reactions, then  $f_{em}$  amounts, after  $n$  generations to:

$$f_{em} = 1 - \left(1 - \frac{1}{3}\right)^n \quad (19)$$

What happens after each collision in the hadronic shower is that  $(1-1/3)$  of the remaining energy is, on average, available for the next collisions. This process continues until the energy is no more sufficient for  $\pi^0$  production, thus being  $n$ , the number of generations, a function of the energy  $E$  of the particle that initiated the shower. Assuming that the total number of mesons produced in the shower development is proportional to  $E$  and that the average multiplicity  $\langle m \rangle$ , *i.e.* the average number of mesons produced per interaction, does not depend on  $E$ , then equation 19 well describes the scaling of  $f_{em}$ .

This simple model, anyway, is only an approximation, because it doesn't take into account some relevant facts. Firstly, the factor  $1/3$  used in the model is an upper limit, being not only pions the particle produced in the interactions. This factor should be better denoted as  $f_{\pi^0}$ . Secondly, the average multiplicity  $\langle m \rangle$  actually depends on energy, in particular it increases logarithmically with  $E$ . Moreover, energy loss by ionization and nuclear excitation of the calorimeter media have been neglected, as well as some peculiarities, such as baryon number conservation.

More precise calculations, developed by Gabriel *et al.* [3], lead to a general expression for  $f_{em}$ , as follows

$$f_{em} = 1 - \left(\frac{E}{E_0}\right)^{k-1}, \quad (20)$$

in which  $E_0$  is a scale factor, corresponding to the average energy requested for the production of one pion, and the exponent  $(k-1)$  is related to  $\langle m \rangle$  and to the average fraction of  $\pi^0$  production in the reactions,  $f_{\pi^0}$ :

$$1 - f_{\pi^0} = \langle m \rangle^{(k-1)} \rightarrow k = 1 + \frac{\ln(1 - f_{\pi^0})}{\ln \langle m \rangle} \quad (21)$$

From Equations 20 and 21 one can deduce that the exponent  $k$ , which defines the energy dependence of the em shower fraction, is determined by the two parameters  $f_{\pi^0}$  and  $\langle m \rangle$ .  $k$  has typically a value around 0.8.

Equation 20 resulted a good one to describe the energy dependence of the average em fraction of hadron showers in a given absorber material, once chosen appropriate values for the parameters  $k$  and  $E_0$ .

From the extensive study of this equation, Gabriel and his coworkers deduced some interesting things, such as the dependence of the parameter  $E_0$  from the  $Z$  value of the medium and the fact that the em fraction in proton-induced showers is significantly smaller than for pion-induced showers of the same energy. This latter effect can be simply explained by noticing that in proton-induced showers the baryon number must be conserved, differently from the case of pion-induced showers, thus limiting  $\pi^0$  production. In order to explain the  $Z$  dependence of  $E_0$ , instead, one has to point the fact that secondary and higher-order hadrons produced in the nuclear reactions lose energy by ionizing the material they traverse on their way to a target nucleus. The amount of energy lost in this way depends strongly from  $Z$ . The number of different hadrons produced in the shower development decreases with the increasing amount of energy loss per hadron, thus increasing  $E_0$  and decreasing the number of generations  $n$  and  $f_{em}$ .

The predictions obtained from Equation 20 have been experimentally supported by the SPACAL [4] and QFCAL [21] Collaborations, which have tried to measure the electromagnetic components of hadronic showers with their dedicated instruments. The SPACAL collaboration, for example, measured the  $f_{em}$  by studying the lateral profiles of showers generated by pions of various energies. Its results are represented in Figure 12, in which the curves correspond to calculations obtained from Equation 20, using a value  $E_0=1.3$  GeV, as recommended by Gabriel *et al.* for lead, which was the absorber material of the SPACAL detector, and varying the parameter  $k$  (the three curves represent results for  $k = 0.80, 0.82$  and  $0.84$  respectively). The experimental data favor  $k = 0.82$ .

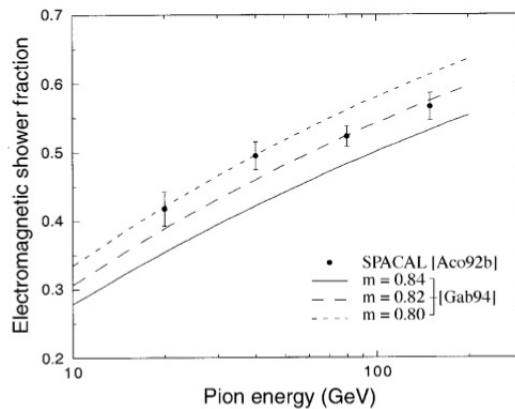


**Figure 12:** The average em shower fraction in pion-induced showers measured in the SPACAL lead/fiber calorimeter. The curves represent predictions based on Equation 20. Experimental data from [4].

Besides the electromagnetic component, in the analysis of the *particle sector* of hadronic showers, one has also to consider the ionization losses by charged hadrons, mostly protons and pions, which occur, on average, after one nuclear interaction length from the point where the particle is created in the collisions. Since pions are only  $2/3$  the size of protons, they are less likely to encounter a nucleus and travel typically a 25-50% longer distance, losing therefore 25-50% more energy by ionization, than protons before a nuclear interaction occurs.

#### 1.4.2.3 *The nuclear sector*

In typical hadron showers developing in lead, the remaining non-em energy is deposited by many kinds of particles. 56% of this energy is deposited by ionizing particles, as seen in the previous section, two third of which are protons, 10% by very soft neutrons (typically 3 MeV) and the remaining 34% is invisible energy.

The most probable reaction to occur when an high-energy hadron encounters an atomic nucleus is *spallation*. It this two-stage process, a cascade of fast nucleons arises from collisions of the incoming hadron with nucleons inside the struck nucleus. Then the intermediate nucleus de-excites by emitting free nucleons,  $\alpha$ s or also nuclear aggregates (evaporation stage) until the excitation energy becomes less than the binding energy of one nucleon.  $\gamma$  rays are emitted in order to release the few MeV of remaining energy. The number of reactions which can occur with comparable probability from spallation of a given nucleus induced by an hadron of a certain energy is enormous. An example is given in Figure 13, which shows the cross section for nuclides that can be produced from  $^{238}\text{U}$  spallation induced by a 2 GeV hadron. The largest cross section for an exclusive reaction amounts to only  $\sim 2\%$  of the total spallation cross section, and there are about 300 different reactions that contribute more than 0.1% to the total spallation cross section.

In order to release spallation nucleons, the nuclear binding energy should be provided. This energy is therefore lost for calorimetric purposes, since it doesn't contribute to calorimetric signal and for this reason it is called *invisible energy*. Event-to-event fluctuations in the invisible energy fraction are very large, and represent the ultimate limit for the energy resolution of hadronic calorimeters ( $\sim 15\%/\sqrt{E}$ ). There is, anyway, a correlation between the binding energy loss and the kinetic energy carried by the nucleons released, as it will be discussed later.

It is worth saying that there is another contribution to invisible energy. The kinetic recoil energy of the struck nucleus in the spallation process, in fact, is generally too small to generate a signal, thus going to contribute to the amount of invisible energy.

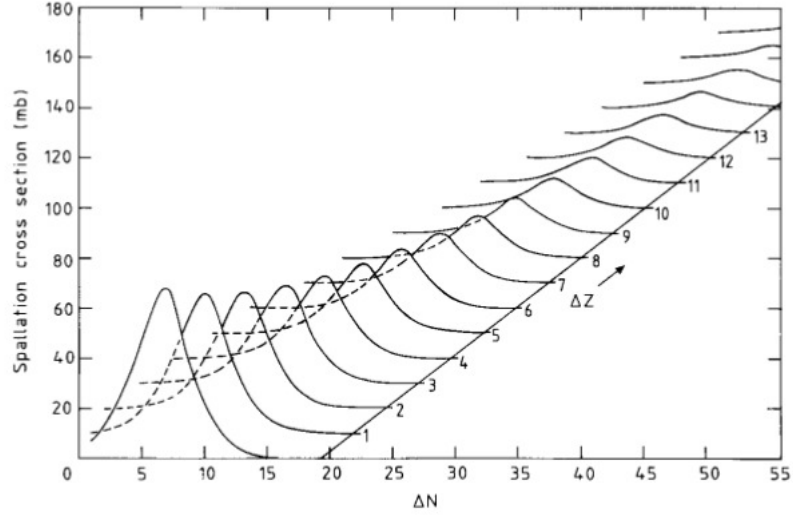


**Figure 13:** Cross sections for nuclides produced by spallation of  $^{238}\text{U}$ , induced by a 2 GeV hadron. The final-state nuclide is defined by the number of protons ( $\Delta Z$ ) and neutrons ( $\Delta N$ ) released from the target nucleus. [1]

**Table 1:** Energy deposit and composition of the non-em component of hadronic showers in lead and iron. The listed number of particles are per GeV of non-em energy. [1]

	Lead	Iron
Ionization by pions	19%	21%
Ionization by protons	37%	53%
<i>Total ionization</i>	56%	74%
Nuclear binding energy loss	32%	16%
Target recoil	2%	5%
<i>Total invisible energy</i>	34%	21%
Kinetic energy evaporation neutrons	10%	5%
Number of charged pions	0.77	1.4
Number of protons	3.5	8
Number of cascade neutrons	5.4	5
Number of evaporation neutrons	31.5	5
Total number of neutrons	36.9	10
Neutrons/protons	10.5/1	1.3/1

The energy deposit and the composition of the non-em component of hadronic showers in lead and iron are presented in Table 1. By inspecting this table, one immediately notices that, in the case of lead, there is a high discrepancy between the number of protons and that of neutrons, which is almost absent in the case of iron. Moreover, the total number of nucleons released in collisions with iron nuclei is substantially smaller than that for collisions with lead nuclei at the same energy. The former fact can be simply explained considering the Coulomb barrier which keeps protons in an excited nucleus in the evaporation stage: in the case of lead, this barrier amounts to  $\sim 12$  MeV, while in iron it amounts to only  $\sim 5$  MeV. For this reason there is not so much difference, for an excited Fe nucleus, between the probability of emitting a proton or a neutron. The discrepancy in the total number of nucleons released, instead, is due substantially to two effects. Firstly, the difference in nuclear binding energy, which is higher in iron. Secondly, the different proton/neutron ratios in the nuclei. In lead ( $Z/A=82/108$ ) protons bring  $\sim 39\%$  of the energy transported by escaping spallation nucleons, while in iron ( $Z/A=26/56$ ) this fraction amounts to 46%. Therefore, since protons lose their kinetic energy by ionization, in the case of lead absorbers a larger fraction of the available energy can be used for nuclear excitation, with the subsequent release of evaporation neutrons.

Some other considerations arise by observing Table 1:

- charged pions are less important in the absorption process with respect to protons;
- soft spallation protons, on the contrary, are more important in the absorption process, depositing about the 40% of the non-em energy;
- there is a large fraction of invisible energy;
- a large number of soft neutrons is produced in the shower development.

As previously said,  $\sim 10\%$  of hadronic shower particles are 3 MeV evaporation neutrons. These particles may travel several cm before interacting (differently from 50-100 MeV spallation protons, the range of which is about 1 cm) and deposit their energy only through nuclear interactions. There are various mechanisms through which evaporation neutrons lose their kinetic energy and are eventually absorbed in dense matter. Elastic scattering with the nuclei is the dominant process at energies between a few eV and  $\sim 1$  MeV. Inelastic scattering, which strongly depends on the details of the nuclear structure of the material, becomes significant, in the case of lead, at energies higher than 2.6 MeV. When neutrons are thermalized, *i.e.* they have lost almost all of their kinetic energy in collisions with the material, they can decay or get captured by an atomic nucleus.

Elastic scattering is in practice the process through which most of the kinetic energy carried by neutrons is deposited. The products of an elastic scattering reaction are a recoil nucleus and a lower-energy neutron. A very remarkable consideration to do is that the efficiency of elastic scattering processes for slowing down the neutrons is related to the mass of the absorber nuclei. In particular, neutrons transfer on average a higher amount of energy the smaller is the mass of the absorber nuclei. Obviously, hydrogen results to be the most efficient medium in thermalizing neutrons and this fact has an important application in calorimetry (see Section 1.5.4).

#### 1.4.2.4 Hadronic shower profiles

As previously hinted, there are some similarities between hadronic and electromagnetic longitudinal shower profiles. Also in the hadronic case, we have an initial approximatively linear rise of the number of shower particles traversing a small thickness of the absorber medium (and of the energy deposited in this thickness), followed by a much softer decay after the shower maximum. The latter changes for different particles and depends on the particle energy.

A major difference between the two kinds of showers is given by their scales, being the nuclear interaction length much larger than the radiation length (up to 30 times for high-Z materials). This difference is exploited in order to distinguish them, for example, by positioning in front of the calorimeter a preshower detector. This latter can simply be a piece of lead (0.5 cm thick) followed by a sheet of plastic scintillator. Because of the different scaling, pions will release a small fraction of their energy in it, while electrons will initiate a shower. Comparing the energy distributions, as showed in Figure 14, it is very easy to distinguish the two kinds of showers.

As for em showers, the calorimeter depth necessary to contain hadronic showers to a certain level increases logarithmically with energy but, because of the larger scaling, much more material is requested. For example, to contain a 300 GeV  $\pi^-$  shower at the 95% level, 85 cm of uranium are needed, *vs.* the 10 cm requested to contain an em shower generated by electrons of the same energy.

Concerning the lateral profile, this is also substantially broader with respect to the em one. A narrow core, surrounded by a halo, is often a peculiarity of the lateral profile of hadronic showers, as it can be seen in Figure 15. This lateral profile, measured with the SPACAL detector, has been integrated over the full depth of the absorber. The narrow core represents the em shower component, while the halo, the intensity of which has an exponential decay with the distance from the shower axis, represents the non-em component. In fact, the em core is caused by  $\pi^0$ s produced in the shower development, which originate em showers and deposit their energy in a much smaller detector volume with respect to other shower particles with the same

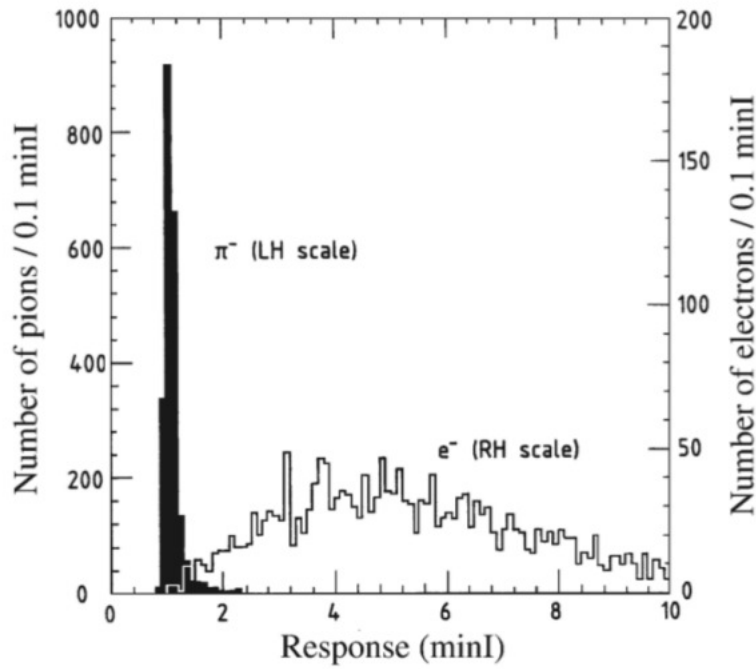


Figure 14: Signal distributions for 75 GeV  $\pi^-$  and  $e^-$  in a very simple preshower detector. [5]

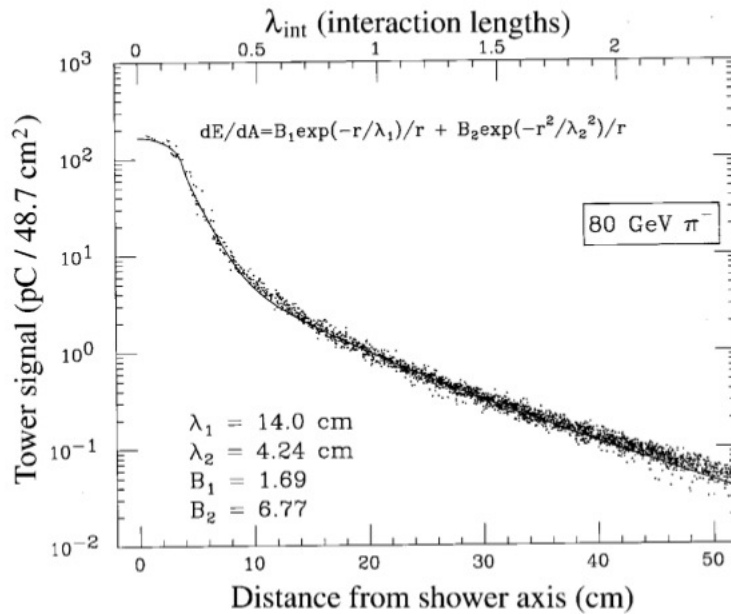


Figure 15: Average lateral profile of the energy deposited by 80 GeV  $\pi^-$  showering in the SPACAL detector. The collected light per unit volume is plotted as a function of the radial distance to the impact point. Data from [4].

energy. The energy density is therefore much larger in regions where  $\pi^0$ s are produced, which occurs mostly near the shower axis, in the earlier stages of the shower development. This can be seen from Figure 16, which shows the lateral profiles at different depths obtained by the ZEUS Collaboration in their uranium/plastic-scintillator calorimeter, with a 100 GeV pions beam.

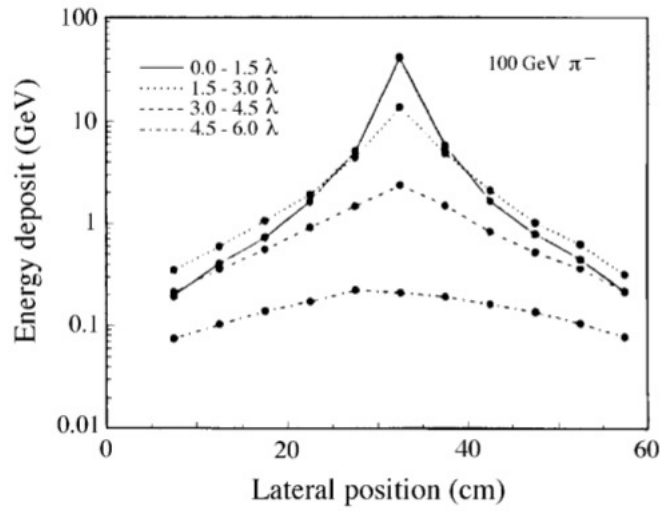


Figure 16: Lateral profiles for pion-induced showers, measured at different depths, with the ZEUS calorimeter. Data from [7].

Differently from em showers, hadronic ones have a wide variety of profiles that varies event-by-event, as it can be seen in Figure 17. The different shapes of the profiles are the result of the production of energetic  $\pi^0$ s, in the second or third generation of the shower development, in different regions of the absorbing volume. All the previously showed shower profiles were the result on an average over a large number of showers.

The tail of longitudinal and lateral shower profiles is actually dominated by evaporation neutrons, because of their longer mean free path. For this reasons, calorimeters which measure the contribution of neutron signals, a fundamental procedure in order to achieve *compensation*, as it will be discussed later, need to integrate over a large volume and a long time.

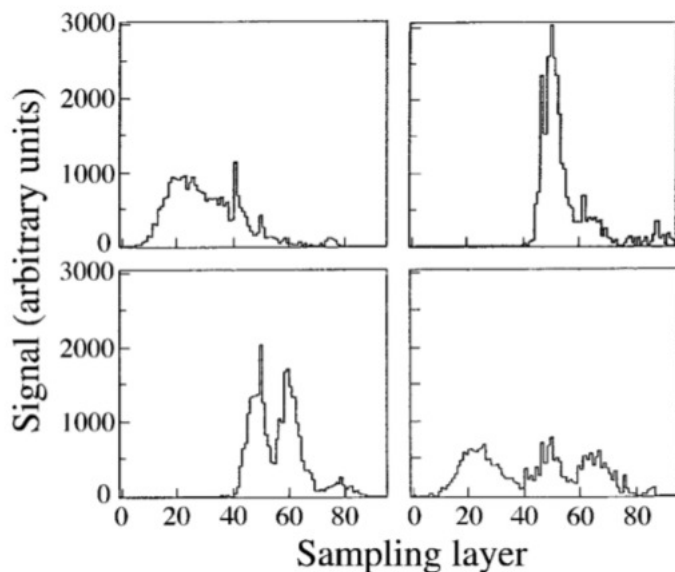


Figure 17: Longitudinal profiles for 4 different showers induced by 270 GeV pions in a lead/iron/plastic-scintillator calorimeter. Data from [6].

## 1.5 THE ENERGY RESPONSE OF CALORIMETERS

In the previous sections, the wide variety of processes responsible for the absorption of highly energetic particles in dense material has been described. In this section the way in which these phenomena are actually exploited, with calorimetric methods, in order to get information about particle properties will be discussed.

First of all, one has to define the *calorimeter response*, *i.e.* the average calorimeter signal divided by the energy of the particle that caused it. This quantity can be expressed in units of *number of photoelectrons per GeV*, or *picocoulombs per MeV*, depending on the calorimeter system.

Calorimeter responses to different types of particles are often compared. In this context, minimum ionizing particles (*mips*) serve as "benchmark particles": the ratio  $X/mip$ , *i.e.* the ratio between the calorimeter response for particles of type  $X$  and that for *mips*, is used to express the calorimeter response for  $X$  particles. Charged particles can be temporarily considered as *mips* when their stopping power is at its minimum value (see Figure 1). Muons are usually considered *mips*, even if this ceases to be true at relativistic energies, when their energy loss becomes greater than the minimum value.

A calorimeter in which there is proportionality between the average signal for the detection of electrons and the electron energy has an electromagnetic response that is constant as a function of energy and it is said to be *linear* for em shower detection.

A very suitable way to present calorimeter (non-)linearity data is to plot the calorimeter response as a function of energy, as it can be seen in Figure 18, which will be described shortly.

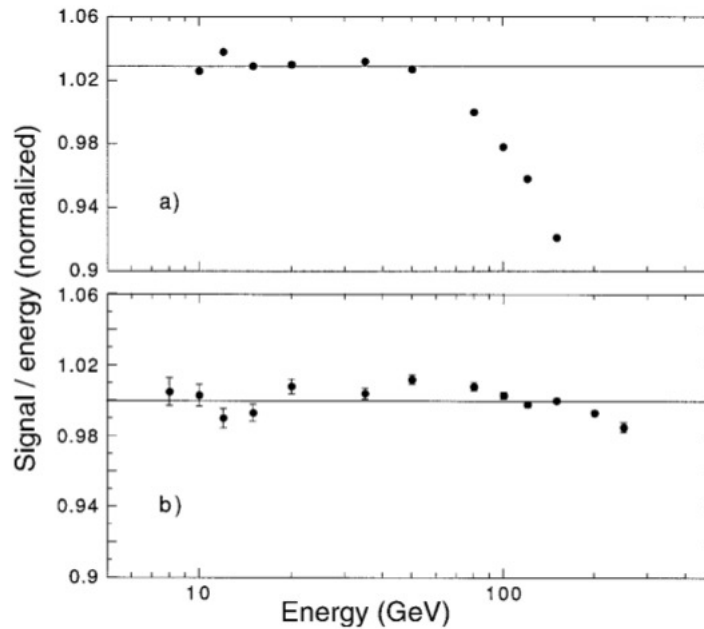


**Figure 18:** The em calorimeter response as a function of energy, measured with the QFCAL calorimeter, before (a) and after (b) precautions were taken against PMT saturation effects. Data from [21].

As it was said in the first section of this chapter, calorimeters can be of different types: homogeneous and sampling. The former ones have their entire volume sensitive to particles and thus contributing to produce the detector signals. Therefore the material which composes the counter performs both the function of absorbing the particles and that of generating the signals produced in this process. Sampling calorimeters, instead, are made of different materials, the absorber (passive medium) and the active medium, which perform separately the functions of absorbing particles and generating signals.

#### 1.5.1 Non-linearity for electromagnetic showers

Both homogeneous and sampling calorimeters should be intrinsically linear for em shower detection, since in this case all the kinetic energy of the incoming photon or electron is used to generate the calorimeter signal. Unfortunately, in many cases deviations from intrinsic linearity are observed and this fact can be due to a variety of reasons. Some of them are listed in the following.

- Saturation effects in the PMTs, since the electric current created in the PMT lowers the potential differences between the dynodes, particularly in the region where the current is largest, *i.e.* in the last amplification stage. Lowering the PMT gain represents a way to reduce this effect, as well as stabilizing the voltage differences between the PMT dynodes using separate power supplies, thus keeping the PMT amplification constant. Figure 18 shows the response of the QFCAL calorimeter before and after precautions of this type were taken. It can be seen in Figure 18b that the response became constant to within  $\sim 1\%$  over the energy range 8-250 GeV.
- Saturation effects resulting from shower particle density, occurring in calorimeters in which the ionization charge is collected by gaseous detectors operating in "digital" mode, such as Geiger counters. In these detectors the em response depends on the density of shower particles.
- Shower leakage effects, resulting in a response which decreases with increasing energy when the calorimeter is not fully containing.
- Recombination of ions and electrons into atoms inside the absorber material.

### 1.5.2 Homogeneous calorimeters

Since muons and the shower particles produced in em shower development traversing a homogeneous calorimeter lose kinetic energy through the same mechanisms, the responses of such a calorimeter to muons and to em showers are equal. Therefore, for a homogeneous calorimeter the following relation holds:

$$e/mip = 1, \quad (22)$$

where  $e$  and  $mip$  indicate the calorimeter responses to em showers and minimum ionizing particles, respectively. As a consequence of this, the calibration constant, *i.e.* the relation between the deposited energy and the resulting calorimeter signal, obtained with em showers can also be applied to signals generated by muons.

#### 1.5.2.1 The response to hadrons and jets

Electromagnetic calorimeters should be linear at the 1% level. This is not the case of hadronic calorimeters. In fact, because of the invisible energy phenomenon, only a fraction of the energy carried by hadrons and jets contribute to the calorimeter signal. Homogeneous calorimeters are therefore intrinsically non-linear for the detection of hadrons and jets. The latter are collection of particles, resulting from

the fragmentation of a quark, a diquark, or a hard gluon produced in the collisions. All the particles which constitute a jet tend to travel in approximately the same direction, particularly at high energies. The measurement of the jet properties, from which the four-vectors of the fragmenting particle can be deduced, is in some experiments preferred to that of individual hadrons.

As previously discussed, the energy of the non-em shower component is distributed, in an energy-independent way, between mesons, spallation protons, evaporation target neutrons, recoil target nuclei and nuclear  $\gamma$ s. In the following discussion,  $h$  will indicate the calorimeter response to the non-em component of hadronic showers,  $e$  the electromagnetic response and  $\pi$  the response to pions.

The signals generated by pions of a given energy result, on average, smaller than those generated by electrons of the same energy, if the same calibration constant is used. This fact is due to the invisible energy phenomenon, since only a fraction of the energy carried by these particles contributes to the signal and it may be written as

$$\pi/e < 1 \quad (23)$$

Besides being smaller with respect to the em one, the response to hadron-induced showers is also energy-dependent, owing to the em fraction of hadronic showers. This latter, which is caused by  $\pi^0$ s produced in the shower development, as it was discussed in Section 1.4.2, increases with increasing energy and so does the calorimeter response to hadronic showers. In other words, it can be said that the  $\pi/e$  ratio increases with energy and at very high energies this ratio approaches 1.

The distribution of the non-em energy between the various components of the non-em shower is energy independent, therefore  $h$  may be considered constant. Obviously, because of invisible energy,  $h$  is smaller than  $e$ , that is:

$$e/h > 1 \quad (24)$$

If this relation is verified, the calorimeter is said to be *non-compensating* and the ratio  $e/h$  indicates the degree of non-compensation. All homogeneous calorimeters are non-compensating. Since part of the pion-induced showers is of electromagnetic nature, and the  $f_{em}$  increases with energy, the  $e/\pi$  ratio is not indicative for the degree of non-compensation.

The  $e/h$  ratio, which can't be directly determined from experimental data, can be derived from the knowledge of the average  $f_{em}$  and from measurements of the  $e/\pi$  signal ratios at different energies. In fact, the response to pions can be written as

$$\pi = f_{em} \cdot e + (1 - f_{em}) \cdot h, \quad (25)$$

which leads to

$$\pi/e = f_{em} + [1 - f_{em}] \cdot h/e \quad (26)$$

By inverting the previous relation, one gets the following expression, which links the measured  $e/\pi$  signal ratio with  $e/h$ :

$$e/\pi = \frac{e/h}{1 - f_{em}[1 - e/h]} \quad (27)$$

Figure 19 shows the relationship between the calorimeter response ratio to em and non-em shower components ( $e/h$ ) and measured  $e/\pi$  ratio, for a variety of  $e/h$  values ranging from 0.8 to  $\infty$ . In order to calculate the energy dependence of the  $f_{em}$ , Equation 20 has been used. The fact that, in the high-energy limit, the  $e/\pi$  signal ratio approaches 1, independently from the  $e/h$  ratio, as previously said, is well illustrated in the figure.

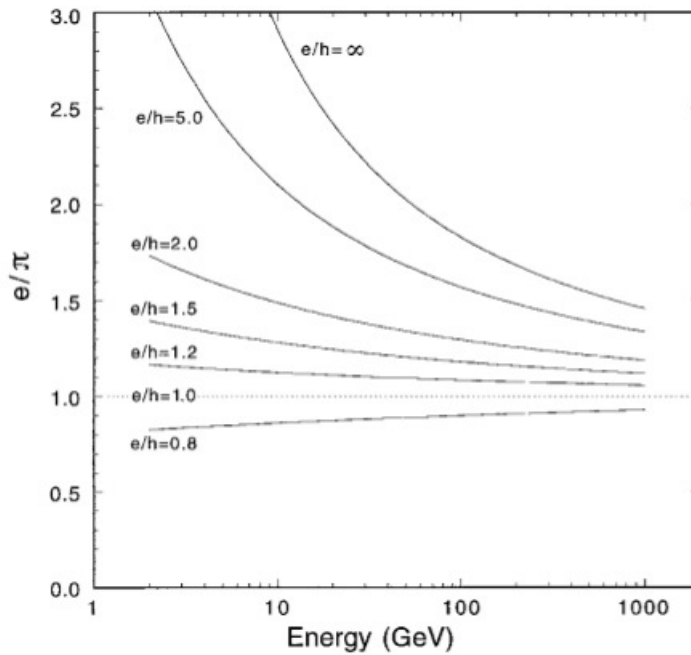


Figure 19: The relation between the calorimeter response ratio to em and non-em energy deposition,  $e/h$ , and the measured  $e/\pi$  signal ratios. [1]

The situation for jets is very similar, since the absorption of jets proceeds in approximately the same way as that of individual hadrons, *i.e.* some fraction of the energy carried by the jet particles is deposited in the form of em showers, the rest in non-em form. A small difference is that there is an intrinsic electromagnetic jet component, owing to the fact that jets usually contain a certain number of  $\gamma$ s from  $\pi^0$  decay before entering the calorimeter, while the em component of hadronic showers originates from  $\pi^0$  decay which happens inside the calorimeter volume. Moreover there may be a difference between the

average  $f_{em}$  for jets and that for individual hadrons with the same energy of the jet, because of the fragmentation process. In fact, in a diquark fragmentation the leading particle will be a baryon, while in a quark fragmentation the leading particle will be most likely a meson. Heavy quarks ( $c, b$ ) will produce with higher probability light quarks ( $u, d$ ) than leading  $\pi^0$ .

Anyway, as in the case of individual hadrons, the response of homogeneous calorimeters to jets is significantly smaller than that to electrons, photons and muons. Again, the response is energy dependent, implying considerable signal non linearities.

### 1.5.3 Sampling calorimeters

One important parameter which characterizes sampling calorimeters is the *sampling fraction*. It is defined as the energy deposited by minimum ionizing particles in the active calorimeter layers, relatively to the total energy deposited by such particles in the calorimeter.

#### 1.5.3.1 The response to electrons and photons

In sampling calorimeters, the relation  $e/mip = 1$  previously discussed in the case of homogeneous calorimeters has no more validity. In particular, it results from experimental data that the ratio  $e/mip$  is less than 1 and it decreases if the difference between the  $Z$  values of the active and the absorber media increases, becoming the  $Z$  of the absorber much larger than that of the active medium. The suppression of the em signal in sampling calorimeters is known as *transition effect* since it is due to phenomena which occur at the boundary between layers of material with different  $Z$ . More precisely, since the soft shower  $\gamma$ s which dominate em shower signals lose their energy predominantly through photoelectric effect, which has a  $Z^5$  cross section dependence, such particles will interact mostly in the high- $Z$  absorber material. Besides, the range of electrons produced in the  $\gamma$  interactions is much shorter than the distance between two adjacent sampling layers. Therefore, one can expect that soft shower  $\gamma$ s contribute to the signal only if they interact sufficiently close to the boundary with an active layer, so that the photoelectron can enter in the active medium.

In order to overcome the problem of the em signal suppression, the sampling fraction can be increased, by making the calorimeter absorber layers thinner.

It is important to notice that, in order to understand the characteristics of sampling calorimeters, a fundamental contribution has been given by Monte Carlo simulations. Figure 20, obtained using EGS4 shower simulation program, shows the  $e/mip$  ratio as a function of the

absorber layers for two uranium calorimeters, one with scintillating plastic (PMMA) as active medium, the other with liquid argon. It can be seen that the ratio has a significant increase when the layers become thinner than about 5 mm.

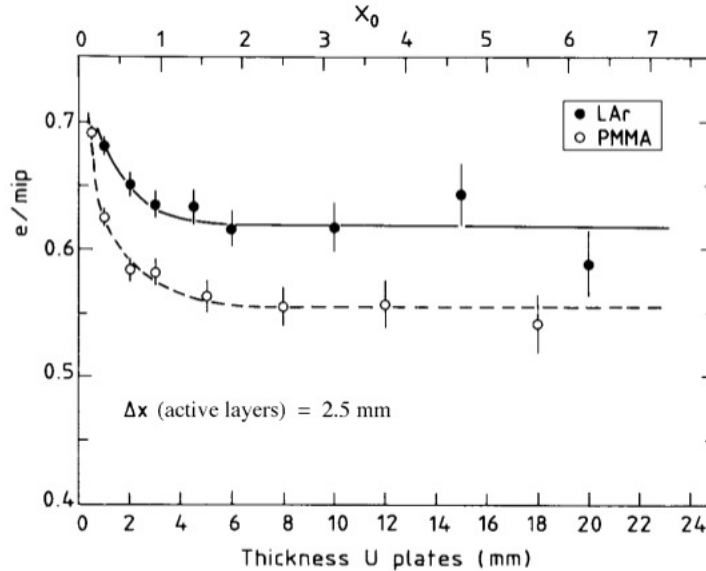


Figure 20: The  $e/mip$  ratio as a function of the thickness of the absorber layers, for uranium/PMMA and uranium/LAr calorimeters. The thickness of the active layers is 2.5 mm in all cases. Results from EGS4 Monte Carlo simulations. [8]

### 1.5.3.2 The response to hadrons

For low-energy hadrons the sampling calorimeters response to their interactions is substantially the same as in the case of homogeneous calorimeters. At energies below 1 GeV hadrons lose their kinetic energy more likely through ionization or excitation of the atoms or molecules of the medium, thus behaving similarly to  $mips$ . Increasing the hadrons energy,  $\pi^0$  production becomes more important and therefore the response to hadrons becomes more similar to the response to the one for em showers. In other words, one can say that, for any kind of calorimeter, at very high energies the  $e/\pi$  signal ratio approaches 1, independently from the degree of compensation. Besides, a calorimeter which has the ratio  $e/mip \neq 1$  and a response to hadrons similar to that of  $mips$  at low energies and to the one for em showers at high energies is by definition non-linear for hadrons, independently from the degree of compensation.

It was previously said that all homogeneous calorimeters have  $e/h$  values larger than one. In particular such values range from 1.5 to 2.5, depending on the  $Z$  values of the components and on the cross-section for neutron-induced reactions. In the case of sampling calori-

meters, the  $e/h$  range is wider.

Most of sampling calorimeters have  $e/h > 1$ , but compensating calorimeters have  $e/h \sim 1$  and there have been even examples of sampling calorimeters with  $e/h < 1$ , meaning that the hadronic response for such calorimeters decreased with increasing energies.

Anyway, it is true that the  $e/h$  value of the calorimeter determines the signal non-linearity. For this reason, a method used to derive such ratio is the measurement of the hadronic signal non-linearity (see Figure 19). In order to do so, one has to know the energy dependence of the average em shower fraction,  $f_{em}(E)$ . The following equation gives the relation between the ratio of pion responses at energies  $E_1$  and  $E_2$  and the  $e/h$  value, assuming linearity for em shower detection:

$$\frac{\pi(E_1)}{\pi(E_2)} = \frac{f_{em}(E_1) + [1 - f_{em}(E_1)](e/h)^{-1}}{f_{em}(E_2) + [1 - f_{em}(E_2)](e/h)^{-1}} \quad (28)$$

It will be seen in the following section that hadronic signal linearity is only one of the many advantages of compensating calorimeters, that is calorimeters whose responses to em and non-em components of hadronic showers are equal.

Concerning the non-em calorimeter response, this is due to mechanisms of energy deposition by substantially three classes of particles:

- relativistic hadrons (mainly charged pions);
- non-relativistic hadrons (mainly spallation protons);
- evaporation neutrons, with energies of typically a few MeV.

Besides, one has to consider the contribution of invisible energy.

If we indicate with  $f_{rel}$ ,  $f_p$ ,  $f_n$  and  $f_{inv}$  the fraction of the non-em shower energy carried by the previously mentioned mechanisms respectively, one has the following relation:

$$h = f_{rel} \cdot rel + f_p \cdot p + f_n \cdot n + f_{inv} \cdot inv, \quad (29)$$

where  $h$  is the calorimeter response to the non-em shower component and  $rel$ ,  $p$ ,  $n$  and  $inv$  are the responses to the various components. Of course one has:  $f_{rel} + f_p + f_n + f_{inv} = 1$ .

A relation between the  $e/h$  value of a given calorimeter and its responses to the non-em shower components can be derived from Equation 29, once normalized all the responses to the one for mip and eliminated the invisible energy term:

$$\frac{e}{h} = \frac{e/mip}{f_{rel} \cdot rel/mip + f_p \cdot p/mip + f_n \cdot n/mip} \quad (30)$$

Combining Equations 26 and 30 one can write the response to pions relative to that to electrons in the following way:

$$\frac{\pi}{e} = f_{em} + [1 - f_{em}] \frac{f_{rel} \cdot rel/mip + f_p \cdot p/mip + f_n \cdot n/mip}{e/mip} \quad (31)$$

Since the average em shower fraction  $f_{em}$  is energy dependent, this response is also energy dependent and the previous equation is valid for energies  $>3$  GeV, when pions are more likely to undergo nuclear interactions rather than to ionize the medium. In the latter case, in fact, their response would be similar to that for mips.

Figure 21 shows the hadronic response of liquid-argon calorimeters, with iron and lead absorbers, calculated by considering all the different factors.

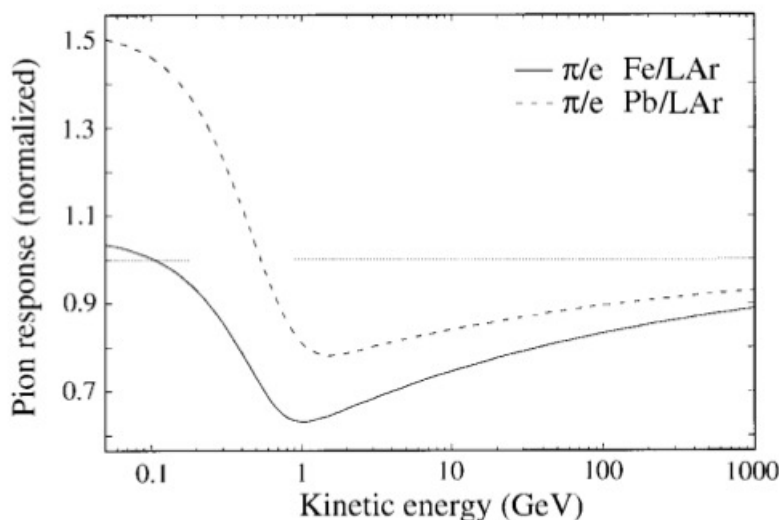


Figure 21: The calculated response of iron/LAr and lead/LAr calorimeters to pions, as a function of energy. [1]

Concerning the response to jets, the situation for sampling calorimeters is substantially the same for homogeneous ones, which has been described in Section 1.5.2.1.

#### 1.5.4 Compensation

As it has been remarked more than once in this chapter, the response of a given calorimeter to hadrons is smaller than that to electrons of the same energy, because of the invisible energy phenomenon. Since non-compensation gives rise both to a signal non-linearity and to a degradation of the energy resolution of the calorimeter, it would be desirable to achieve a *compensation* for the invisible energy loss.

The  $e/h$  value of a calorimeter is given by Equation 30 in terms of the different em and non-em signal components. All homogeneous calorimeters are undercompensating, that is their  $e/h$  is always less than one, in a usually considerable way. That's because for such calorimeters the responses to the non-em shower components can be at

best equal to that to the em components.

Sampling calorimeters, on the other hand, offer the possibility to achieve compensation, that is to obtain the value  $e/h=1$ , by choosing appropriately the parameters  $e/mip$ ,  $p/mip$  and  $n/mip$  in Equation 30. In fact,  $f_{rel}$ ,  $f_p$  and  $f_n$  are fixed by the choose of the active and passive media of the calorimeter, while the value  $rel/mip$  is equal to 1, since the relativistic charged hadrons give the same signal as mips in the calorimeter active layers.

The achievement of compensation can be pursued by means of different methods, which involve the reduction of the em response ( $e/mip$ ) or the increase of the non-em response ( $n/mip$ ,  $p/mip$ ).

By choosing high-Z absorber materials, one can reduce the electromagnetic response of sampling calorimeters. This is due to the behaviour of soft photons, as it has been explained in Section 1.5.3.1.

The most effective way to obtain compensation, valid for calorimeters whose active medium contains hydrogen, is to enhance their response to neutrons. The latter ones at low energies typically interact through elastic scattering with nuclei (see Section 1.4.2.3). In this process they transfer a fraction of kinetic energy which depends on the atomic number  $A$  of the target nucleus, given by the relation:

$$f_{elastic} = \frac{2A}{(A+1)^2} \quad (32)$$

It's easy to see that in hydrogen this fraction is 50%, while in lead it is 100 times smaller. The presence of hydrogen in the active layers is, in fact, a key requirement in order to get compensation. If we consider a calorimeter made of a Pb/H<sub>2</sub> structure, with the same number of nuclei for the two components, MeV-type neutrons will release 98% of their energy to hydrogen nuclei and only 2% to lead. Considering that in such a calorimeter the sampling fraction for charged particles is equal to 2.2%, one has therefore the possibility to obtain a *signal amplification through neutron detection* (SAND). That's particularly due to the fact that the recoil protons which are produced in the active layers may also contribute to the calorimeter signal.

This is well illustrated by the case of the L3 uranium/gas calorimeter. Signal for pions and for electrons were measured with this calorimeter, using two different sampling gaseous media: argon/CO<sub>2</sub> and isobutane (C<sub>4</sub>H<sub>10</sub>). Figure 22 shows how the pion/electron response ratio changed by varying the hydrogen content of the gas mixture. It can be seen that the pion response doubled when isobutane was used instead of argon/CO<sub>2</sub>. Different gas mixtures have been tested by the L3 group and it resulted that, by choosing the most suitable mixture, one could equalize the responses to em and hadronic showers.

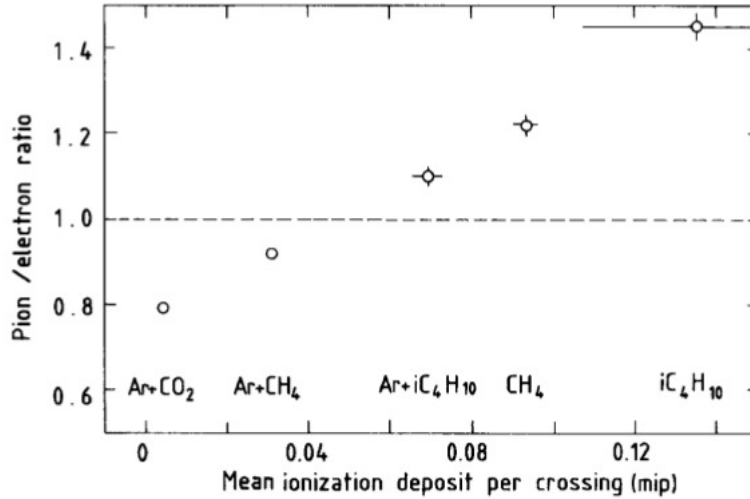


Figure 22: Pion/electron response ratio as a function of the hydrogen content of the gas mixture. [10]

Not necessarily the active medium of the calorimeter needs to be of gaseous type in order to obtain compensation, but it must contain hydrogen.

Hadronic signals measured with compensating calorimeters usually exhibit a tail, which is absent in electron signals, as it is shown in Figure 23, which concerns signal recorded with the compensating SPACAL calorimeter (lead/scintillating plastic fibers).

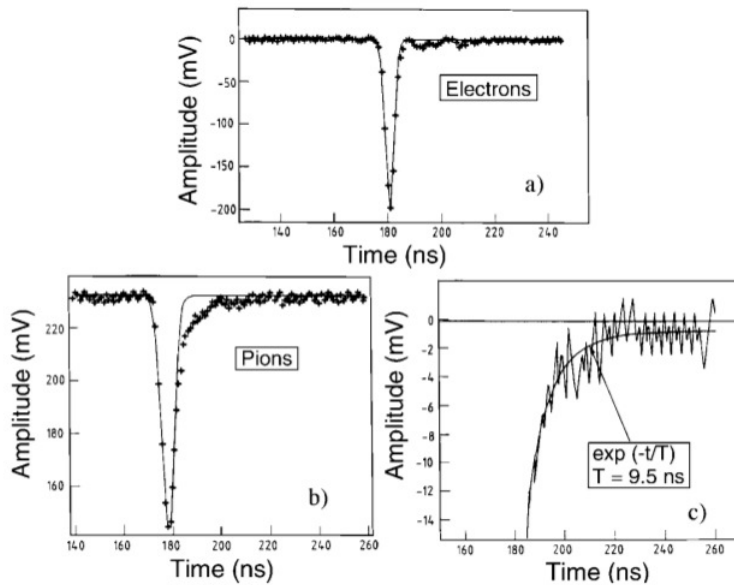


Figure 23: Typical signals for 150 GeV electrons (a) and pions (b) measured with the SPACAL calorimeter. The pion signal exhibits an exponential tail with a time constant of  $\sim 10$  ns (c). [11]

The presence of such tail is owed to the fact that neutrons contribute in a substantial way to the signals: the exponential law which well describes the tail has a slope of 10 ns, being the latter the characteristic time between subsequent elastic scattering processes of neutrons in this material combination.

## 1.6 FLUCTUATIONS

In order to obtain the energy of a particle detected by a calorimeter, the knowledge of the detector calibration and of the energy resolution of the calorimeter are needed. The former represents the relationship between the measured signals and the deposited energy, while the latter gives the precision with which one can measure the energy of a given particle. Both the calibration and the energy resolution of a calorimeter are obtained experimentally, by sending particles of known energy into the calorimeter. The resolution is deduced by the precision with which the energy of the particles is reproduced by the calorimeter signals.

The importance of knowing the energy resolution of a calorimeter can be easily understood if one considers that, in particle physics experiments:

- it may limit the precision with which the mass of a new particle can be determined;
- it may limit the separation between particles with similar masses (such as the jet-jet decay of the intermediate vector bosons  $W$  and  $Z$ );
- it is responsible of the signal-to-background ratio in event samples collected during the experiments.

Fluctuations in the processes through which the energy is deposited and the technique chosen to measure the final products of the cascade processes are responsible in limiting the precision in the measurement of the energy of showering particles. Fluctuations in the shower development are unavoidable.

The situation is different if one considers em or hadronic calorimeters. In the first case, the ultimate limit on the achievable energy resolution is given by fluctuations in the em shower development. For hadronic calorimeters, on the other hand, the chosen measurement techniques often don't affect the energy resolution, since intrinsic fluctuations in the hadronic shower development produce considerable event-to-event variations in the fraction of visible energy.

Most of the fluctuations, such as fluctuations in the number of quanta that constitute the detector signals (scintillation or Cherenkov photons, ion-electron or electron-hole pairs, *etc.*) are of Poissonian

type, even though some of them are not, *e.g.* shower leakage fluctuations. Poissonian fluctuations contribute to the energy resolution with a term which is proportional to  $1/\sqrt{E}$ .

The resolution of a given calorimeter is actually affected by various types of fluctuations. Each type of fluctuations has a peculiar energy dependence and, since these effects are generally uncorrelated, they have to be added in quadrature. A view of the various types of fluctuations which affect the calorimeters performance will be given in the following.

It is customary to express the energy resolution of a calorimeter as the sum in quadrature of three terms:

$$\frac{\sigma}{E} = \frac{a}{\sqrt{E}} \oplus \frac{b}{E} \oplus c, \quad (33)$$

where the first term (the *stochastic* term) is related to statistical fluctuations inherent the development of showers, the second term (the *noise* term) is due to instrumental effects (noise, pedestal) and the third term (the *constant* term) is due to calibration errors, non-uniformities and non-linearities in photomultipliers, proportional counters, ADC's, etc.

The total resolution of a calorimeter, therefore, may be dominated by different effects, depending on the energy regimes. The separate contributions of various effects to the ATLAS EM calorimeter are shown in Figure 24.

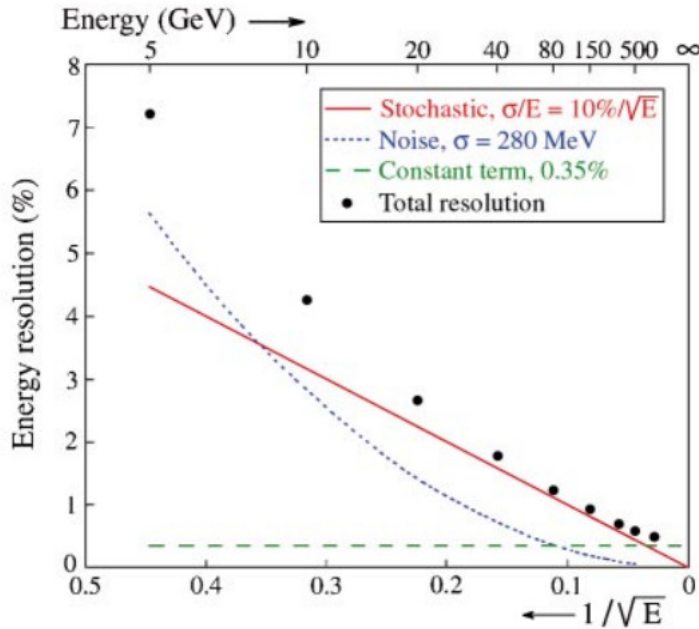


Figure 24: The em energy resolution and the separate contributions to it, for the ATLAS EM calorimeter. [20]

Therefore, in the design of a calorimeter, one has to identify which types of fluctuations dominate the performance and act in order to reduce them.

### 1.6.1 Signal quantum fluctuations

This kind of fluctuations is particularly important in detectors which exploit Cherenkov light detection, such as the detectors of the DREAM Project, which will be described in detail in the following chapters.

In fact, being the Cherenkov process much rarer than the others through which a particle may lose energy, in such detectors only a very small fraction ( $\sim 1\%$ ) of the shower energy is deposited in the active medium. Besides, another small fraction of the Cherenkov light manage to reach the photomultiplier tube devoted to its detection. Finally one has also to consider the quantum efficiency of the PMT tube, so that not all the Cherenkov photons reaching the photocathode will be converted into photoelectrons. In this regard, equipping the PMT with a quartz window, which has a quantum efficiency shifted to lower wavelengths, can be helpful, as it can be seen in Figure 25.

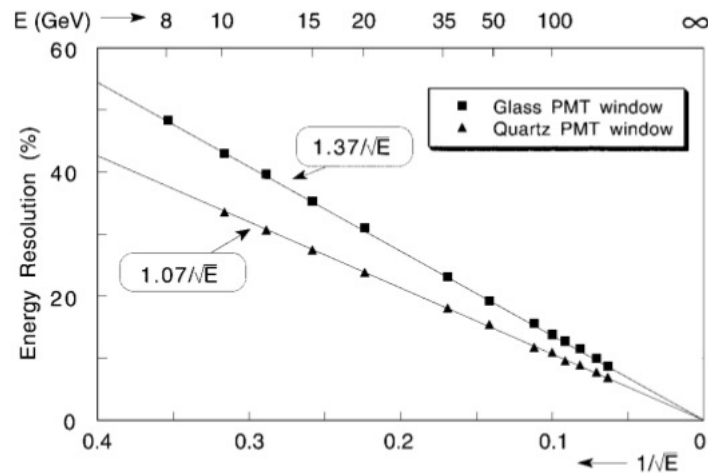


**Figure 25:** The energy resolution for electron detection with the QFCAL prototype detector, as a function of energy. Results are given for measurements in which photomultiplier tubes with a glass window were used and for measurements in which the same type of PMTs were equipped with a quartz window. [21]

As a result of all the previously mentioned effects, one has a very low Cherenkov light yield, of the order of 1 photoelectron per GeV. In these devices, fluctuations in the number of photoelectrons are therefore the dominating ones in these devices, strongly influencing the energy resolution.

### 1.6.2 Sampling fluctuations

In sampling calorimeters, fluctuations in the number of particles traversing the active calorimeter layers influence the energy resolution. Sampling fluctuations are governed by Poisson statistics.

In order to increase the fraction of shower energy deposited in the active medium, one may either add more active layers (with a certain thickness  $d$ ) in the calorimeter volume, *i.e.* increasing the *sampling fraction*  $f_{smp}$ , or reducing the thickness  $d$  for a given amount of active medium, *i.e.* increasing the *sampling frequency*.

Taking into account the previous considerations, one may write the contribution of sampling fluctuations to the energy resolution of an electromagnetic calorimeter with non-gaseous active medium as:

$$(\sigma/E)_{smp} = a\sqrt{d/f_{smp}} \cdot \frac{1}{\sqrt{E}} \quad (34)$$

where  $a$  is a constant term.

Figure 26 concerns data from different types of calorimeters used in past experiments. In this figure one can see that the sampling fluctuations contribution is well described by the constant term  $a=2.7\%$ , provided that the thickness  $d$  of the active layers or fibers is expressed in mm and  $f_{smp}$  is the sampling fraction for mips.

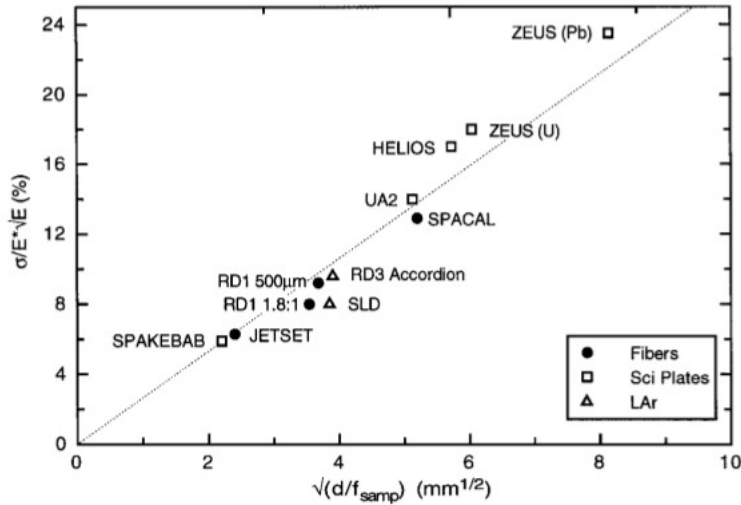


Figure 26: The em energy resolution of sampling calorimeters as a function of the parameter  $(d/f_{smp})^{1/2}$ . [22]

It is worth to notice how the energy resolution of fiber calorimeters is much better compared to the one of plate calorimeters (such as plastic-scintillator plate calorimeters), as it can be seen in Figure 27. This is because both the number of different active elements in a given volume and the total surface of the boundary between active and passive layers are much larger in the fiber calorimeter case.

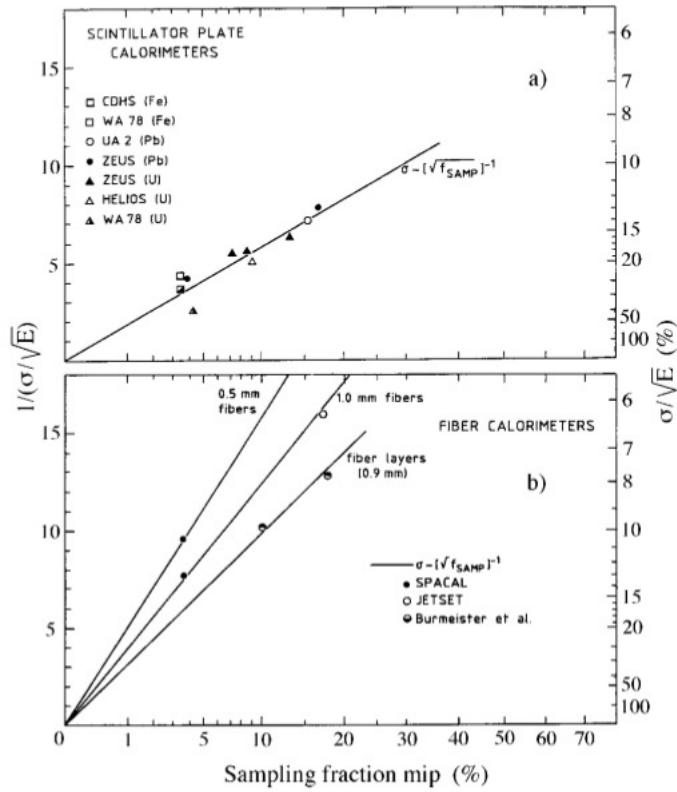


Figure 27: The em energy resolution (see right scale) as a function of the sampling fraction for various representative plastic-scintillator calorimeters (a) or for scintillating-fiber calorimeters (b). [22]

### 1.6.3 Instrumental effects

Imperfections both in the calorimeter construction and in the setup environment lead to instrumental effects which contribute to the energy resolution of the calorimeter with a non-Poissonian term. A wide variety of such effects exists, the ones which mainly influence fiber calorimeters are listed in the following.

- *Electronic noise.* This effect contribute to energy resolution with a term which scales as  $E^{-1}$ . In calorimeters based on scintillation light detection, like DREAM, electronic noise manifests as the accumulation of charge during the gate time of the Analog to Digital Converter (ADC), with which the PMTs signals are digitized and analyzed, even when the PMTs signals are absent. This "pedestal" signal has to be subtracted by the raw signal.
- *Variations in sampling fraction.* This effect depends on the type of calorimeter. Concerning fiber calorimeters, an example is offered by the SPACAL calorimeter [23]. SPACAL was made of

a lead matrix in which plastic scintillating fibers with a diameter of 1 mm were embedded. The lateral cross section of it is shown in Figure 28(a). With such device one may notice how the sampling fraction of the calorimeter is position dependent for narrow showers. In fact, it is different if the impact point of the particle is in the fiber plane or between two fiber planes. In the former case, a larger part of the shower is sampled with respect to the latter. This effect can be seen in Figure 28(b), which shows the SPACAL signal as a function of the impact point. In order to counteract this effect, it can be useful to tilt slightly the detector from  $0^\circ$  with respect to the direction of the incident particles and using fibers with a small radius.

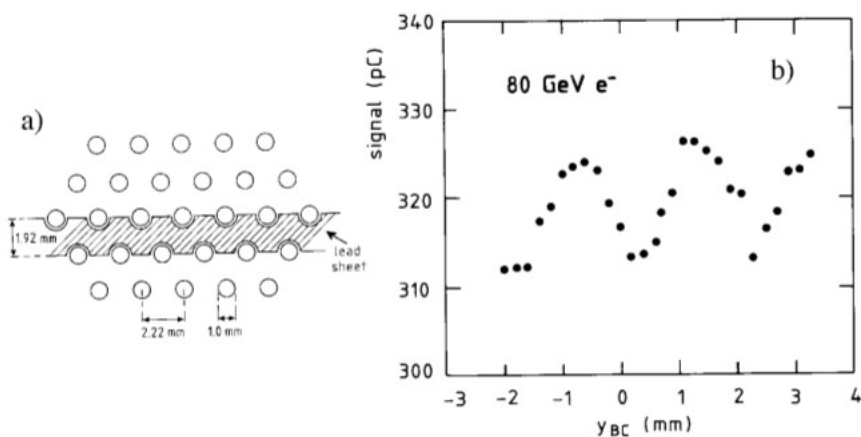


Figure 28: Lateral cross section of SPACAL (a). The SPACAL signal as a function of the  $y$ -coordinate of the impact point (b). Data for 80 GeV electrons. [23]

Besides, fiber calorimeters are also affected by channelling effects, which lead to anomalous signals when the particles enter the calorimeter in the exact position of a fiber. Again, tilting the detector can be a useful way to counteract these effects.

- *Non-uniformity of active elements.* In fiber calorimeters, one has to consider fiber-to-fiber thickness fluctuations as well as the fact that PMTs quantum efficiency is position dependent. Besides, light attenuation may also play an important role. It can be caused, for example, by self-absorption in the active media and gives rise to a position dependence of the signals from the distance between the point in which light is produced and the point in which it is detected.

## 1.6.4 Shower leakage

The incomplete containment of particle showers in a calorimeter leads to energy dependent event-by-event fluctuations in the shower leakage, thus affecting the energy resolution of the device. These fluctuations are of non-Poissonian type. Besides, in the context of a  $4\pi$  experiment, the escape of particles from the calorimeter has to be minimized, in order to avoid that the escaping particles release signal in other detectors.

Shower leakage depends both on the energy and on the nature of the particles traversing the calorimeter. Hadrons are less contained with respect to electrons of the same energy.

There are three types of shower leakage: *longitudinal* leakage, *lateral* leakage and *albedo*.

For a given level of shower containment, longitudinal leakage fluctuations contribute much more to energy resolution than lateral ones, as it can be seen in Figure 29. The reason for such behaviour is that, while side leakage is a collective phenomenon and therefore has contributions from a large number of shower particles, longitudinal leakage fluctuations may be owed to fluctuations in the starting point of a photon-induced shower. In the latter case, only one particle, *i.e.* the initial photon, is responsible of the fluctuations.

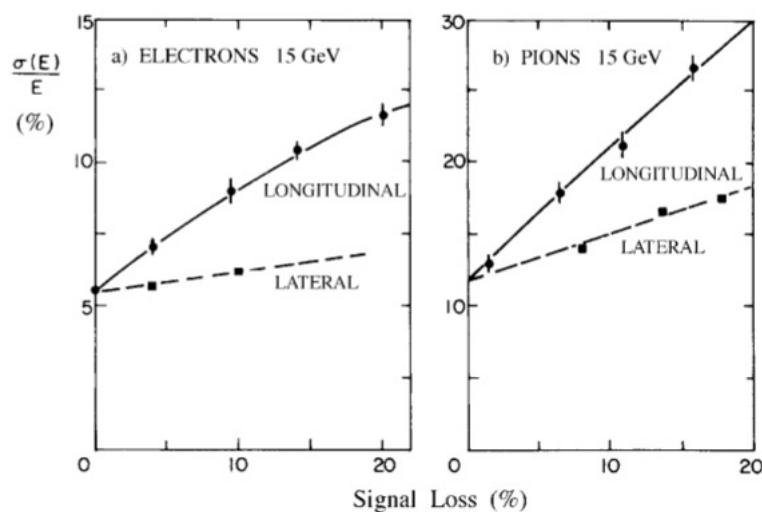


**Figure 29:** The effects of longitudinal and lateral shower leakage on the energy resolution, as measured for 15 GeV electrons (*a*) and pions (*b*) by the CHARM Collaboration in a low- $Z$  calorimeter. [24, 25]

The albedo, whose effects are usually very small, consists in backward leakage through the front face of the detector. The design of the calorimeter can't avoid in any way this phenomenon.

A comparison of the effects of the three types of shower leakages, obtained by means of Monte Carlo simulation is shown in Figure 30.

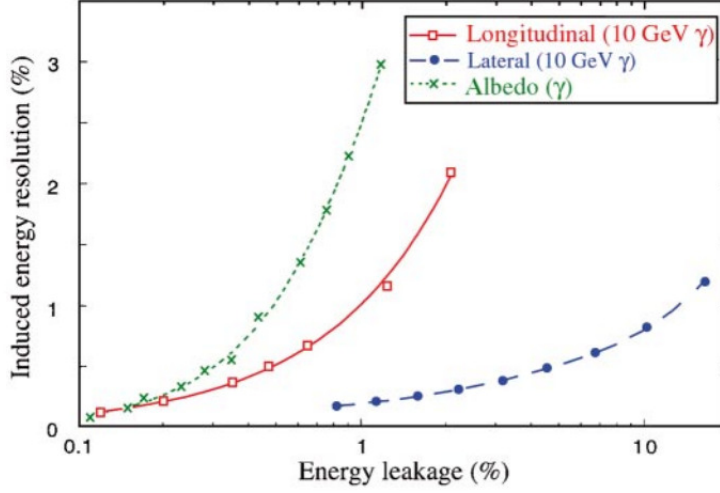


Figure 30: A comparison of the effects caused by different types of shower leakage. Shown are the induced energy resolutions resulting from albedo, longitudinal and lateral leakage as a function of the energy fraction carried by the particles escaping from the detector. Results from EGS4 Monte Carlo calculations. [5]

### 1.6.5 Fluctuations in hadronic showers

When considering hadronic calorimeters, besides all the previously mentioned effects, one has to take into account of two types of fluctuations which are peculiar of hadronic showers: fluctuation in *visible energy* and fluctuations in the *em shower content*.

The first ones are related to the phenomenon of "invisible energy", which was described in Section 1.4.2. These fluctuations ultimately limit the resolution of compensating calorimeters to a value which is approximately  $15\%/\sqrt{E}$  for compensating calorimeters.

Event-to-event fluctuations in the electromagnetic shower content,  $f_{em}$ , tend to dominate the hadronic performance in non-compensating calorimeters. They are of non-Poissonian type and contribute to the energy resolution with a term which scales as  $cE^{-0.28}$ , where the parameter  $c$  is determined by the  $e/h$  value. The hadronic energy resolution for non-compensating calorimeters may therefore be expressed as

$$\frac{\sigma}{E} = \frac{c_1}{\sqrt{E}} \oplus cE^{-0.28}, \quad (35)$$

even if it has become customary to express the energy dependent term as a constant ( $c_2$ ).

Sampling fluctuations have a larger contribution to energy resolution for hadron showers than for em ones. In fact, the MeV-type

spallation protons which dominate hadronic shower signals may traverse a larger number of active layers with respect to the Compton and photo-electron which dominate em signals. For this reason, a smaller number of different hadronic shower particles contribute to the calorimeter signal, thus giving rise to larger fluctuations.

#### 1.6.6 The shape of the response function

As a result of the effects of the various types of fluctuations, the calorimeter response function may also acquire an asymmetric shape. This may happen, for example, if very few signal quanta constitute the signal, as in the case of quartz-fiber calorimeters (see Figure 31).

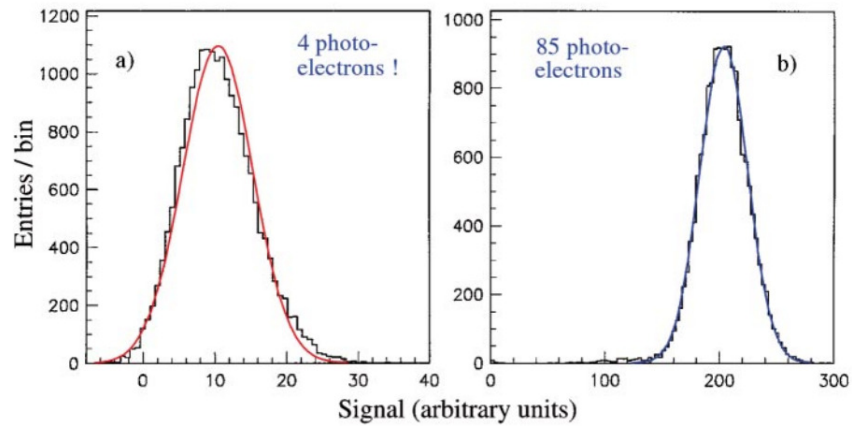


**Figure 31:** Signal distributions for 10 GeV (a) and 200 GeV (b) electrons showering in the CMS quartz-fiber calorimeter. The curves represent Gaussian fits to the experimental data. [21]

Shower leakage effects, such as particles escaping from the rear end of the detector may give rise to tails of the signal distributions, typically in the low-energy side.

It is also worth to mention the so called *leading particle effect*, which occurs in non-compensating hadron calorimeters and leads to asymmetric fluctuation in the  $f_{em}$ . If we consider a shower induced by pions, for example, the  $f_{em}$  value may be large even if in the first nuclear interaction most of the energy is transferred to a particle different from a  $\pi^0$ , since this particle may give rise then to energetic  $\pi^0$  in subsequent reactions. This effect is absent in proton-induced showers, since the leading particle has to be a baryon in this case. This can be seen in Figure 32.

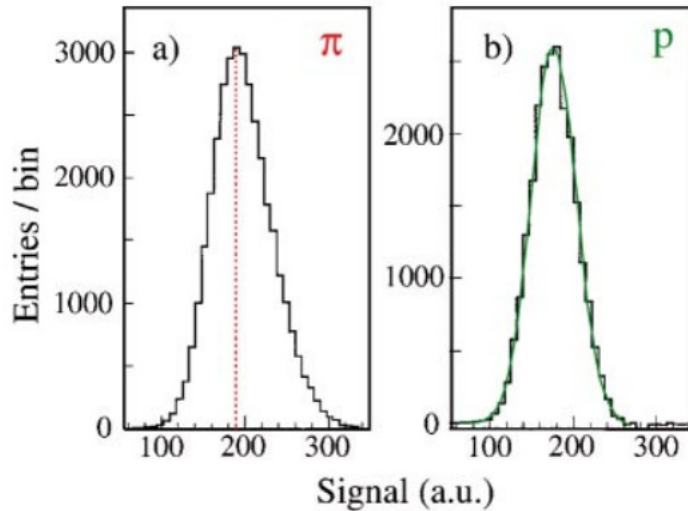


Figure 32: Signal distributions for 300 GeV pions and protons detected with a quartz-fiber calorimeter. The curve in (b) represents the result of a Gaussian fit to the proton distribution. [26]

## 1.7 SUMMARY

In this chapter the basic information about the detection of particles with calorimetry have been given, starting from the physics of detection mechanisms and shower development to the description of the characteristics of calorimeters. The latter ones, as it has been remarked more than once, exist in a wide variety of types. In the context of a particle physics experiment, the choice of the detector system and its parameters is influenced by various aspects besides the physics under study, such as the costs and the radiation levels.

The crucial point to consider in order to improve the energy resolution of a calorimeter is the identification of the type of fluctuations which dominate the detector performance. For example, in an instrument which relies on the detection of Cherenkov light, as a quartz-fiber detector, signal quantum fluctuations owed to the smallness of the light yield represent the main contribution to energy resolution. Therefore, in this case, it's useless to make efforts to increase the sampling frequency, in order to decrease the sampling fluctuations.

Nevertheless, the use of calorimeters for particle detection has to face some limitations, such as the impossibility of having high performances in detecting both em and hadronic showers with the same instrument. In fact, high values of em energy resolution result in high  $e/h$  values, thus implying low hadronic energy resolution. There are several projects which are currently involved in finding possible solutions to this problem, trying to find a compromise which allows to

have satisfying values of energy resolution both for the em and the hadronic part of the calorimeter. One of them, the DREAM Project, will be extensively described in the following sections.

# 2 | THE DREAM PROJECT

In the future developments of calorimetry, an aim to achieve will be that of improving the resolution in the detection of jets.

Concerning hadron colliders, there are many aspects which contribute to the efficiency in jet detection besides the energy resolution of the calorimeter, such as the jet algorithm and contributions of underlying events to the signals, but the latter two become less important with increasing energy and jets collimation.

In view of the realization of a future  $e^+e^-$  linear collider, one could aim for measuring the four-vectors of all elementary particles with a precision of  $\sim 1\%$ . The desired design for future calorimeters is the one which allows the distinction between hadronically decaying W and Z bosons. In order to obtain it, the constant  $c_1$  of the scaling term which appears in the customary formula that express the energy resolution of a calorimeter (see Section 1.6.5)

$$\frac{\sigma}{E} = \frac{c_1}{\sqrt{E}} \oplus c_2 \quad (36)$$

should be smaller than 0.3 (30%). Likewise, one may say that 80-90 GeV jets should be detected with a resolution of 3-3.5 GeV. Such a resolution could be obtained with sampling calorimeters. However, the downside of these devices is that the electromagnetic energy resolution is limited ( $\sim 15\%/\sqrt{E}$  [29]), because of the small sampling fraction necessary for compensation. Besides, the signals should be integrated over large volumes and time intervals to achieve a similar resolution, owing to the importance of the contribution of neutrons produced in the shower development to the signals.

## 2.1 NEW APPROACHES TO CALORIMETRY

Two methods aimed to overcome the limitations described in the previous section in view of future developments are now listed.

### 2.1.1 The energy flow method

This method combines the use of a precision tracker and a highly granular calorimeter. This allows the calorimeter to measure the energy of neutral particles and the tracker to precisely measure charged jet fragments.

However, the effectiveness of this method is limited by the fact that

one has to correct the calorimeter signals for the contributions of the charged jet particles, since the calorimeter can't distinguish between charged and neutral particles.

This method is being tested by the CALICE Collaboration [27].

### 2.1.2 Dual-readout calorimetry

This method allows to measure the em shower fraction  $f_{em}$  event-by-event, by means of the comparison of the amounts of Cherenkov and scintillation light produced by a hadron shower. In fact it is almost only the em shower component of hadronic showers which contribute to the production of the Cherenkov light, since electron and positrons which deposit the shower energy are relativistic down to  $\sim 0.2$  MeV (and thus emit Cherenkov photons). On the other hand, spallation protons that dominate the non-em calorimeter signals are typically non-relativistic (hence they don't produce Cherenkov light), but, being charged, in some types of active media, such as scintillators, these protons generate signals. Therefore, in a calorimeter equipped with active materials suitable to detect both scintillation and Cherenkov light, the former is produced by the total energy deposited by all the charged shower particles, while the latter is given by  $e^-$  and  $e^+$  only. By separately measuring the Cherenkov and the scintillation signals it is possible to deduce the value of the em shower fraction, by means of a simple relation which will be described in Section 2.2.1.2.

In the next sections the DREAM project, the result of an international collaboration, aimed to exploit the potential of dual-readout calorimetry, will be briefly described from its beginning to the most recent results.

## 2.2 THE DUAL-READOUT METHOD

### 2.2.1 The DREAM detector

The first instrument based on the dual-readout approach dates back to more than a decade ago and was a  $1.4 \lambda_{int}$  deep calorimeter, devoted to the measurement of high-energy cosmic hadrons [12]. Because of its successful results, the idea of a longitudinally fully containing ( $10 \lambda_{int}$  deep) dual-readout calorimeter was pursued and the DREAM (Dual-READout Method) detector was built and tested.

The basic element of this detector is an extruded copper rod, 2 m long and  $4 \times 4$  mm<sup>2</sup> in cross-section. The rod is hollow and the central cylinder has a diameter of 2.5 mm. Seven optical fibers, each with a diameter of 0.8 mm and a length of 2.50 m, are inserted in this hole, three of which are plastic scintillating fibers, while the other four are

intended for detecting Cherenkov light. The fiber pattern of single rods can be seen in Figure 33(a). Concerning the Cherenkov fibers, those devoted to the central region of the detector are made of high-purity quartz, while those devoted to the peripheral regions are made of acrylic plastics.

5580 of the previously described rods constituted the DREAM calorimeter, of which 5130 were filled with fibers, while the remaining empty rods were used on the periphery of the detector. The fibers were grouped to form 19 towers, each having an approximately hexagonal shape and consisting of 270 rods, as it is showed in Figure 33(b).

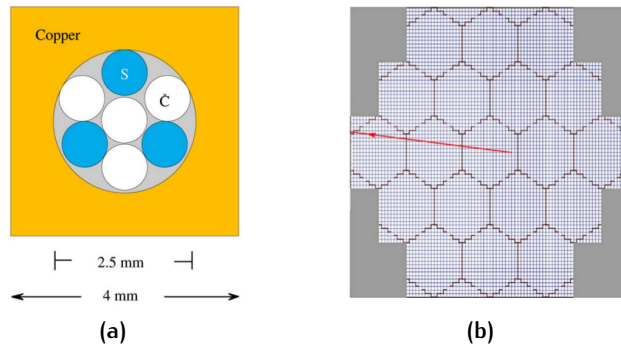


**Figure 33:** (a) The basic building block of the DREAM calorimeter is a  $4 \times 4$  mm<sup>2</sup> extruded hollow copper rod of 2 meters length, with a 2.5 mm diameter central hole. Seven optical fibers (four Cherenkov and three scintillating fibers) with a diameter of 0.8 mm each are inserted in this hole, as shown. (b) Layout of the DREAM calorimeter. The detector consists of 19 hexagonal towers. A central tower is surrounded by two hexagonal rings, the Inner Ring (6 towers) and the Outer Ring (12 towers). The towers are not longitudinally segmented. The arrow indicates the (projection of the) trajectory of a muon traversing the calorimeter oriented in the position  $\phi=6^\circ$ ,  $\theta=0.7^\circ$ . [13]

The sampling fraction of the copper/scintillating-fiber structure for mips was 2.1%. The depth of the tower structure corresponded to 99 radiation lengths ( $X_0$ ) and 10 nuclear interaction lengths ( $\lambda_{int}$ ). Fibers departing from the rear of the calorimeter were bunched separately (Figure 34), such as there were one bunch of scintillating fibers and one of Cherenkov fibers for each tower. Each bunch was then coupled with a PMT. A yellow filter was installed between the scintillation fiber ends and the photocathode, in order to remove the blue part of the spectrum of light generated in the scintillating fibers, which is attenuated by self-absorption.

The DREAM calorimeter has been tested at the H4 beamline of the SPS at CERN. It was mounted on a platform which could move vertically and sideways with respect to the beam, so that it was possible to change the angle of incidence of the beam particles with respect to

the fibers in the horizontal plane ( $\phi$ ) and in the vertical plane ( $\theta$ ) by means of a crane.



**Figure 34:** Fiber bunches exiting from the rear face of the DREAM calorimeter. Each bunch was tightly squeezed by means of a thin metal collar with adjustable radius. [13]

#### 2.2.1.1 *Electron detection*

Even if the DREAM calorimeter was designed for the detection of hadrons and jets, its electromagnetic performance was firstly tested with electron beams [14].

The linearity of the signal is studied through the calorimeter response (the average signal per unit of deposited energy).

In Figure 35 the response of the DREAM calorimeter, for scintillation and Cherenkov signals, to electrons in the range 8-200 GeV is shown. As it can be seen, scintillation signals present a strong non-linearity: in fact, while deviations from linearity in the Cherenkov case are smaller than 2% over the entire energy range, in the scintillation case the response at 8 GeV is  $\sim 12\%$  smaller than that at 200 GeV.

It was established that the non-linearity originated in the central tower, where 90% of the signal is contained. The DREAM Collaboration focused then on the strange fact that non-linearity was more evident at low energies, in contrast with the typical non-linearity at high energies, owed to saturation effects in the light detectors or to shower leakage. Three effects, which are listed in the following, were considered responsible of such behaviour.

- Light attenuation in the fibers, owed to self-absorption caused by the overlapping absorption and emission spectra of the wavelength shifting dopants in the scintillating fibers. Since light produced by high-energy showers is emitted deeper inside the detector with respect to the light produced by low-energy show-

ers, the latter results to be much more attenuated and the resulting response is smaller. This type of non-linearity is negligible for the Cherenkov signals, since the light attenuation in the region where em showers develop is virtually absent.

- Energy loss in upstream material, like the preshower detector ( $1 X_0$  of lead) placed before the calorimeter but also the first radiation length of the copper absorber. The fraction of energy deposited in this dead material is larger if the electron energy is lower and this effect is negligible for the Cherenkov signals, since the latter ones have almost no contributions from the energy deposited in the first few radiation lengths.
- Inefficiencies in the sampling of the early, highly collimated shower component, owed to the very small angles between the shower axes and the fibers. This effect is much stronger in the scintillation case, since for the Cherenkov signals their lateral shower profiles in the early stage of the shower development are not as steep as for the scintillation signals.

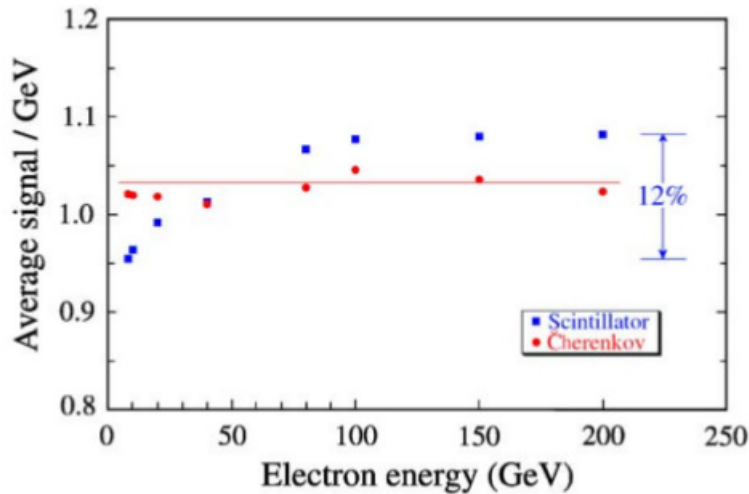


Figure 35: The response for electrons entering the DREAM calorimeter oriented in the tilted position ( $\phi=3^\circ$ ,  $\theta=2^\circ$ ), as a function of energy. Results for the scintillating fibers (squares) and the Cherenkov fibers (circles) are shown separately. The data are normalized to the response for 40 GeV electrons, obtained in the calibration runs. [14]

The above-mentioned effects have also influence on the electromagnetic energy resolution of the DREAM calorimeter. This influence manifests as a deviation from the  $E^{-1/2}$  scaling given by the Poisson statistics, as it was said in Section 1.6. The latter governs both the sampling fluctuations, which dominate the em energy resolution of sam-

pling calorimeters, and those in the photoelectron statistics, which are more significant in the case of the Cherenkov signal. The deviation from the  $E^{-1/2}$  scaling can be seen in Figure 36, which shows the em energy resolutions for the two readout media, for the calorimeter placed in the position  $\phi=3^\circ$ ,  $\theta=2^\circ$ , in order to avoid channelling effects. From the figure one can see that the above-mentioned deviation is smaller for the signals measured with the Cherenkov fibers. One may also notice that the  $E^{-1/2}$  term is larger for the Cherenkov readout than for the scintillation one.

Concerning the contribution of the sampling fluctuations and the photoelectron statistic to the  $E^{-1/2}$  term, fluctuations in the number of photoelectrons dominate the Cherenkov resolution in quartz, while for the scintillator signals the two contribution are almost equal.

Finally, it is worth to mention the fact that two types of Cherenkov fibers were tested with this detector: quartz fibers were used in the inner part of the calorimeter, while in the twelve calorimeter towers constituting the outer ring plastic fibers were chosen. The latter ones resulted to have a better energy resolution with respect to the quartz ones. It was then found that the Cherenkov light yield for plastic fibers amounted to 18 photoelectrons/GeV (p.e./GeV), to be compared with the 8 p.e/GeV for quartz.

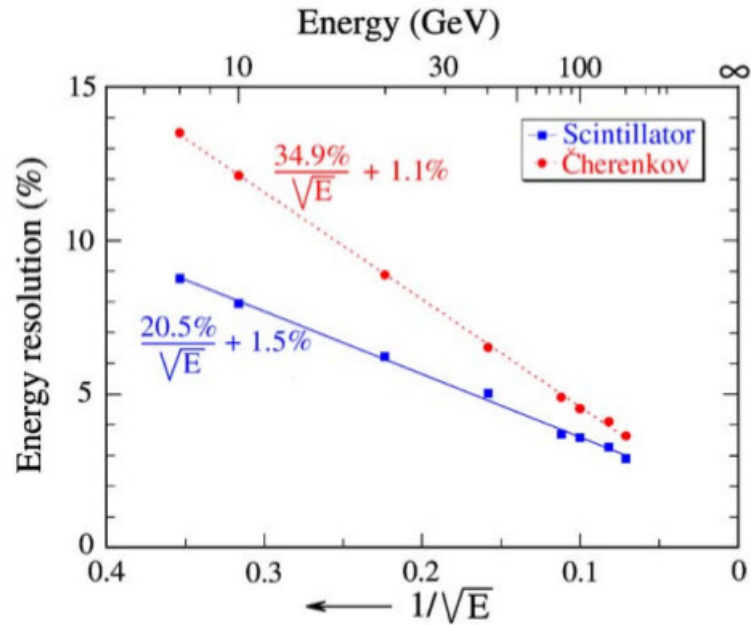


Figure 36: The energy resolution as a function of energy, measured with the scintillating (squares) and the Cherenkov fibers (circles), for electrons entering the calorimeter in the tilted position ( $\phi=3^\circ$ ,  $\theta=2^\circ$ ). [14]

### 2.2.1.2 Hadron and jet detection

The DREAM detector was also tested with negative pions, with energies in a range from 20 to 300 GeV, and with simulated jet events, obtained from the pion beam by selecting hadron interactions in a polyethylene target installed upstream of the DREAM calorimeter [15].

The signal distributions for 100 GeV  $\pi^-$  are shown in Figure 37, as measured with the scintillating and Cherenkov fibers (37a and 37b respectively). It can be seen that these distributions present the typical features of non-compensating calorimeters, that is they are broad and asymmetric, and have mean values which are remarkably smaller than those for electrons of the same energy.

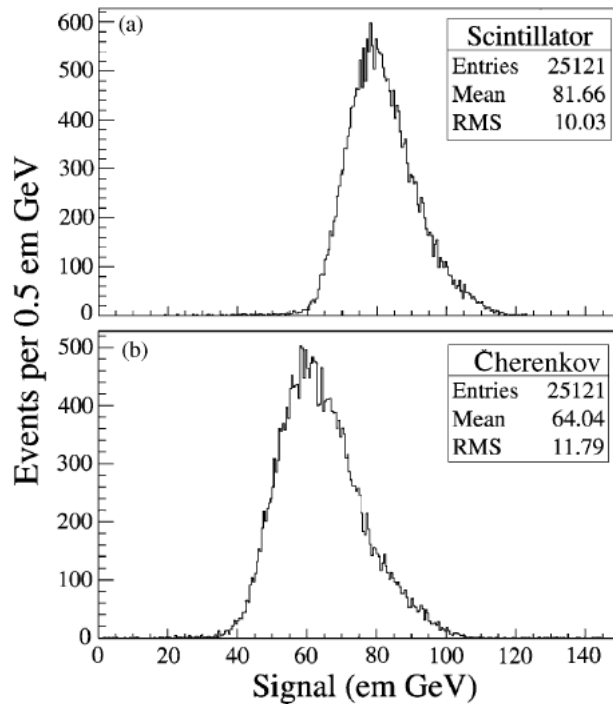


Figure 37: Signal distributions for 100 GeV  $\pi^-$  recorded by the scintillating (a) and Cherenkov (b) fibers of the DREAM calorimeter, oriented in the untilted position ( $\phi=2^\circ$ ,  $\theta=0.7^\circ$ ). [15]

The energy resolution for pions as a function of energy is shown in Figure 41a and it is described by the linear sum of a  $E^{-1/2}$  term and a constant term.

Both the energy resolution and the linearity of the calorimeter response underwent a considerable improvement after that the dual-readout approach was applied, as it will be described in the following.

One may express the hadronic calorimeter response as a function of the em shower fraction  $f_{em}$  in this way:

$$R(f_{em}) = f_{em} + \frac{1}{e/h}(1 - f_{em}) \quad (37)$$

The previous relation is valid both for Cherenkov and scintillation signals and  $R=1$  for electromagnetic showers. The  $e/h$  values are very different for the two sampling media, thus explaining the differences between the Cherenkov and scintillator characteristics of the calorimeter.

Denoting with  $Q$  the Cherenkov signal and with  $S$  the scintillation one, the  $Q/S$  signal ratio is a variable directly related to  $f_{em}$  and, considering that  $(e/h)^{-1}=0.20$  [21] and  $0.71$  [30] for the Cherenkov and scintillation readout respectively, it can be written as

$$\frac{Q}{S} = \frac{f_{em} + 0.20(1 - f_{em})}{f_{em} + 0.71(1 - f_{em})} \quad (38)$$

Figure 38 shows the scatter plot of the Cherenkov signal versus the scintillator one for  $100 \text{ GeV } \pi^-$ .

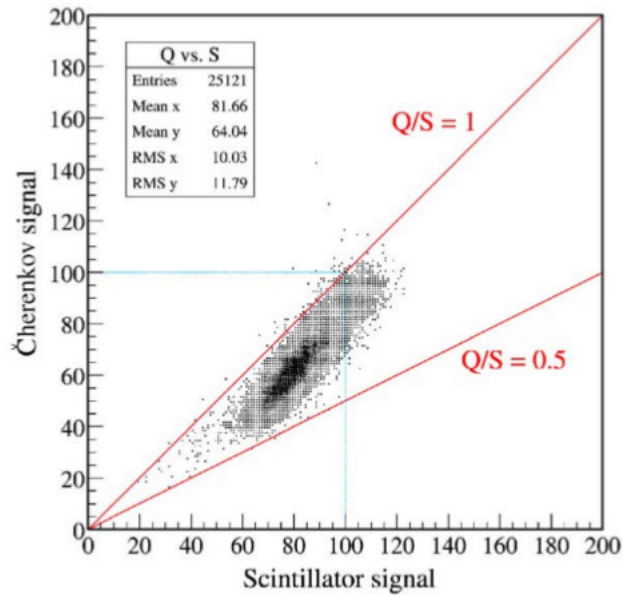


Figure 38: Cherenkov signals versus scintillator signals for  $100 \text{ GeV } \pi^-$ . [15]

**THE Q/S METHOD** From the  $Q/S$  ratio (see Equation 38) one may therefore obtain the value of  $f_{em}$  event-by-event and correct the measured signals. In order to obtain such corrections, the measured scintillator signals were firstly corrected for the effects of lateral shower leakage [15] (no leakage corrections were applied to the Cherenkov

signals, since the Cherenkov profiles are narrower than the scintillator ones). The leakage-corrected Q/S value was then converted into the  $f_{em}$  value, using Equation 38. Finally, corrections for the effect of non-compensation were applied to the leakage-corrected scintillator signals, by increasing them such as to make the response, given in Equation 37, equal to that for em showers:  $R=1$ .

The information on  $f_{em}$  can be equally used to correct the Cherenkov signals for the effects of non-compensation. In this case the improvements resulting from the Q/S method are much larger than for the scintillation channel, since the Cherenkov calorimeter has a much larger  $e/h$  value.

After the Q/S corrections, a much more symmetric and narrow signal distribution is obtained, as well as a considerable improvement in the energy resolution and an average value of the distribution much closer to the real one. This can be seen in Figure 39, which shows the comparison between the Cherenkov signal distribution for 100 GeV  $\pi^-$  and distributions for subsamples of events selected on the basis of the measured  $f_{em}$  value and in Figure 40, which shows the same for jet simulated events.

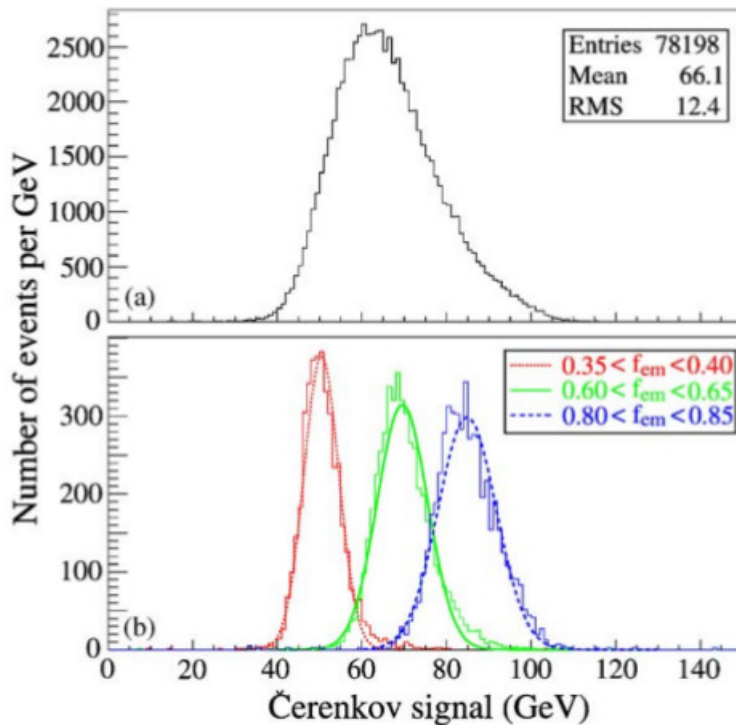


Figure 39: Cherenkov signal distribution for 100 GeV  $\pi^-$  (a) and distributions for subsamples of events selected on the basis of the measured  $f_{em}$  value, using the Q/S method (b). [15]

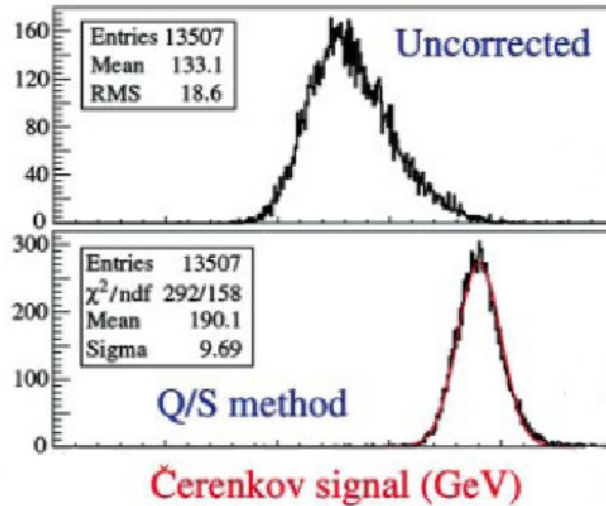


Figure 40: Signal distributions for high-multiplicity "jets" in DREAM before and after corrections on the basis of the observed Q/S ratio were applied. [5]

Figure 41a shows the energy resolution for single pions and jets, before and after the corrections applied by means of the Q/S method. From the figure one may observe the benefit of the Q/S method, especially in the case of jets.

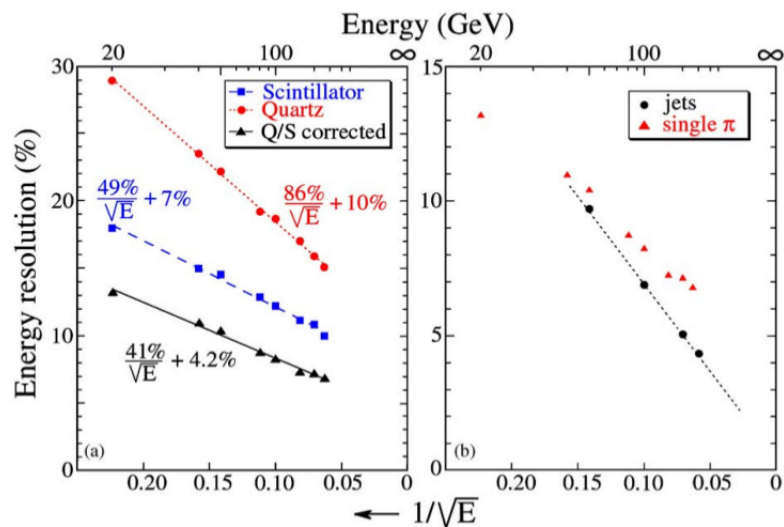
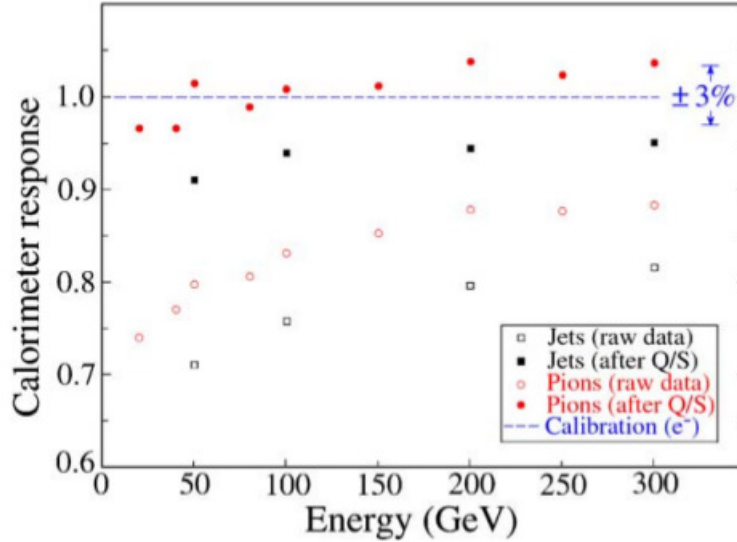


Figure 41: The energy resolution for single pions as a function of energy, before and after corrections made on the basis of the measured Q/S signal ratio (a). Comparison of the corrected resolutions for jets and single pions (b). [15]

Finally, observing Figure 42 (which concerns scintillation light) one may notice how the linearity improved, both for pion and "jets" sig-

nals, after the Q/S corrections. A strong non linearity for pion detection, with deviations of  $\sim 20\%$ , characterized in fact the calorimeter response before the corrections were applied, as it can be seen in the figure.



**Figure 42:** The calorimeter response to single pions and high-multiplicity jets, before and after corrections made on the basis of the measured Q/S signal ratio. [15]

### 2.2.1.3 Measurement of the contribution of neutrons to hadron signals

As it has been said in Section 1.5.4, measuring the total kinetic energy carried by neutrons produced in the shower development can be an useful way to reduce the effects of visible energy fluctuations. The latter ones become dominant in hadronic calorimeters, once that the fluctuations in the em shower fraction have been eliminated, as it was seen in the previous section, and the calorimeter structure is large enough to contain all the shower particles.

The measurement of the contribution of shower neutrons to hadron signals event-by-event has been performed with the DREAM calorimeter [28] and is one of the aim of the DREAM Project.

As it can be seen from the average time structure of Cherenkov and scintillation signals, shown in Figure 43, a tail with a characteristic time constant ( $\sim 20$  ns) in the scintillating time structure is the manifestation of the neutron contribution, as it was already seen in Figure 23 for the SPACAL calorimeter with another time constant, because the material was different. In fact, since one may assume that the plastic fibers are made of an approximately equal number of hydrogen and carbon atoms, neutrons most likely lose their energy by means of elastic scattering with protons. The physical meaning of the

time constant is thus the time which elapses between two subsequent neutron-proton scatterings in this material combination. As a proof of that, the tail is absent in scintillator signals generated by em showers. Moreover, since the recoil protons are non relativistic, they don't generate Cherenkov light and this tail is absent in the Cherenkov signals.

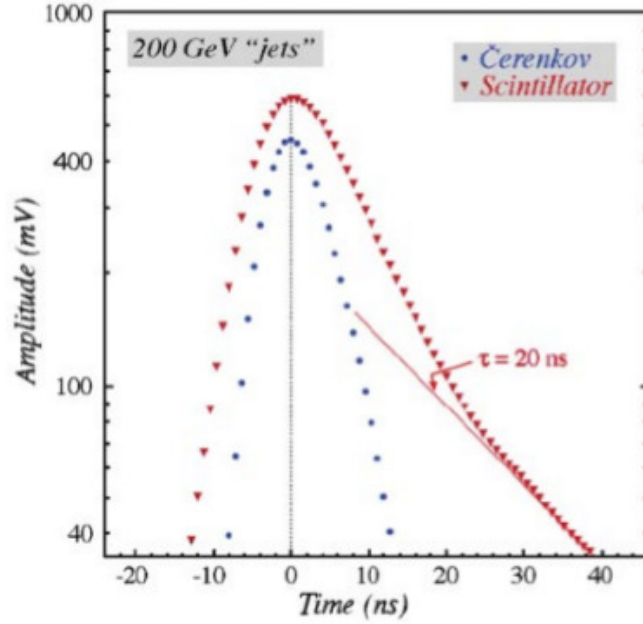
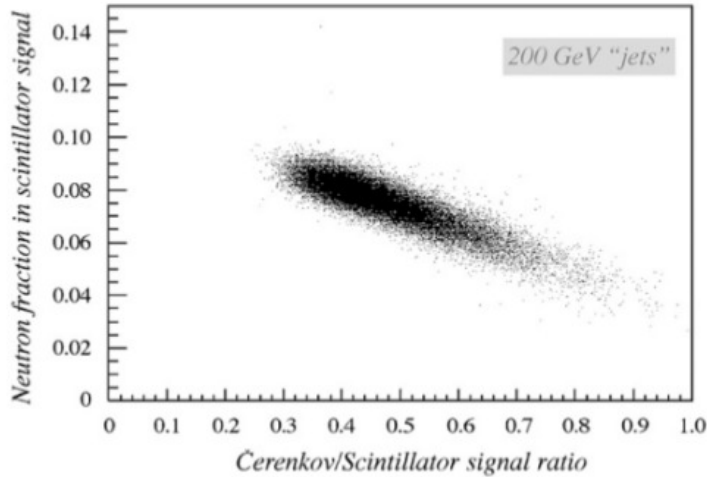


Figure 43: Average time structure of the Cherenkov and scintillation signals recorded for 200 GeV "jets" developing in the DREAM calorimeter. [28]

Figure 44 shows the neutron fraction in scintillator signals, *i.e.* the relative contribution of the tail measured in the time structure to the scintillation signals event-by-event, as a function of the Q/S signal ratio. It can be seen that the two quantities result to be anti-correlated, as expected. In fact, since the Cherenkov signal is insensitive to neutron contribution, one expects that increasing the Q/S ratio, which is related to  $f_{em}$ , the neutron fraction decreases. Therefore one can deduce that the tail actually represents the neutrons present in the shower.

Because of the correlation between the total amount of invisible energy and the total kinetic energy carried by neutrons produced in the hadronic shower development, this can be exploited in order to obtain an improvement of the calorimeter performance and to get close to the hadronic energy resolution limit of  $15\%/\sqrt{E}$ , as it was said in Section 1.6.5.



**Figure 44:** Scatter plot for 200 GeV "jets": for each event, the combination of the total Cherenkov/scintillation signal ratio and the fractional contribution of the neutrons to the total scintillation signal is represented by a dot. [28]

### 2.2.2 Dual-readout with crystals

The possibility of using crystals for dual-readout purposes has also been explored by the DREAM Collaboration. The dual-readout approach was originally demonstrated with the first DREAM copper/-fiber module, as it has been described in the previous paragraph. However, the main limitation of this detector is represented by the low Cherenkov photoelectron production, arising from the very small sampling fraction and leading to limited electromagnetic performances. The Cherenkov light yield amounted to 8 p.e/GeV for the quartz fibers and contributed with  $35\%/\sqrt{E}$  to the measured resolution.

Exploiting the dual readout method with homogeneous materials may thus be a way to increase the number of Cherenkov photoelectrons, since in this case all the material is active for particle detection, and to improve the performance on em showers, because of the absence of sampling fluctuations.

The main advantage of some dense high-Z crystals, such as lead tungstate ( $\text{PbWO}_4$ ) and bismuth germanate (BGO), is that the particles passing through them produce a considerable amount of Cherenkov light. In order to apply the dual-readout method, and thus separating Cherenkov from scintillation light, the differences between the two types of signals are exploited. In fact, differently from the case of the fiber calorimeter, where the two different signals were read out by separate PMTs, here the signal exiting from the PMT coupled with the crystal is a mixture of Cherenkov and scintillation lights. The dif-

**Table 2:** Different properties of Cherenkov and scintillation light. [5]

	Cherenkov	Scintillation
<i>Time structure</i>	Prompt	Exponential decay
<i>Light spectrum</i>	$1/\lambda^2$	Characteristic peaks
<i>Directionality</i>	$\cos\theta_C = 1/\beta n$	Isotropic
<i>Polarization</i>	Yes	No

ferent characteristics between Cherenkov and scintillation light are listed in the following and are summarized in Table 2.

- *Directionality.* Scintillation light (S) is emitted isotropically, while Cherenkov light (C) is emitted at a precise angle (we call it the "Cherenkov angle") by the relativistic shower particles in the detector volume. C and S can then be separated looking at the directionality of the light (see Figure 46).
- *Time structure.* Scintillation light is produced through a mechanism which is characterized by one or more time constants, thus determining the pulse shape, while Cherenkov light is prompt. The two types of light can then be separated recording the pulse shape and then integrating it in different time structures (see Figure 51).
- *Spectral properties.* Scintillation light spectrum varies from crystal to crystal, while Cherenkov light exhibits a characteristic  $\lambda^{-2}$  spectrum. C and S can then be separated using optical filters (see Figure 48).
- *Polarization.* Cherenkov light is polarized, while scintillation light is not, hence Cherenkov and scintillation signals can be separated by means of polarization filters.

A "perfect" crystal to be used in dual-readout calorimetry, *i.e.* a crystal which allows to obtain a good separation between the Cherenkov and scintillation components, should therefore have a scintillation spectrum which peaks far from the bulk of Cherenkov radiation and a scintillation decay time of tenths of nanoseconds.

The DREAM Collaboration tested different homogeneous media for dual-readout, that is pure  $\text{PbWO}_4$  or doped (with Mo and Pr), BGO and BSO crystals. The tests have been performed at the H4 and H8 beam lines of the SPS with electron beams of different energies, using a common setup for all the single-crystals measurements.

The experimental setup is shown in Figure 45. Two PMTs were positioned at the opposite ends of the crystal, in order to read out the light produced by traversing particles. A platform able to rotate around a vertical axis hosted the studied crystal. The latter was oriented in the horizontal plane and the rotation axis went through its

geometrical center, as well as the steering direction of the particle beam.

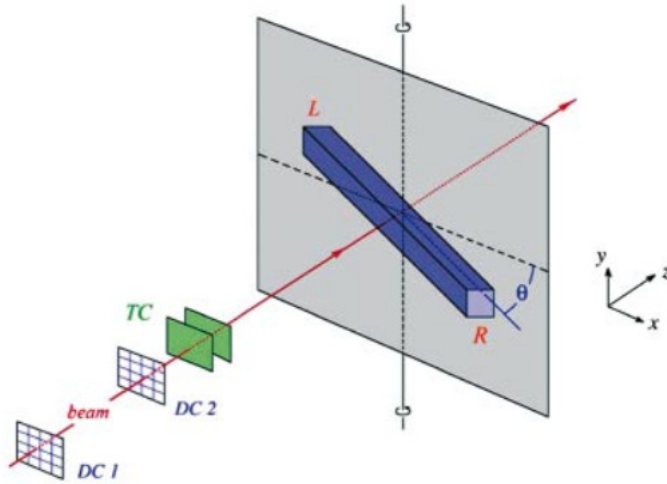


**Figure 45:** Experimental setup in which the beam tests of the crystals were performed. The angle  $\theta$  is negative when the crystal is oriented as drawn here. The crystal orientation shown in this figure corresponds to  $\theta = -30^\circ$ . [16]

#### 2.2.2.1 $PbWO_4$ crystals

The average time structure of the signals from 50 GeV electrons in the  $PbWO_4$  crystal, for angles  $\theta=30^\circ$  and  $-30^\circ$  respectively is shown in Figure 46 [17]. As it can be seen, the trailing edges of the two signals are identical (in fact they are dominated by the slow scintillation component that is present at each angle), but there is a difference between the leading edges and the amplitude of the signals if taken at the Cherenkov or at the anti-Cherenkov angle <sup>1</sup>. In fact, signals recorded at the Cherenkov angle have a significantly steeper leading edge and larger amplitude, since they are dominated by the prompt Cherenkov light. This behaviour is naturally reversed for the PMT on the opposite side.

If one indicates with R and L the average signals measured in the two PMTs, respectively, for the same events, the response asymmetry, defined as the ratio  $(R-L)/(R+L)$  represents a useful figure of merit. If this value results to be different from zero, it means that a non-isotropic signal component is present, *i.e.* Cherenkov light. This is illustrated in Figure 47, where the left-right response asymmetry is

<sup>1</sup> The angle at which the Cherenkov light has a maximum in one of the two PMTs ( $\theta = 30^\circ$  for the Right PMT and  $\theta = -30^\circ$  for the Left PMT) was called "Cherenkov angle", while the opposite angle, *i.e.* the angle at which a given PMT collects only scintillation light, but not Cherenkov, was called "anti-Cherenkov angle".

plotted as a function of the rotation angle of the  $\text{PbWO}_4$  crystal. The left-right response asymmetry was measured in two different configurations of the crystal, in order to study the early and late components of the showers. Besides the normal configuration, represented by circles in the Figure, the so-called "late" configuration, represented by triangles, has been considered. The latter was obtained by positioning a block of lead in front of the crystal, so that beam particles started showering in it. As it can be seen from the figure, in the second case the effect of the asymmetry is highly reduced, owing to the fact that the light is produced in the crystal by particles constituting the late part of the shower, where their directions are almost isotropic.

Testing the pure  $\text{PbWO}_4$  crystal was useful in order to demonstrate the possibility of separating Cherenkov and scintillation light exploiting their different directionality. Nevertheless, a similar approach can't be used in a  $4\pi$  detector. Therefore the DREAM Collaboration decided to study doped  $\text{PbWO}_4$  crystals, where the doping elements have the function of shifting the scintillation spectrum to longer wavelengths. In this way the difference between the time structures of the two signals may be exploited in order to separate the two types of light.

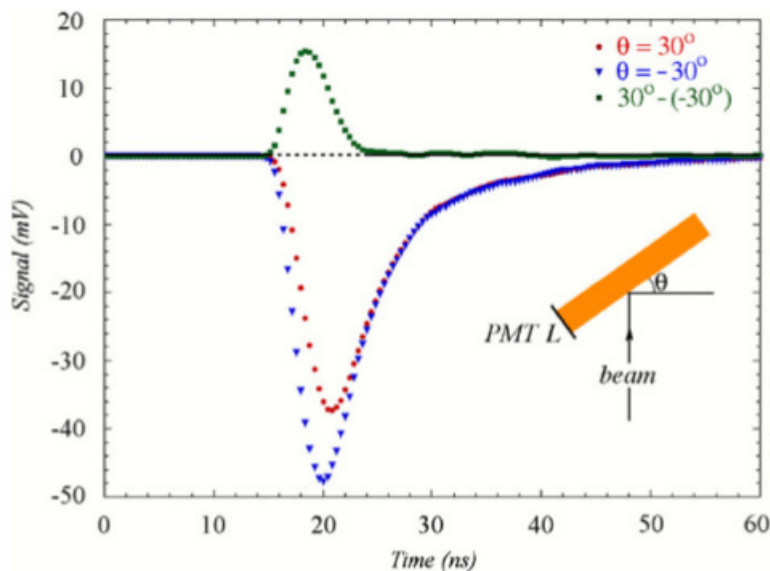


**Figure 46:** Time structures of the PMT signal from 50 GeV electrons traversing a  $\text{PbWO}_4$  crystal at angles  $\theta=30^\circ$  and  $-30^\circ$ , respectively, and the difference between these two time distributions. [17]

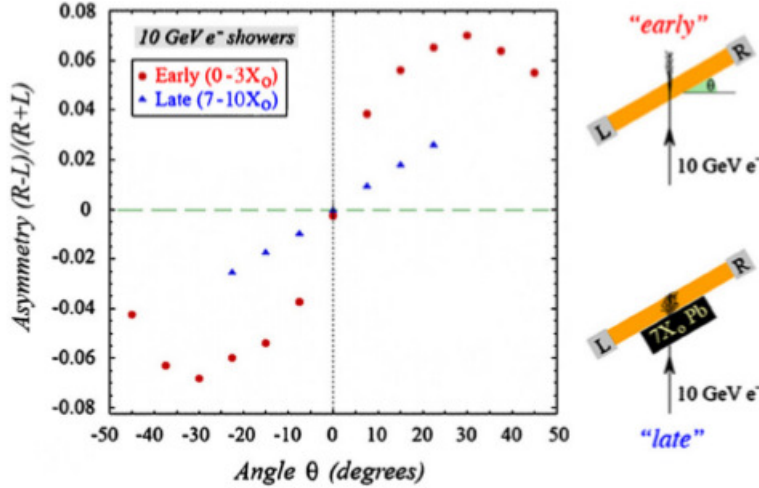


Figure 47: Left-right response asymmetry measured for 10 GeV electrons showering in a  $2.5 X_0$  thick  $\text{PbWO}_4$  crystal, as a function of the orientation of the crystal (the angle  $\theta$ ). Results are shown for the early and late components of the showers. The latter measurements were obtained by placing 4 cm of lead upstream of the crystal. [17]

#### 2.2.2.2 Doped $\text{PbWO}_4$ crystals

The DREAM Collaboration also performed a study of different doping elements, to be added to the  $\text{PbWO}_4$  crystal, in order to achieve a shift of the scintillation spectrum to longer wavelengths and a longer decay time.

Molybdenum was chosen in the end, and  $\text{PbWO}_4$  crystals with different dopant levels (from 0.1% to 5%) were tested. The doping with Mo allowed to obtain a shift of the scintillation peak from  $\sim 420$  nm to  $\sim 500$  nm, thus allowing the use of filters to separate the bulk of the Cherenkov light, peaking at a shorter wavelength.

The quantities under study were the time structure of the signals, the C/S ratio, the effect of light attenuation and the Cherenkov light yield [18].

The use of optical filter permitted to detect separately scintillation and Cherenkov light. A short-pass UV filter was used to select the wavelength region that contributed to the Cherenkov signal, while a long-pass yellow filter was used for scintillation. Each filter was placed between one side of the crystal and the correspondent PMT.

**TIME STRUCTURE** The two different time structures measured on both ends of the crystal are shown in Figure 48. The peculiar characteristics of the two types of light, previously listed in Table 2, can be

appreciated in the figure. Comparing the time structures of the signals showed in Figure 48 with those showed in Figure 46, concerning the readout of the undoped  $\text{PbWO}_4$  crystal without the use of filters, one may notice a considerable improvement of the level of separation of Cherenkov and scintillation lights.

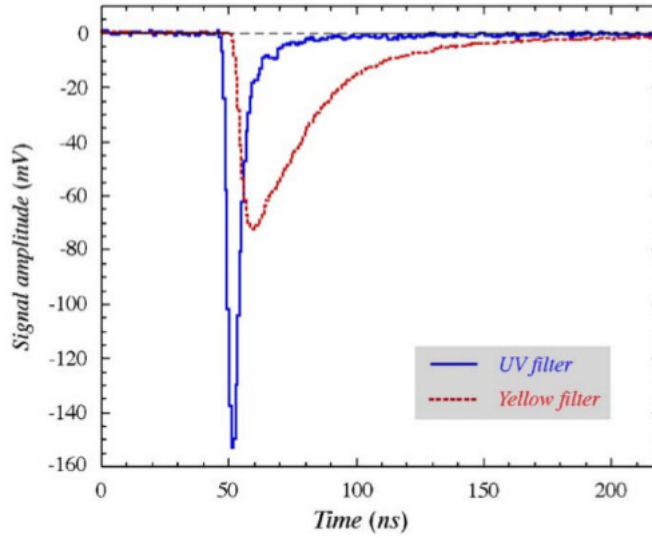


**Figure 48:** Average time structure of the signals from a  $\text{PbWO}_4$  crystal doped with 1% of molybdenum, generated by 50 GeV electrons. The angle  $\theta$  was  $30^\circ$  in these measurements. The results obtained with UV and yellow filters are shown. [18]

**C/S RATIO** One expects the amount of light traversing the UV filter to be strongly dependent from the angle of incidence of the beam particles on the crystal (which is rotated), since it should predominantly be of the Cherenkov type. Figure 49, which shows the ratio of the signals read at the two ends of the crystal as a function of the angle of incidence, confirms the expectations. In fact, since the Cherenkov angle amounted to  $\sim 63^\circ$  in this case, one can see a maximum of the C/S ratio at  $\theta = 90 - \theta_C \sim 27^\circ$ , as expected.

**LIGHT ATTENUATION** The attenuation length was measured for the two components of the signal. This showed how, for signals detected on the UV filter side,  $\lambda_{att}$  ranged from 10 to 20 cm, depending on the filters used and on the concentration of dopant. The scintillation signals, on the other end, resulted almost independent from the impact point.

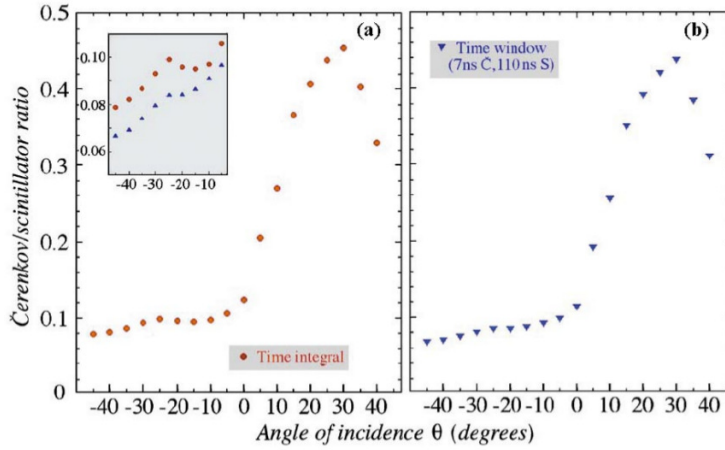


**Figure 49:** Ratio of the signals from the light transmitted by the UV and the yellow filters, as a function of the angle of incidence of the beam particles. The signals were obtained either by integrating over the full time structure (a), or over limited time interval chosen such as to purify their Cherenkov or scintillation content (b). [18]

**CHERENKOV LIGHT YIELD** The Cherenkov light yield was found to be dependent from the molybdenum concentration and the UV filter. In particular, it was found to range from 7.7 p.e./GeV to 60 p.e./GeV, increasing with wider transmission window for the UV filter and with lower Mo concentration.

### 2.2.2.3 BGO crystals

The use of BGO crystals in dual-readout calorimetry ([17], [19]) offers the opportunity of shifting the scintillation spectrum peak to 480 nm and having a decay time of  $\sim 300$  ns. Even if the Cherenkov component in the signals from this crystal is much smaller than for  $\text{PbWO}_4$ , the use of BGO offers the possibility of measuring its contribution with high precision (owing to the large decay time of the scintillation component) and the spectral differences between the two components.

Figure 50 shows the time structure of the signals, obtained again with UV and yellow filters, as described in the previous section. As it can be seen, the UV filter signal presents a sharp peak, representing the Cherenkov component and a long tail with the characteristic time structure of pure scintillation light. The relative contributions of Cherenkov and scintillation photons to the UV filter signal could be deduced by integrating over the proper time intervals and are shown in Figure 51. The C/S ratio could therefore be measured with an accuracy of  $\sim 20\text{-}30\%$  for an energy deposit of 1 GeV.

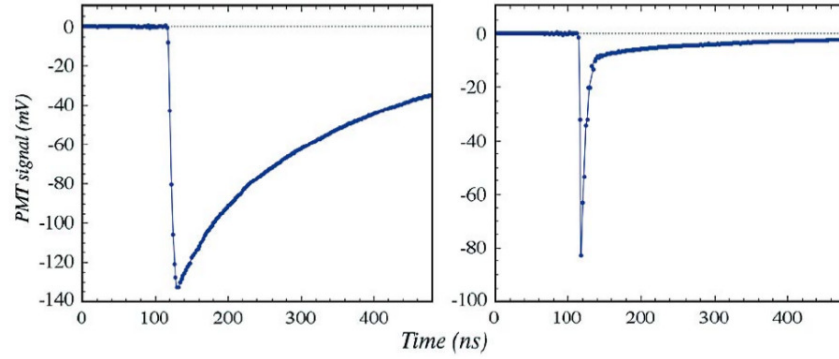


**Figure 50:** The time structure of a typical 50 GeV electron signal measured in the BGO crystal equipped with a yellow filter (a), and with an UV filter (b). These signals were measured with sampling oscilloscope, with a time resolution of 2.0 ns. The crystal was oriented perpendicular to the beam line ( $\theta = 0$ ). [17]

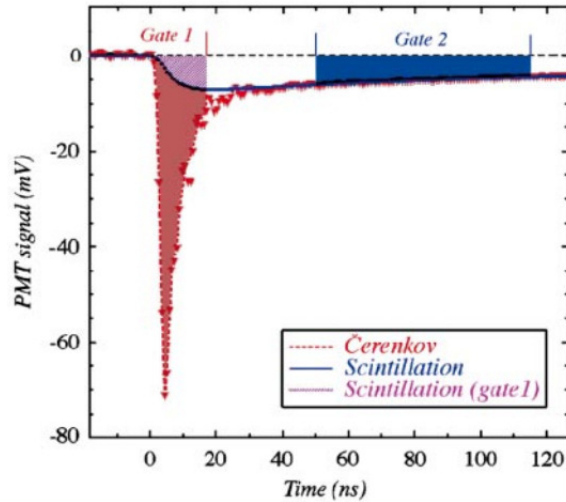


**Figure 51:** The UV BGO signals were used to measure the relative contributions of scintillation light (gate 2) and Cherenkov light (gate 1). The oscilloscope sampled the time structure at intervals of 0.8 ns in this case. [19]

#### 2.2.2.4 BSO crystals

The study performed on BGO crystals emphasized the possibility of separating the two types of light by exploiting the large differences between their spectral properties and time structure of the two components. For this reason, BSO (bismuth sylicate) crystals have been subject to the attention of the DREAM Collaboration [31]. BSO ( $\text{Bi}_4\text{Si}_3\text{O}_{12}$ ) has the same crystal structure as BGO, with silicon atoms replacing the germanium ones.

The properties of BSO crystals in dual-readout calorimetry resulted to be similar to those of BGO, with some interesting advantages, *e.g.* an higher Cherenkov light yield and a smaller level of contamination of scintillation light in Cherenkov signals.

#### 2.2.2.5 Combined calorimetry

An hybrid dual-readout calorimeter, consisting in an electromagnetic section made of 100 BGO crystals and the hadronic DREAM copper/fibers prototype was also tested by the DREAM Collaboration [19]. With such an hybrid calorimeter, Equation 38, used in the case of the DREAM fiber prototype alone in order to get the  $f_{em}$  from the ratio of Cherenkov and scintillation signal, can't be applied, since the  $e/h$  values of the BGO crystals are different from those of the fiber detector. Moreover, the energy sharing between the two calorimeter sections varied from event to event.

Anyway, as it can be seen in Figure 52, the C/S ratio itself represents a good measure of the em shower fraction. The Cherenkov signal distribution is shown, before and after the selection of three subsets of events, on the basis of the measured C/S ratio. As in the case of the fiber prototype alone, one can see how the distributions become narrower, more Gaussian and the mean values have a proportional increase with the C/S value of the selected events.

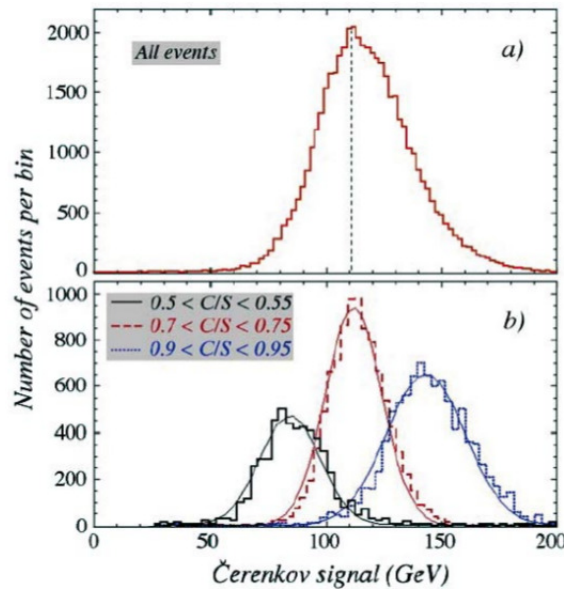
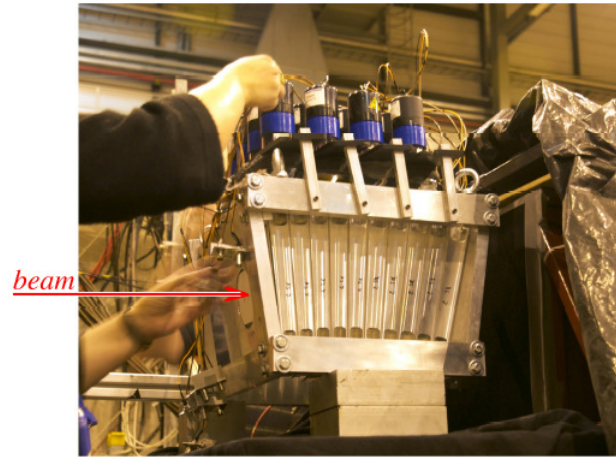


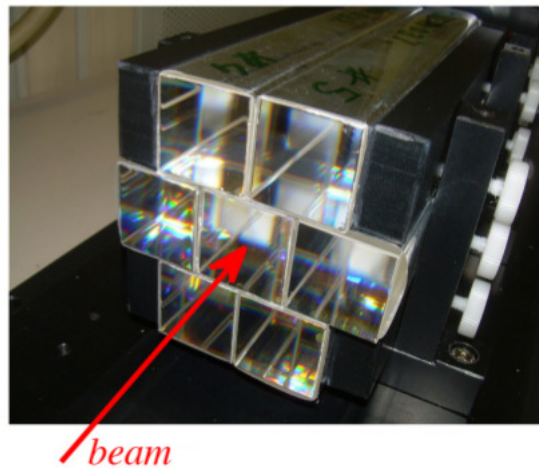
Figure 52: The Cherenkov signal distribution for 200 GeV jet events detected in the BGO/fiber calorimeter system (a) together with the distributions for subsets of events selected on the basis of the C/S ratio (b). [19]

### 2.2.2.6 Crystal matrices

More recently, two crystal matrices, which are shown in Figure 53, have been tested at the H8 beam line of CERN SPS with electron beams of energies ranging from 4 to 180 GeV.



(a)



(b)

**Figure 53:** (a) The BGO matrix, consisting of 100 tapered crystals. They were read out from the top by 16 PMTs, each of which was equipped with a UV filter, while the beam entered from the side, as shown. (b) The 0.3% Mo-doped  $\text{PbWO}_4$  matrix consisted of 7 crystals with dimensions of  $3 \times 3 \times 20 \text{ cm}^3$ . These were arranged as shown in the figure and the beam entered the matrix in the central crystal. Both the upstream and downstream end faces were covered with filters. [32]

One of them is the BGO matrix which was already used as electromagnetic part of the combined calorimeter discussed in the previous

section. Its performance has been compared to the one of a matrix consisting of 7  $\text{PbWO}_4$  crystals doped with 0.3% of Molybdenum [32].

The beam entered this matrix in the central crystal. The light produced by electrons showering in this matrix was read out by a total of 14 PMTs located at opposite ends (2 PMTs for each crystal). Both the upstream and downstream end faces of the matrix were covered with optical transmission filters.

Figure 54 shows the energy resolution measured for the Cherenkov signals, as a function of energy. The data points were derived using UV filters at both ends of the crystal matrix, in two different combinations for high and low energy measurements.

From the study of the crystal matrices, it has been noticed that the Cherenkov light yield results smaller with respect to the one measured with single crystals. This difference is due to the fact that the measurements with single crystals concerned particles traversing the crystal at the Cherenkov angle, thus maximizing the light yield.

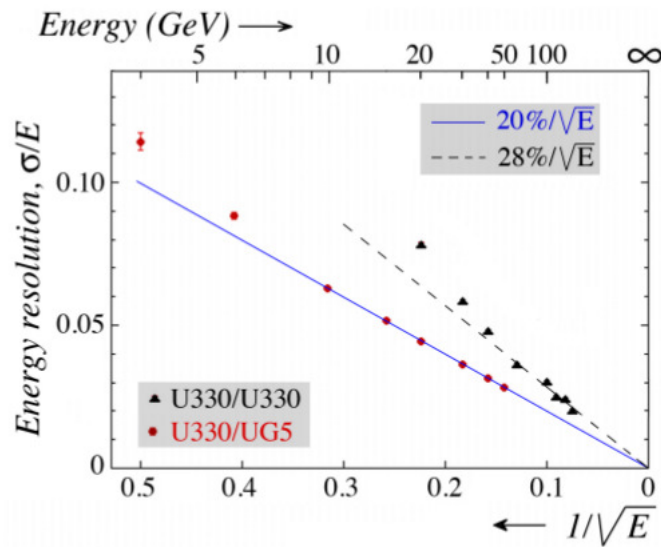


Figure 54: Energy resolution for electrons showering in the  $\text{PbWO}_4$  crystal matrix, as a function of energy. The data points concern the resolution measured for the Cherenkov signals, derived from two combinations of UV-filtered light detected at both ends of the crystal matrix. [32]

The conclusion reached after a long and in-depth study of crystal performances is that no significant improvements in terms of the Cherenkov light yield seem to be offered by the use of crystals in combination with filters in dual-readout calorimeters.

The DREAM Collaboration decided therefore to focus hereafter on the fiber option only.

### 2.2.3 The NewDREAM module

During the spring of 2011 a new prototype of dual-readout fiber calorimeter was built by the Pavia DREAM Group. Lead was used this time as absorber medium. The performance of this calorimeter were studied in two beam test periods: one which took place in November 2011 and another in July 2012. My thesis work consisted mainly in the analysis of data taken in these periods and in the participation to the July 2012 testbeam activities. The results I have obtained are described in Chapter 4.

Moreover, I collaborated to the construction of new lead/fibers modules started at the beginning of 2012 in Pavia. Details of the construction procedure are given in Chapter 3.

# 3

## CONSTRUCTION OF LEAD/FIBERS MODULES

During the year 2012 nine NewDREAM lead/fibers modules have been built by the Pavia DREAM Group. During my thesis period I participated to the construction of some of them with the technical staff.

In the following paragraphs the steps of module construction will be described. The modules built in 2012 will be tested during November 2012 testbeam. Those nine modules will form a  $3 \times 3$  matrix, as shown in Figure 55. Such matrix will be part of the final full containment NewDREAM calorimeter, a  $6 \times 6$  modules structure which will be built and tested in the next years and is the final goal of the DREAM project.

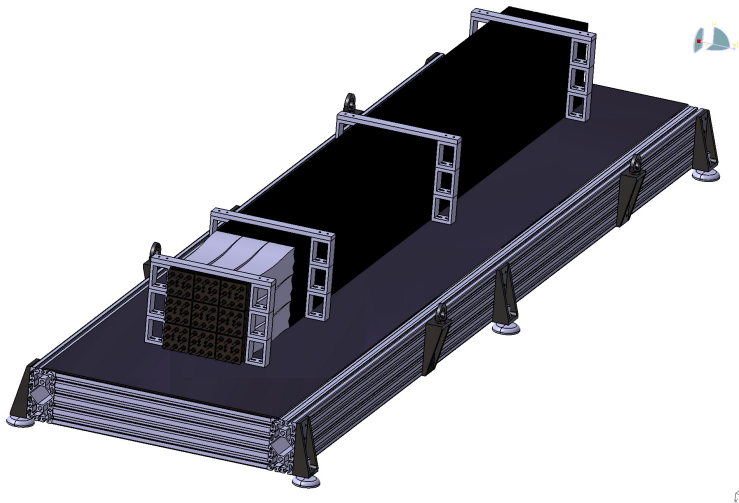


Figure 55: A 3-dimensional representation of the  $3 \times 3$  modules matrix, which will be tested in November 2012. The 9 lead/fibers modules composing it can be seen, together with the base structure.

### 3.1 CHOICE OF MATERIALS

Each module is created by stacking layers of lead with a proper geometry with layers of scintillating or Cherenkov fibers. The characteristics of both material will be described in the following.

### 3.1.1 Lead plates

#### 3.1.1.1 Profile and extrusion

Lead plates are provided by an Italian extrusion company (Lead-Extrusions srl) which produces pure lead shaped profiles. The company realises such plates expressly for our project and has worked for months, during 2010 and 2011, in order to optimize the production for our purposes. The mechanical drawing of the extruded profile with the final geometry can be seen in Figure 56.

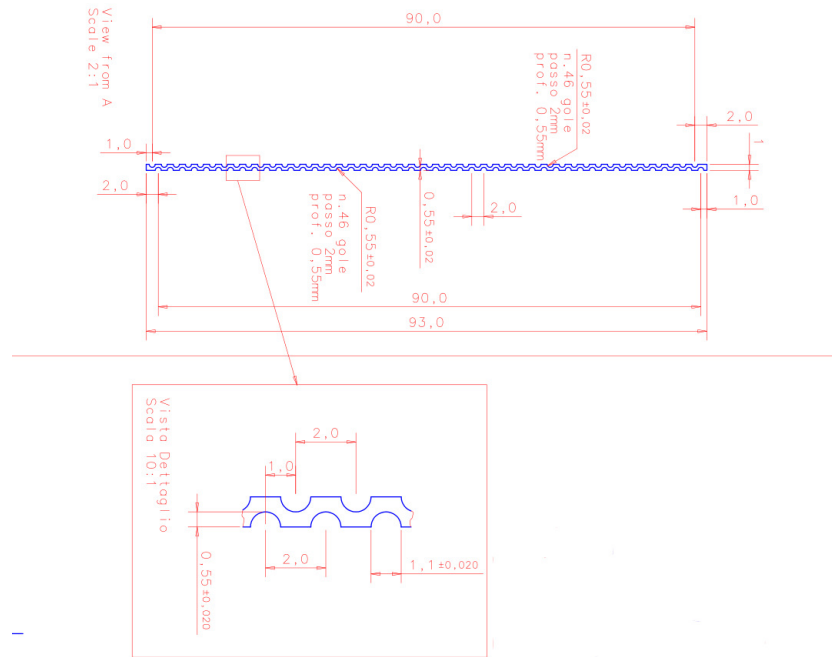


**Figure 56:** A scheme of the extruded profile of lead plates. The plate has a nominal thickness of 1 mm and a fiber-to-fiber distance of 2 mm.

Some prototypes of lead plates with different thickness have been produced by the company before starting of the production, in order to allow us to choose the best solution. We however noticed that plates with a thickness less than 1 mm were not resistant enough and easily bent. Moreover, the thickness and fiber-to-fiber distance of such plates was not constant, thus making the stacking process more difficult. We therefore asked that each plate had a nominal thickness of 1 mm with a tolerance of  $\pm 0.05$  mm, a fiber-to-fiber distance of 2 mm and a width of 9.3 cm.

Plates are obtained by cold extrusion. In this process, lead is exposed to the relatively low temperature of  $\sim 100$  °C, thus resulting in a lower shrinkage of the material with respect to hot extrusion. Therefore cold extrusion allows to obtain the requested tolerance.

### 3.1.1.2 Geometry

The geometry chosen for the lead profile represents the best compromise between the limitations given by the production technologies and the need to maximize the sampling fraction and the sampling frequency of the calorimeter. The electromagnetic energy resolution of a fiber calorimeter is given by the formula (see Section 1.6.2)

$$\frac{\sigma}{E} = 2.7\% \sqrt{\frac{d}{f_{\text{samp}}}}, \quad (39)$$

and therefore depends on the diameter of the fibers  $d$  and on the sampling fraction for mips  $f_{\text{samp}}$ . This formula will be better commented in Section 3.2.2. Now one only has to notice that, once  $d$  is fixed, the only way one can optimize  $\sigma/E$  is by increasing the sampling fraction.

Alternating Cherenkov and scintillating fibers in a single layer would represent the optimal geometry for the dual-readout purpose. Nevertheless this solution, which is pursued by the Pisa Group in the construction of their copper/fiber module, would take a much longer work time and would be easily subject to errors during the assembly stage. The chosen geometry, therefore, is the one shown in Figure 57, namely a regular structure with equidistant fibers.

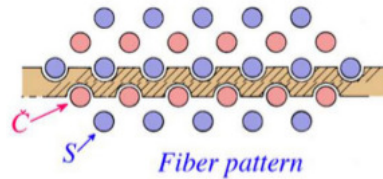


Figure 57: The fiber pattern used in the modules construction. The two different colours correspond to different fiber types.

### 3.1.1.3 Lead vs. copper

Two different materials have been considered to be used as absorber medium: lead and copper. Both of them present advantages and disadvantages.

A comparison between the advantages of the use of copper or lead as absorber medium is summarized in the following.

- Much smaller detector mass and dimensions would be required with copper. In fact, copper has both a shorter nuclear interaction length (151 mm vs. 170 mm for lead) and a smaller density (8.96 g/cm<sup>3</sup> vs. 11.3 g/cm<sup>3</sup> for lead) with respect to lead.
- Both the materials present an enhancement of the Cherenkov light yield. Concerning copper, this is due to the fact that Cherenkov light is almost exclusively produced by em shower components in hadron absorption and the  $e/mip$  ratio is higher for

copper (0.9) with respect to lead (0.6). Therefore, for a calorimeter with a given sampling fraction, one gets  $\sim 50\%$  more Cherenkov photons per GeV of deposited energy. Since Cherenkov light yield is one limiting factor for energy resolution of hadronic calorimeters, the latter could be optimized by the use copper as absorber. On the other hand, in the lead case, the Cherenkov light yield is also enhanced since lead has a lower critical energy with respect to copper, thus implying that more shower particles (and therefore more electrons and positrons) are present. These effects, however, aren't easily evaluable and a Monte Carlo simulation should be required in order to estimate the differences. Nevertheless such a simulation would be complex, since the Cherenkov component in hadronic showers is not easily parameterizable.

- Fluctuations in the low-energy hadronic content of jets are smaller for copper than for lead. In fact a substantial fraction of jets energy is carried by fragments with energies  $<$  than 5 GeV. At such low energies hadrons are likely to not develop showers, but rather to range out, acting like mips. This effect, which leads to non-linearities in energy resolution, is smaller for copper than for lead, because of their different  $e/mip$  ratios (0.9 and 0.6, respectively).
- Lead has a greater malleability, which offer the possibility of using an extrusion process in order to get the required geometry.
- Lead extruded profiles are cheaper with respect to copper formed or machined profiles.

Considering all these factors, the DREAM collaboration decided of using both the materials in the construction. Modules built in Pavia have lead as absorber medium, while the Pisa collaboration has been involved in the construction of two copper/fiber calorimeter modules. All these modules have been tested in July 2012 at the H8 beam line of CERN SPS. The online analysis of data taken during this testbeam hasn't highlighted any substantial difference in their performances. However, a more careful offline analysis is ongoing.

### 3.1.2 Fibers

Fibers are supplied by two different companies. Those devoted to the detection of scintillation light are of the type SCSF-78 and are produced by Kurayay. Concerning the fibers used for Cherenkov light detection, they have a polymethyl methacrylate (PMMA) core and are produced by Mitsubishi.

Before the beginning of the construction, the properties of two different plastic materials have been studied, that is PMMA and poly-

styrene (PS). PS fibers were originally chosen to build a first Pisa module, which has then been tested with electron beams at testbeam. In fact, because of their higher numerical aperture (0.72) with respect to PMMA ones (0.50), the Cherenkov light yield of such fibers (which was measured with a LED) resulted to be of 32 p.e./GeV, twice that of PMMA fibers. However, self-absorption of Cherenkov light at  $\lambda < 5$  nm occurred in PS fibers, because of Rayleigh scattering. On the other hand, owing to the different core material, PMMA fibers present a much lower self-absorption at shorter wavelengths, as it can be seen in Figure 58.

Therefore PMMA fibers were chosen to be used to build the first prototype of NewDREAM lead/fibers module (the analysis of data taken with such module is reported in the next chapter). This module has been tested with electron beams using the same identical readout of the Pisa one and the results obtained with both modules have been compared.

The results of the test are shown in Figure 59. It can be seen that no change occurred for the scintillation signal, while the Cherenkov signal doubled. We deduced then that the effect of a smaller numerical aperture of PMMA fibers is more than offset by the decreased light absorption in the short-wavelength region that dominates the Cherenkov spectrum.

Therefore, PMMA fibers have finally been chosen for the construction of the 2012 modules.

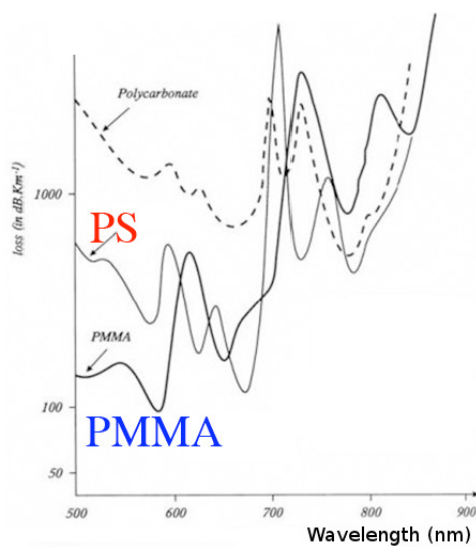


**Figure 58:** Comparison of self-absorption of PS and PMMA fibers. As it can be seen, PMMA fibers are much less absorbent in the short-wavelength region that dominates the Cherenkov spectrum.

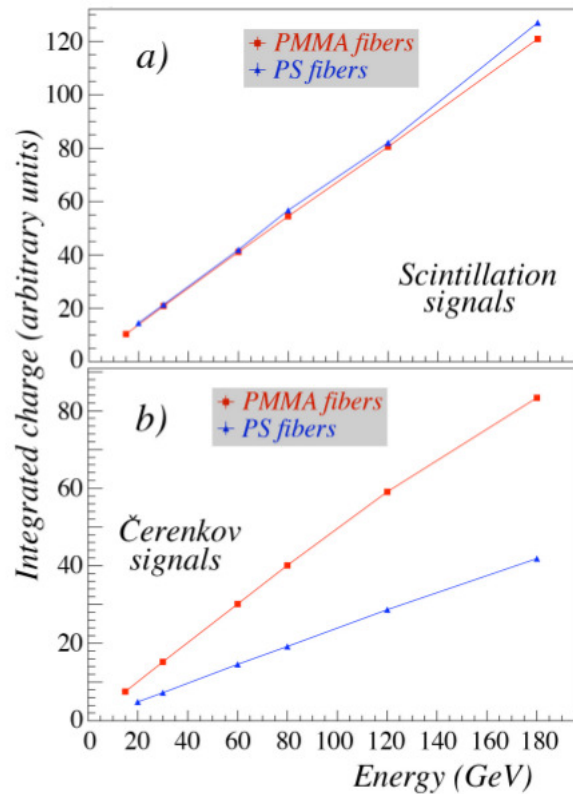


**Figure 59:** Comparison of scintillation and Čerenkov signals obtained from the test of two modules with PS and PMMA fibers, respectively. The scintillation signal doesn't change, while the Čerenkov signal doubles.

### 3.2 CONSTRUCTION

Extruded lead is shipped by the producer rolled up on a reel. Each reel is made of about 30 meters of profile. The first step in the construction of the modules is to unroll the lead (Figure 60a) and cut it at the proper length, which is 2.5 m, corresponding to  $\sim 10 \lambda_{int}$ . The cutting process is shown in Figure 60b. Once the plate has been cut it needs to be stretched by means of a roller, in order to eliminate possible humps, as it is showed in Figure 60c. Because of the cutting, lead grooves at the extremes of the plates may damage their profile. For this reason, after each cutting, they need to be restored by means of a comb, as it can be seen in Figure 60d.

Once the lead layer is ready, it is placed on a worktable, where the stacking process occurs.

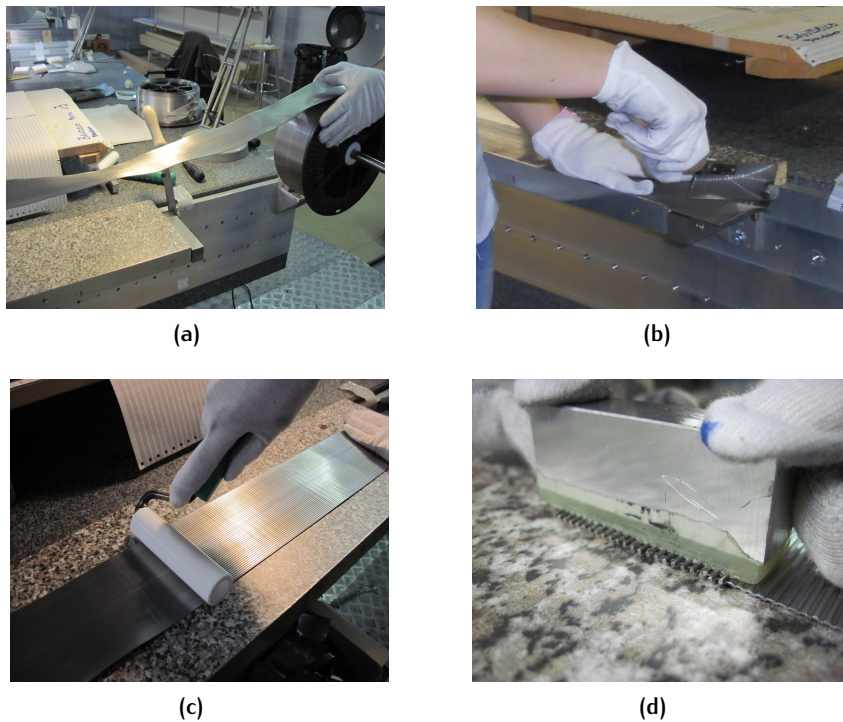


**Figure 60:** Detail of the lead reel (a), of the cutting of the rolled lead (b), of its stretching with the roller (c) and of the redefinition of the grooves profile with the comb (d).

A layer of fibers is created, by laying carefully 46 fibers of a given type in each of the lead grooves. They are then fixed at an extremity of the layer and stretched over all the length of it. Finally, another lead layer is carefully placed on the fibers, making them match the lead grooves. The stacking continues, alternating layers of Cherenkov and scintillating fibers, until the height of the module reaches 9.3 cm. At each stacking stage, the extremities of the module need to be fixed by means of clamps, since no glue is used in the construction of the Pavia modules to keep them fixed, differently from the Pisa copper module. This is illustrated in Figure 61a and 61b, which shows both the front and the rear end of the module. Figure 61c shows the rear end of the module, from which the bunches of fibers depart, 4 bunches for each type of fiber.

Only a few numbers of layers (on average 10) per day could be stacked, because after some stages an overlap of the various irregularities of both fibers and lead plates occurred, thus resulting in the displacement of the fibers. At the end of the day, the layers were left fixed and pressed by clamps all night, in order to reduce irregularities. A picture of the closed module at the end of a work day is given in Figure 62.

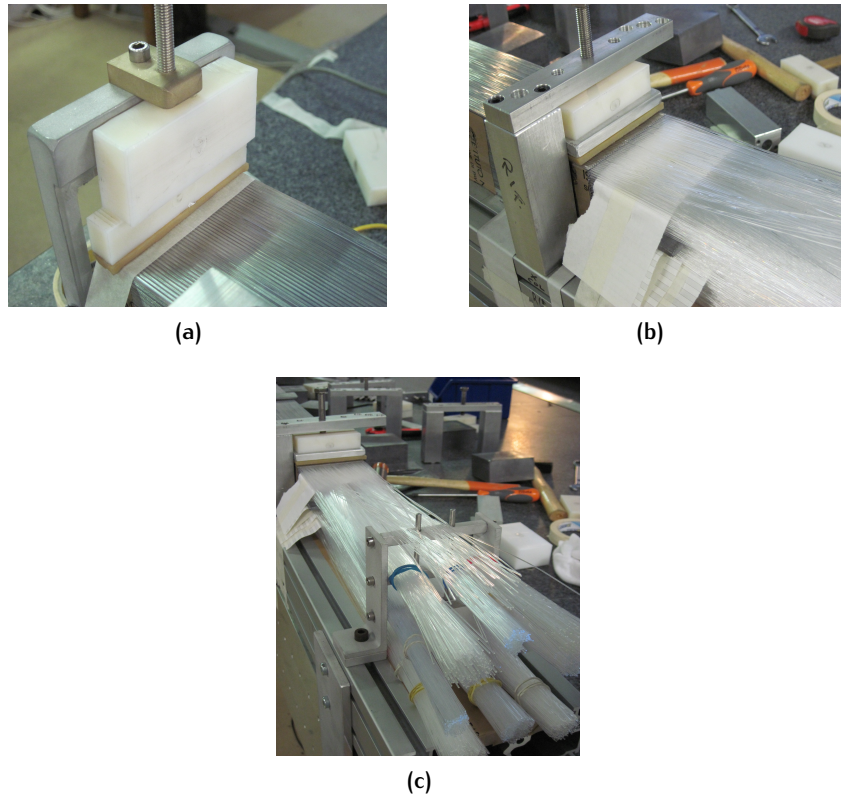


**Figure 61:** Details of the fixing of the layers during construction: the front end of the module (a), the rear end (b) and the fiber bunches departing from the rear end (c).

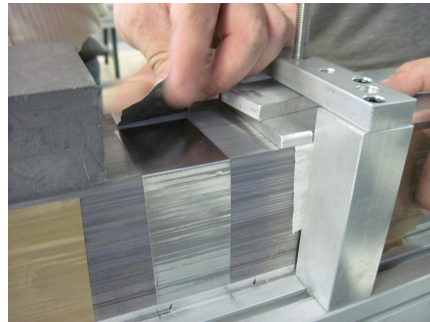


**Figure 62:** A picture of the module fixed and pressed by clamps for the night.

Once the module has been completed, it needs to be moved away from the worktable. In order to do so, we firstly fix the module by means of a Pb based adhesive tape. This is made of a  $120\ \mu\text{m}$  thick lead layer and a structural glue. We then position an aluminum plate

on the top of module and we move it by means of an aluminum bar with vacuum suckers, which works exploiting the Venturi effect. A series of tests has been previously made in order to ascertain if the 20 suckers of which the bar is equipped could bear the weight of the module, which is about 150 kg. These final operations of wrapping and moving the module are shown in Figure 63a and 63b. Figure 63c shows, instead, the completed modules moved away.

The method used to move the modules by means of suckers will be the same that will be used in the November 2012 testbeam for the positioning of all the modules to be tested.



(a)



(b)



(c)

**Figure 63:** Detail of the wrapping of the module with the lead tape (a) and of its moving from the worktable (b). Some completed modules are shown in (c).

### 3.2.1 Thickness non-uniformity of lead layers

During the stacking of the first module, it soon became evident that the thickness of the lead plates wasn't uniform over its width, thus giving rise to an unwanted "S" shape of the layers. This can be seen in Figure 64, which concerns the first lead production, which was replaced because of its bad quality. Anyway, also the following plates productions presented this problem, even if to a lesser extent, but we decided to continue the construction.



Figure 64: The "S" shape of the lead plates, caused by the non-uniformity of their thickness.

Because of this effect, I measured with the microscope the thickness of a sample of plates as a function of the position on the width (9.3 cm). A picture of the lead plate seen with the microscope is shown in Figure 65.

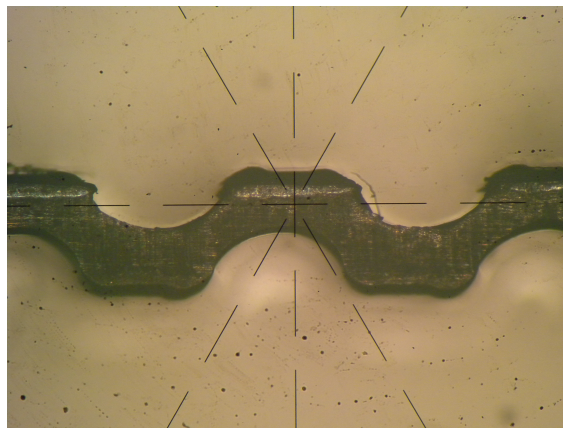
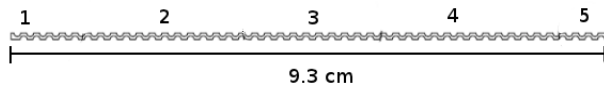


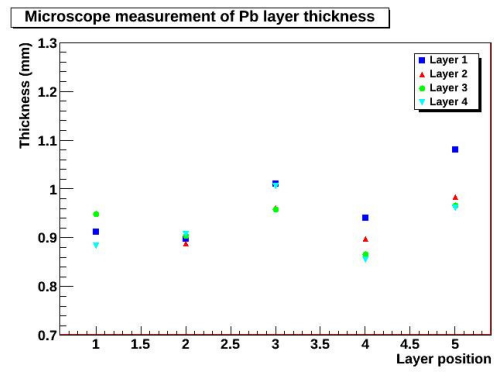
Figure 65: The lead plate profile seen with the microscope. In order to obtain the thickness of the lead plates samples I measured the distance between two consecutive heights.

I measured plates coming from two different samples, produced in February and March 2012 respectively. By comparing the measurements (see Figure 66), it results that the more recent layers have a larger non-uniformity with respect to the older ones, which amounts

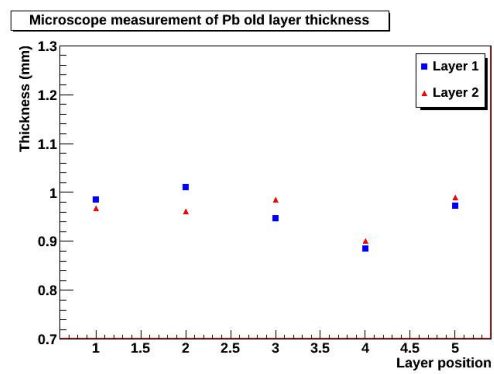
to  $\sim 10\%$  and therefore have a more accentuated "S" shape.



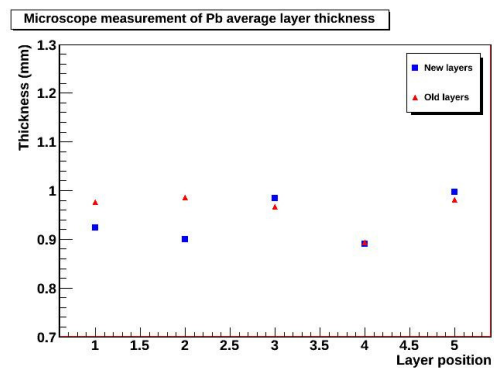
(a)



(b)



(c)



(d)

**Figure 66:** Thickness of lead layers as a function of the position on the plate (number from 1 to 5 correspond to a position varying from 0 to 9.3 cm) (a). Measurements of different samples of the new layers (b), old layers (c) and the comparison between their average values (d) are shown.

Unfortunately, the tight deadline for the construction did not allow us to replace again the production. We used therefore the more recent plates, being careful to alternate them with some coming from the older production.

Another problem arose during construction, which caused a slowdown of the stacking process, was the bad quality of the PMMA fibers, which resulted to be twisted, thus implying an extra work for their loosening.

Besides, the thickness of a sample of some lead plates was also measured during the stacking process with the sliding gauge. More precisely, we deduced the thickness of the plates after having measured the thickness of about 20 layers, in order to reduce the measurement error. It resulted that their average thickness wasn't exactly 1 mm, but had the slightly higher value of 1.1 mm, owing to the the presence of some irregularities in the lead, as it can be seen in Figure 65. Therefore the plates used in the construction turned out to be about the 10% thicker than those requested by the design, even if a tolerance of  $\pm 0.5$  mm had been given.

A total of 84 fibers layers (42 Cherenkov + 42 scintillating) and as many of lead was required to get the square section ( $9.3 \times 9.3$  cm<sup>2</sup>) instead of the 92 (46 + 46) of the 2011 module and required by the design. Another consequence of the different thickness is that the calculation of the sampling fraction for the calorimeter will give a different result with respect to the old module and the design. This will be shown in the next section.

However, a third production of lead plates (necessary for the construction of the last three modules and arrived in August) resulted to be in accordance with the nominal requirements, so that 92 fiber layers were stacked in order to build each of the last three modules.

### 3.2.2 Differences in energy resolution

We now want to calculate how much the energy resolution changes by using lead layers with a thickness different from the nominal value.

In order to estimate the energy resolution of the calorimeter, the starting point is the known formula (see Section 1.6.2) which links the energy resolution to the sampling fraction of the calorimeter, that is:

$$\frac{\sigma}{E} = 2.7\% \sqrt{\frac{d}{f_{samp}}}, \quad (40)$$

where  $d$  is the thickness of the sampling layers (the fibers, in our case) and  $f_{samp}$  is the sampling fraction for mips. This formula is valid only for fibers of the scintillating type. This is because the calculation of the sampling fraction involves the knowledge of the energy loss in the sampling medium. If the latter is constituted by Cherenkov fibers,

then the energy loss of a charged particle in such medium is almost zero, because only a small amount of energy is dissipated through Cherenkov effect. Therefore the sampling fraction of a calorimeter which has Cherenkov fibers as sampling medium is determined primarily by photon statistics and can't be calculated in a simple way. Besides, we took particular attention in the choice of PMMA fibers, which are characterized by a limited self-absorption of Cherenkov photons, in order to avoid fluctuations in the starting point of the shower.

The next step is the calculation of the equivalent height for both lead and fibers ( $t_p$  and  $t_f$  respectively). They are given by the relations:

$$L \cdot h = L \cdot t_p + 46\pi R^2, \quad (41)$$

in the case of lead and

$$46\pi R^2 = L \cdot t_f, \quad (42)$$

in the case of fibers.

In the previous equations,  $h$  is the thickness of the lead plates,  $R$  is the radius of the fibers and  $L$  is the width of the layers, as it can be seen from the schematic representation of Figure 67a.

Therefore we have  $h=1$  mm (nominal) or  $h=1.1$  mm (measured),  $R=0.5$  mm and  $L=93$  mm. Using the previous data, one obtains the values  $t_f=0.47$  mm,  $t_p=0.53$  mm (with the nominal thickness) and  $t_p=0.63$  mm (with the measured thickness).

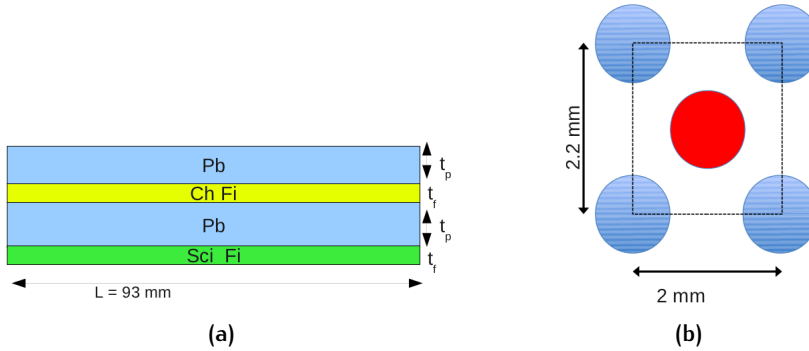


**Figure 67:** A schematic representation of how we calculated  $f_{samp}$  (a).  $t_f$  and  $t_p$  indicate the equivalent height of the fibers and the lead layers, respectively. The filling fraction of the fibers (b).

The higher thickness of the plates causes the filling fraction of each fiber to decrease. Referring to Figure 67b, the filling fraction results:

$$\pi R^2 / h \cdot S = \pi \cdot (0.5\text{mm})^2 / 1 \cdot 1.1\text{mm}^2 = 71.4\% \quad (43)$$

With nominal plates it would have been 78.5%, thus implying a difference of about 9%. Because of the decrease of the filling fraction of

each fiber, also the sampling fraction will decrease. We now calculate the sampling fraction with its definition:

$$f_{samp} = \frac{(dE/dx)_{fiber} \cdot t_f}{(dE/dx)_{Pb} \cdot t_p + (dE/dx)_{fiber} \cdot t_f} \quad (44)$$

The tabulated values for the stopping powers, taken from PDG, are:

$$\left(\frac{dE}{dx}\right)_{fiber} = 2.29 \text{ MeV/cm}; \quad (45)$$

$$\left(\frac{dE}{dx}\right)_{Pb} = 12.73 \text{ MeV/cm} \quad (46)$$

It therefore results:

$$f_{samp}(h = 1 \text{ mm}) = \frac{2.29 \cdot 0.47}{2(12.73 \cdot 0.053 + 2.29 \cdot 0.47)} = 0.0688; \quad (47)$$

$$f_{samp}(h = 1.1 \text{ mm}) = \frac{2.29 \cdot 0.47}{2(12.73 \cdot 0.063 + 2.29 \cdot 0.47)} = 0.0592 \quad (48)$$

The values found for  $f_{samp}$  can be used for calculate the energy resolution, using Equation 40. We obtained:

$$\frac{\sigma}{E}(h = 1 \text{ mm}) = 2.7\% \sqrt{\frac{1}{0.0688}} = \frac{10.29\%}{\sqrt{E}}; \quad (49)$$

$$\frac{\sigma}{E}(h = 1.1 \text{ mm}) = 2.7\% \sqrt{\frac{1}{0.0592}} = \frac{11.1\%}{\sqrt{E}} \quad (50)$$

This means that the resolution is worse of a factor  $0.81\%/\sqrt{E}$  with respect to the one we would have obtained the lead plates have had their nominal thickness. Because of the relative smallness of such worsening, we decided to continue with the production.

### 3.3 READOUT

As I said at the beginning of this chapter, the modules built during 2012 will be tested at November 2012 testbeam. The tested matrix will be supposedly made of nine of such modules, arranged in the structure illustrated in Figure 55.

In order to provide the readout of the sampling medium, the fiber bundles need to be connected to the photomultiplier tubes. The connection which will be used in November 2012 testbeam will be the same adopted in November 2011 and July 2012 testbeams, when a single NewDREAM lead/fiber module was tested.

For each module, eight fiber bundles (4 scintillating and 4 Cherenkov) depart from the rear end, as it was seen before (see Figure 61c). Each fiber bundle is inserted in a cup and fixed with glue, as it is

shown in Figure 68a. All bundles are then milled, in order to obtain a smooth surface (Figure 68b). Each milled bunch is then connected to a PMT (Figure 68c) by means of the mechanical structure shown in Figure 69. Details of the photomultiplier used will be given afterwards in Section 4.1.2.4.

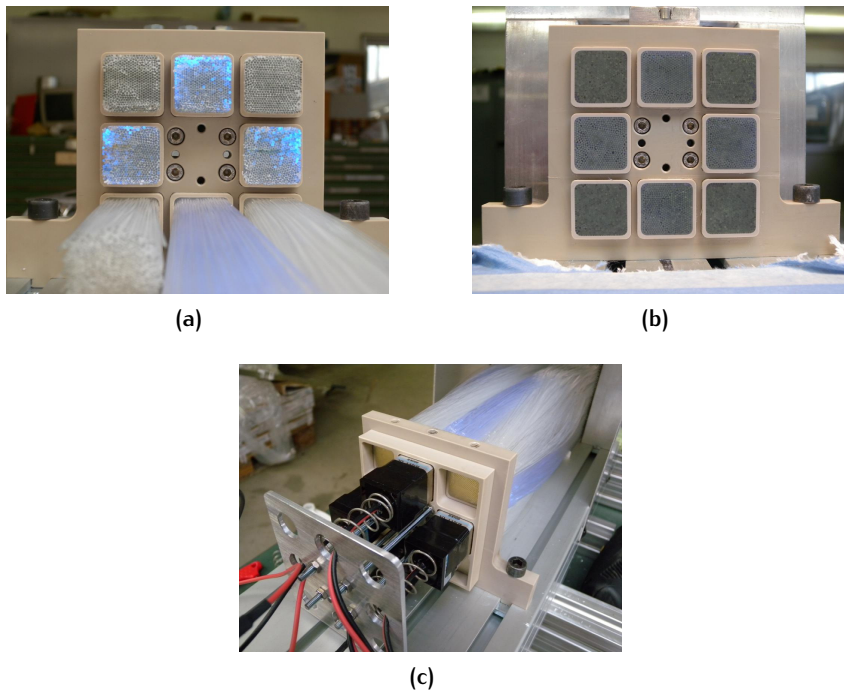


**Figure 68:** Fiber bunches departing from the rear end of the module before milling (a), after milling (b) and their connection to the PMTs. The pictures concern the first NewDREAM lead/fibers module tested during the November 2011 and July 2012 testbeams.

As described in the next chapter, the analysis of data taken with NewDREAM lead module during November 2011 testbeam revealed a non-uniformity of the detected signal with respect to the different position of incidence of light on the photocathode. This is due to the fact that the PMTs collection efficiency varies with the position of incidence on the photocathode, as it will be described in Section 4.1.3.5.

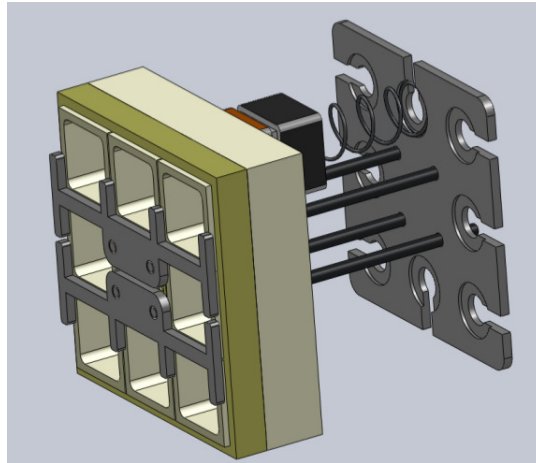


**Figure 69:** A 3-dimensional representation of the mechanical structure used to connect the photomultiplier tubes to the fiber bunches.

In order to avoid such non-uniformities in the detection of the signal, a possible solution which could be implemented in the November 2012 testbeam would be the addition of a light guide before the connection of the photomultiplier tubes. In this way light coming from different areas of the calorimeter would be mixed before reaching the photocathode.

One has nevertheless to consider that inserting a light guide before the PMTs could cause a relevant absorption of Cherenkov light. For this reasons other groups of the DREAM collaboration (Roma, Cagliari and Pisa) have performed a study in order to obtain a compromise between light mixing and absorption of Cherenkov wavelengths.

Two types of light mixers have then been tested during July 2012 testbeam. The results of these tests will be given in Section [4.2.2.1](#).

### 3.3.1 Ideas for readout optimization

The analysis of data taken during November 2011 testbeam with the NewDREAM lead/fibers module has emphasized the non-linearity of the calorimeter for electron detection, as it will be seen in the next chapter. Non-linearity could be caused by the readout electronics, which does not sustain a change of dynamic range so wide (4-180 GeV). One of the reasons for this effect is given by the too much high gain of PMTs ( $G \sim 5 \times 10^4$  at 600 V). They are provided by Hamamatsu with standard bases and, because of the wide range of electron beam energies used to test the module, their high gain causes saturation effects at the higher energies. In order to overcome this problem, different solutions have been studied by the Pavia electronic team. In view of the test of a 3x3 matrix of lead/fibers modules, only the central towers will be equipped with the new readout, because it is the

one where most of the signal gathers and, therefore, saturation effects occur. We have investigated those effects in details and some possible improvements, which have been tested during July 2012 testbeam with the first NewDREAM lead/fibers module, are listed below.

- A new PMT base has been realised, by modifying the standard Hamamatsu base. The scheme of voltage dividers suggested by the company has been followed and a proper voltage divider has been added in order to lower the gain. Lowering the gain allows the PMTs to be efficient in a wider energy range. The new bases have been preliminary tested with a LED, in order to obtain different signal amplitudes. They have been then tested in July at the SPS, and the results of such test will be given in the following chapter.
- Moreover, low energy signals are overcome by PMTs noise and are hard to be detected. For this reason, a possible improvement would be that of adding an external amplification stage of PMTs signals at low energies. Some of such PMTs have been realized and tested in July, having thus two readout channels: a 10x amplified channel that will be used for low energy runs in addition to an 1x gain channel.
- The voltage between the last PMT dynode and the readout can be significantly reduced owing to space charge effects which occur in that region, where the number of photoelectrons is high. This effect contributes to the non-linearity of the calorimeter response. Therefore, in order to counteract this effect, it has been considered the possibility of adding a removable voltage generator to the last dynode of the new bases.

Besides the test of these supposed improvements in the readout, the grounding of the whole experimental apparatus has been improved during the July 2012 testbeam.

The analysis of data taken on this occasion will be presented in the next chapter.

Given the results, the DREAM Collaboration is considering what changes to apply to the readout in view of November 2012 testbeam.



# 4

## DATA ANALYSIS ON NEWDREAM LEAD MODULE

A large fraction of my thesis work has been devoted to the analysis of data taken with the NewDREAM lead-fiber module built in Pavia during the spring 2011. It was tested both in the October/November 2011 and in the July 2012 testbeam periods. In the latter case I also took part actively to the data taking of the testbeam.

In both testbeams the module has been tested with electron and hadron beams, with energies between 4 and 180 GeV, at the H8 beam line at CERN Super Proton Synchrotron (SPS).

In the next sections, after the description of the experimental setup used in the testbeams, I will present the results of the analysis I carried out.

### 4.1 OCTOBER/NOVEMBER 2011 TESTBEAM

#### 4.1.1 The H8 beamline

In order to obtain beams to be used in the testbeam area, firstly a 450 GeV proton beam is extracted from the SPS. This is then split in three beams, one of which is directed against a primary target. This primary beam has typical intensities of a few  $10^{12}$  protons per burst. From the target three secondary beams of hadrons (*e.g.* pions) are derived, to be used at different beamlines, one of which is the H8 beamline.

In order to get a pure electron beam, separation of electrons from hadrons is achieved by using their energy loss due to synchrotron radiation in high-field bending magnets (dipoles), followed by collimation of the hadrons.

Since the electron beam obtained in this way is not a primary one, it exhibits a limited purity, especially for energies close to the one of the hadrons from which it originates. For this reason, auxiliary detectors are needed in order to provide information to clean the beam from contaminating particles, such as muons and hadrons originated from the collision with the target, as it will be described in the following section.

#### 4.1.2 Experimental setup

In this section the experimental setup adopted in the October/November 2011 testbeam period will be illustrated. A simple scheme of it is represented in Figure 70.

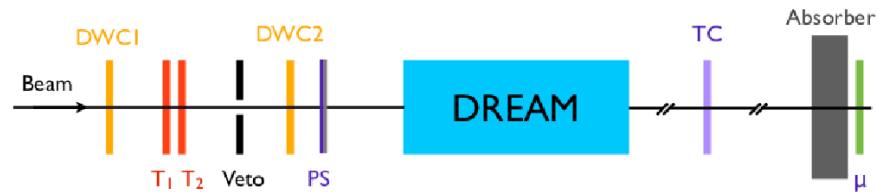


**Figure 70:** The experimental setup used to test the performance of the Pavia NewDREAM module. The figure is not in scale.

##### 4.1.2.1 Beam position

In order to get information about the trajectories of beam particles and reconstruct them, two Delay Wire Chambers (DWC<sub>1</sub> and DWC<sub>2</sub>) were used. DWCs consists of a sandwich of two cathode planes surrounding a central anode wire plane. The principle of working of such detectors is the same of that of any other Multi Wire Proportional Chamber. A particle passing through the chamber will ionise the gas and create free electrons and positive ions. Electrons are then accelerated towards the 20 micron anode wires, where avalanche multiplication takes place, by the high voltage between anode and cathodes. An image current is induced on the cathode wires closest to where the anode avalanche took place. Individual cathode wires are connected to a tapped delay line. The induced signal from the cathode wires is actually used to obtain the position information, in the following way. The sum of the signals of different wires build up two waves in the delay line, one in each direction. The anode signal is used as a common start and the time delays for the integrated waves to reach the amplifiers at each end of the delay line are measured by means of a Time to Digital Converter (TDC). The latter is a device which converts a time interval measurement in digital form. By subtracting the value measured at the left end of the delay line from the one measured at the right end, one finds the horizontal coordinate. A second sandwich of cathodes and anode placed orthogonally in the same housing provides a full two dimensional position reading (now the vertical coordinate is obtained by subtracting the value measured at the top from the one measured at the bottom of the delay line). In this way the impact point can be determined with a resolution of typically 200  $\mu\text{m}$ .

The DWCs need to be calibrated, in order to convert temporal information to position, and this procedure has to be done at the be-

ginning of each testbeam period. In order to calibrate the DWCs, an appropriate pulse shape is given to the chamber by means of a dedicated pulse generator. The horizontal coordinate is obtained from the TDC signal in the following way. Three points of the DWC are excited, that is the points at -30 mm, 0 mm (in the center) and 30 mm. Three reference points are therefore obtained and fitted with a straight line. The timing information of the TDC is then converted in mm by means of the relation:  $X_{position} = \Delta t \cdot Slope_{horizontal} + Offset_{horizontal}$ , where  $Slope_{horizontal}$  and  $Offset_{horizontal}$  are the parameters of the fit. The same procedure is applied to obtain the vertical coordinate.

#### 4.1.2.2 *Trigger*

Between the two tracking chambers, two small scintillation counters (T1 and T2), each with a thickness of 2.5 mm and an area of overlap of  $4 \times 4 \text{ mm}^2$ , are installed, together with a veto counter. The latter, which is a simple scintillator with a thickness of 1 cm and an area of  $15 \times 15 \text{ cm}^2$ , has a hole with a diameter of 2 cm in its center. T1, T2 and the veto counter provide the trigger for the data acquisition system, by considering a coincidence between the two trackers, combined with the absence of a signal in the veto counter. The latter is used to reduce the beam halo and the divergence of particles arriving at a big angle with respect to the direction of the beam.

#### 4.1.2.3 *Beam cleaning*

In order to clean the event samples, by recognizing and eliminating contaminating beam particles, some auxiliary detectors are present. They provide information that will be used in my analysis, as it will be seen.

A preshower detector (PS), consisting of 5 mm ( $\sim 1 X_0$ ) of lead followed by a plastic scintillator and placed  $\sim 50$  cm upstream the fiber module, provides the elimination of the hadrons and low-energy muons contributions to the event signals. In fact in such a detector, as previously mentioned in Section 1.4.2.4, pions and muons generally produce a mip signal, while electrons start showering in lead, thus producing a much larger signal.

A simple  $20 \times 20 \text{ cm}^2$  scintillator paddle placed about 1 m behind the calorimeter plays the role of tail catcher (TC). Because of the different scaling between em and hadronic showers, electron showers are in general completely contained in the fiber module, while this is not the case for hadronic ones. For this reason, the tail catcher is useful to clean the signals from hadronic contributions on electron beam.

Finally, a muon counter, consisting in a  $50 \times 50 \text{ cm}^2$  scintillator paddle installed 20 m away from the experimental area and behind the beam dump (absorber), provides a further improvement of the signal, by recognizing contaminating muons of higher energies that have not

been stopped by the absorber, differently from other types of particles.

The readout of all three auxiliary detectors is provided by an Analog to Digital Converter (ADC), an electronic device which converts the information contained in an analog signal (in this case the pulse shape of the scintillators) to an equivalent digital form (ADC counts). The ADC can therefore convert an input signal with a certain amplitude in a digital number which is proportional to the charge released on scintillators.

Figure 71 shows a foreshortening of the auxiliary detectors.

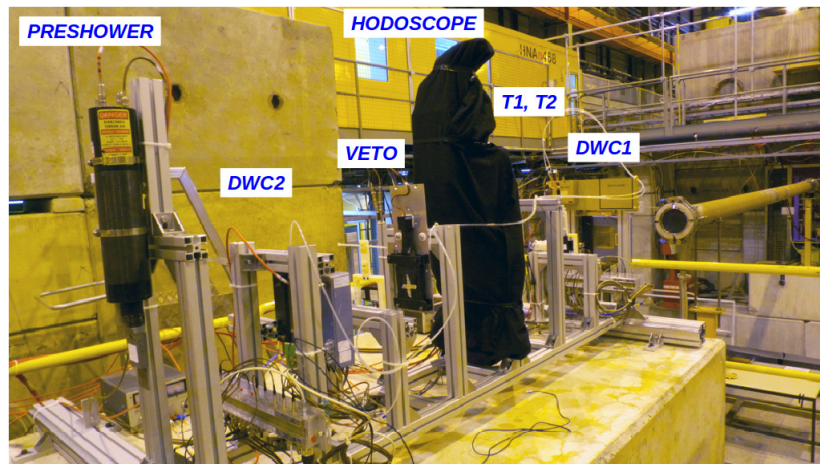


Figure 71: Picture of DREAM testbeam area, which is placed downstream the calorimeter. The auxiliary detectors are indicated (the hodoscope wasn't discussed because it wasn't used in this analysis). The beampipe, from which the beam comes, is also visible.

#### 4.1.2.4 Positioning and readout

As it was described in the previous chapters, the NewDREAM module consists of a 2.5 m long lead absorber+fibers structure, with fibers individually embedded in the absorber. The module is conveniently divided into four towers and, at the rear end of it, Cherenkov and scintillating fibers are bunched separately in a way that two bunches (one Cherenkov and one scintillating) exit each tower and stick out over a distance of about 0.5 m.

A scheme of the structure of the Pavia module is showed in Figure 72b.

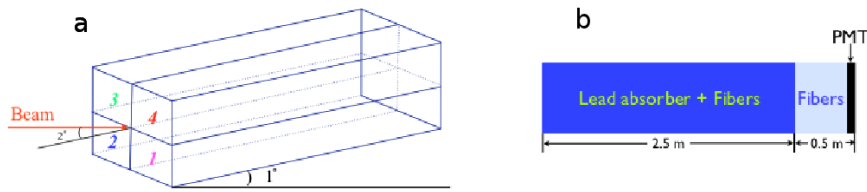


Figure 72: The tower structure of the module and its positioning (a); the scheme of the structure of the Pavia module (b).

The module is placed on a platform, so that its position with respect to the beam can be remotely controlled. Figure 72a shows the tower division of the module and its positioning in the experimental area, where it was tilted by  $1^\circ$  in the vertical plane and rotated by  $2^\circ$  in the horizontal plane, in order to avoid channelling effects. The whole calorimeter module and the PMTs are contained in a box, in order to prevent the entrance of light and detect only the calorimeter signals.

Two PMTs for each tower provide the readout of the fiber signals. We used 8 Hamamatsu 8900 PMTs, each with a photocathode area size of  $23.5 \text{ mm}^2$  and 10 multiplication stages. They were equipped with a borosilicate window and those devoted to the detection of Cherenkov light had also a superbi-alkali cathode (model 8900-100), in order to increase the quantum efficiency. The PMTs devoted to the detection of scintillation light were coupled with a long-pass GG495 (yellow) filter, which only transmits light with  $\lambda > 495 \text{ nm}$ . The yellow filter is used in order to select the spectral component that is not absorbed by the fibers. In this way the position dependent effects are avoided. The readout of the PMTs was performed by the ADC.

#### 4.1.3 Data analysis

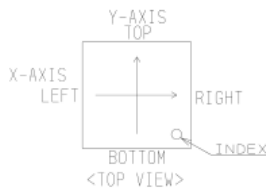
The main purpose of my analysis work on October/November 2011 data was to investigate possible non-uniformity effects in the signals. In order to do that, I performed a position scan of the Tower 4 (T4) beamspot area. Before doing so, I made a previous general analysis, which will be illustrated in the following paragraphs. More precisely, I studied the electromagnetic resolution and the calorimeter response linearity of data taken with electron beams of various energies, which are listed in Table 3, which also gives the statistics for each run.

I used runs with the beam centered on T4, in order to avoid the so called *4-corners region*, which is located in the center of the module. The reason why one wants to avoid the 4-corners region is that it presents strong non-uniformities, owing to the fact that the PMTs

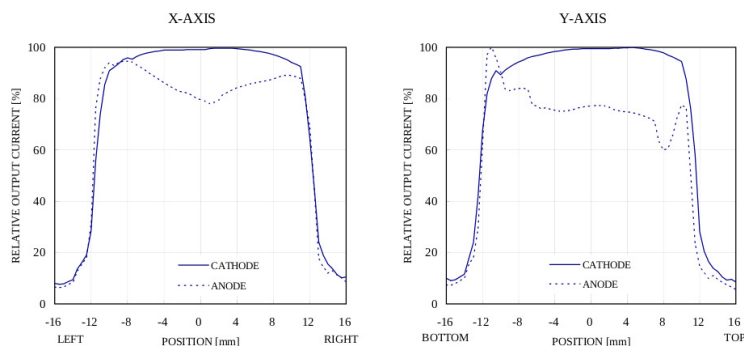
collection efficiency varies with the position of the incident light on a photocathode, thus influencing the spatial uniformity of the PMT. This can be seen in Figure 73, where the sensitivity of a PMT is showed as a function of the position of incidence on it. Since fibers located at the center of the module are read out by the borders of the PMTs, corresponding to the tails of the sensitivity plot, the mentioned non-uniformities originate.

Table 3: Electron beam energies and statistics of the runs used in the analysis.

Energy (GeV)	N <sup>o</sup> of events
4	7000
6	5000
10	10000
15	10000
20	10000
30	10000
40	10000
50	20000
80	10000
100	10000
150	10000



(a)



(b)

Figure 73: Spatial uniformity of a photomultiplier tube.

I also selected events, by means of the DWCs, in one quadrant of the beam spot located most closely to the module center, in order to minimize the effects of non-containment.

For events selected with the previously explained criteria, the electron energy deposit in Tower 4 was typically the 80-90% of the energy deposit in the whole calorimeter.

#### 4.1.3.1 Calibration constants

In order to get the energy distribution of the signal from the ADC distribution and to sum the four towers in a consistent way, the calibration constants for the four calorimeter towers need to be derived. In this section the method used to obtain them will be described.

The starting point is the assumption that the full electron energy is contained in a  $3 \times 3$  matrix of towers. Therefore, as it can be seen in Figure 74, each of the four towers is supposed to be surrounded by eight towers, three of which are real and the other five are virtual. The signal in the five virtual towers can be deduced by symmetry considerations. Let's take as example the calibration of Tower 4. In this case, the energy deposits in the real peripheral Towers 1, 2 and 3 should be the actual measured signals. Concerning the five virtual towers, because of symmetry reasons, one of them should have the same energy deposit as Tower 1, another one the same as Tower 3 and the three remaining virtual towers should have the same signal as Tower 2. This is illustrated in Figure 74.

1	2	1	2
4	3	4	3
1	2	1	2
4	3	4	3

Figure 74: The four real towers (in red) to be calibrated and the five virtual towers (in white) surrounding them.

Reasoning in this way, one gets the following four equations with four unknown quantities, which are the calibration constants  $c_1$ ,  $c_2$ ,  $c_3$  and  $c_4$  for Tower 1, 2, 3 and 4 respectively:

$$c_1 T_1 + 2c_2 T_2 + 4c_3 T_3 + 2c_4 T_4 = E \quad (51)$$

$$2c_1 T_1 + c_2 T_2 + 2c_3 T_3 + 4c_4 T_4 = E \quad (52)$$

$$4c_1 T_1 + 2c_2 T_2 + c_3 T_3 + 2c_4 T_4 = E \quad (53)$$

$$2c_1T_1 + 4c_2T_2 + 2c_3T_3 + c_4T_4 = E \quad (54)$$

In the previous relations,  $T_1$ ,  $T_2$ ,  $T_3$  and  $T_4$  are the average measured tower signals (obtained after equalizing the gains and with the beam centered on each tower, by means of the remote position control) and  $E$  is the beam energy.

Since the response of the detector resulted to be non-uniform with respect to the position on the module, as it will be seen in the next sections, the calibration procedure has been performed with no cutting on the beam spot. Otherwise the calibration constants would depend on the cuts used.

Two different electron beam energies have been exploited for calibration purposes (30 GeV and 80 GeV), thus leading to two sets of calibration constants. Such constants have been used in the following analysis.

#### 4.1.3.2 *Event selection*

By observing the signal distribution of the auxiliary detectors, I applied some cuts to the event selection in order to obtain pure electron event samples. The preshower detector was installed only for the three high energy runs (80, 100 and 150 GeV), which have been found to be the most contaminated ones. In the other runs it has not been installed in order to avoid to spoil the calorimeter electromagnetic resolution, by adding an extra  $X_0$  of material in front of the calorimeter.

Figure 75 shows the ADC distributions for the auxiliary detectors for the run taken with the calibration energy of 80 GeV. By inspecting these distributions, appropriate cuts on event selection can be derived. Each of the three plots exhibits a peak at low ADC counts. This is the pedestal signal due to electronic noise and to the energy released by minimum ionizing particles. The signal after the pedestal peak represents the real particle's energy release, corresponding to the Landau distribution.

Therefore, one has to eliminate events corresponding to the signal of contaminating particles.

Appropriate cuts resulted to be:

- Muon counter < 150 ADC counts
- Tail catcher < 55 ADC counts
- Preshower > 250 ADC counts (only for high energy runs)

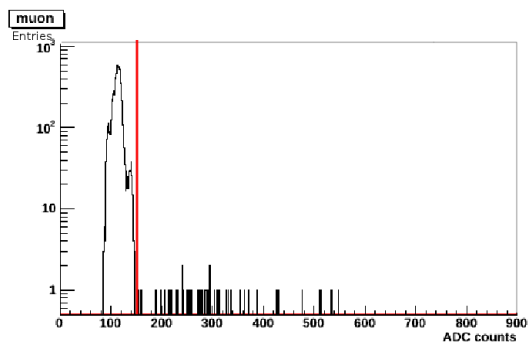
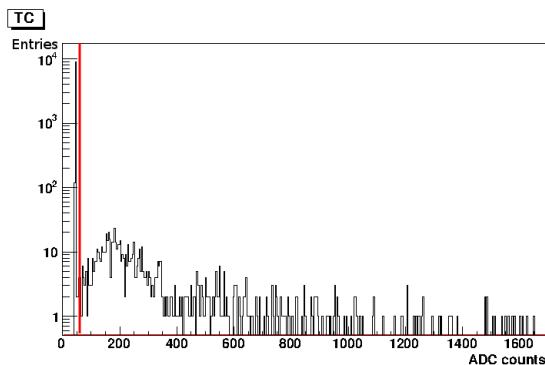
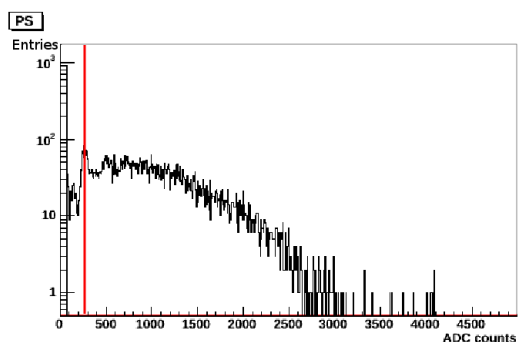
(a) *Muon counter*(b) *Tail catcher*(c) *Preshower*

Figure 75: ADC counts distribution of the muon counter, the tail catcher and the preshower detector for the 80 GeV electron beam.

The beam profile obtained from the DWC is shown in Figure 76 and it results very similar at all the energies. The beam profile has a diameter of 2 mm, corresponding to the central hole of the veto counter. In order to satisfy the event position criteria previously explained, that is the selection of events in one quadrant of the beam spot located most closely to the module center, I applied cuts on the  $x$  and  $y$  coordinates given by the DWC, as it can be seen in Figure 77.

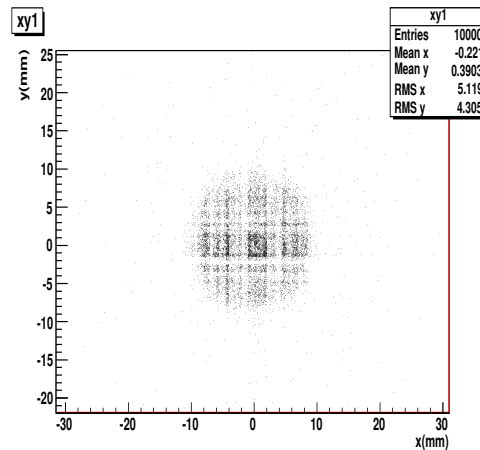


Figure 76: The beam profile obtained from  $DWC_1$ , for 30 GeV electrons.

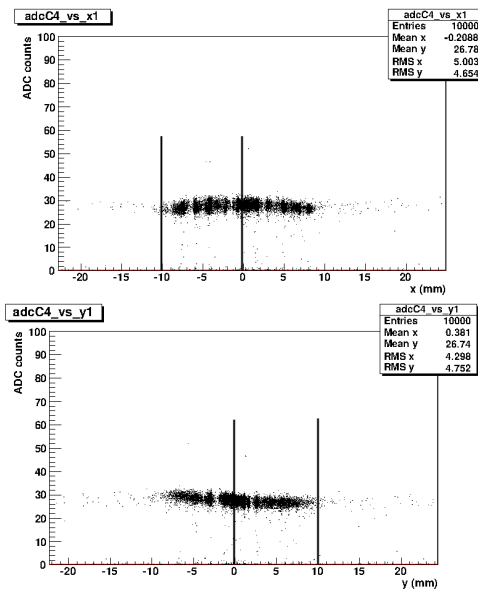


Figure 77: The scatter plot of the Cherenkov ADC counts as a function of the  $x$  and  $y$  coordinates for the electron beam run of 30 GeV. The cuts applied are marked by the solid lines. The  $DWC$   $y$  coordinate is reversed with respect to the module point of view.

#### 4.1.3.3 Energy resolution

Figure 78 and 79 shows the signal distribution of the Cherenkov and scintillation channels for all the runs considered (scan of different electron energies), after calibration and the appropriate cuts, fitted with a Gaussian. I estimated the mean  $\mu$  and the standard deviation  $\sigma$  from these fits and then derived the energy resolution  $\sigma/\mu$ .

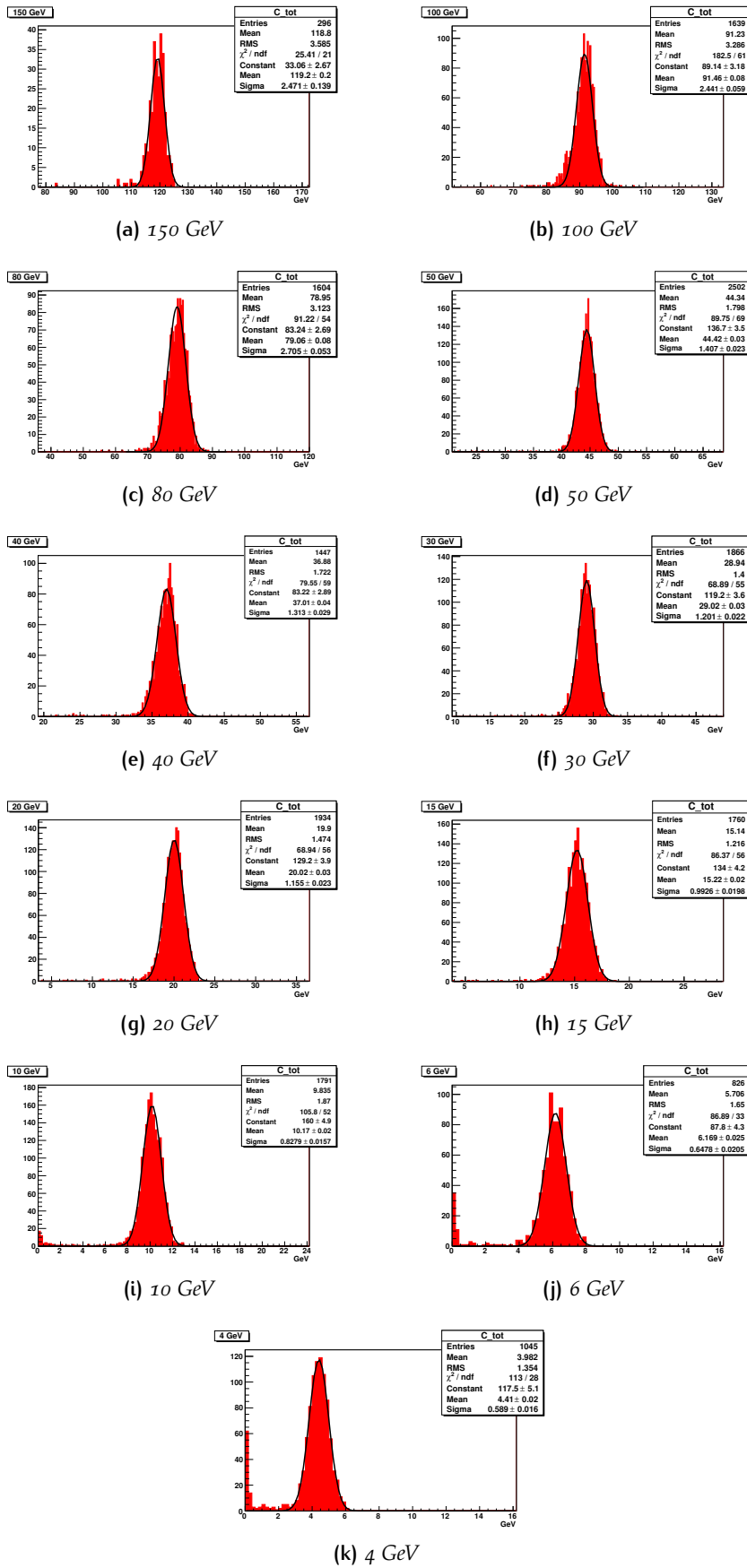


Figure 78: Signal distribution of the Cherenkov channels for each electron beam energy, fitted with a Gaussian.

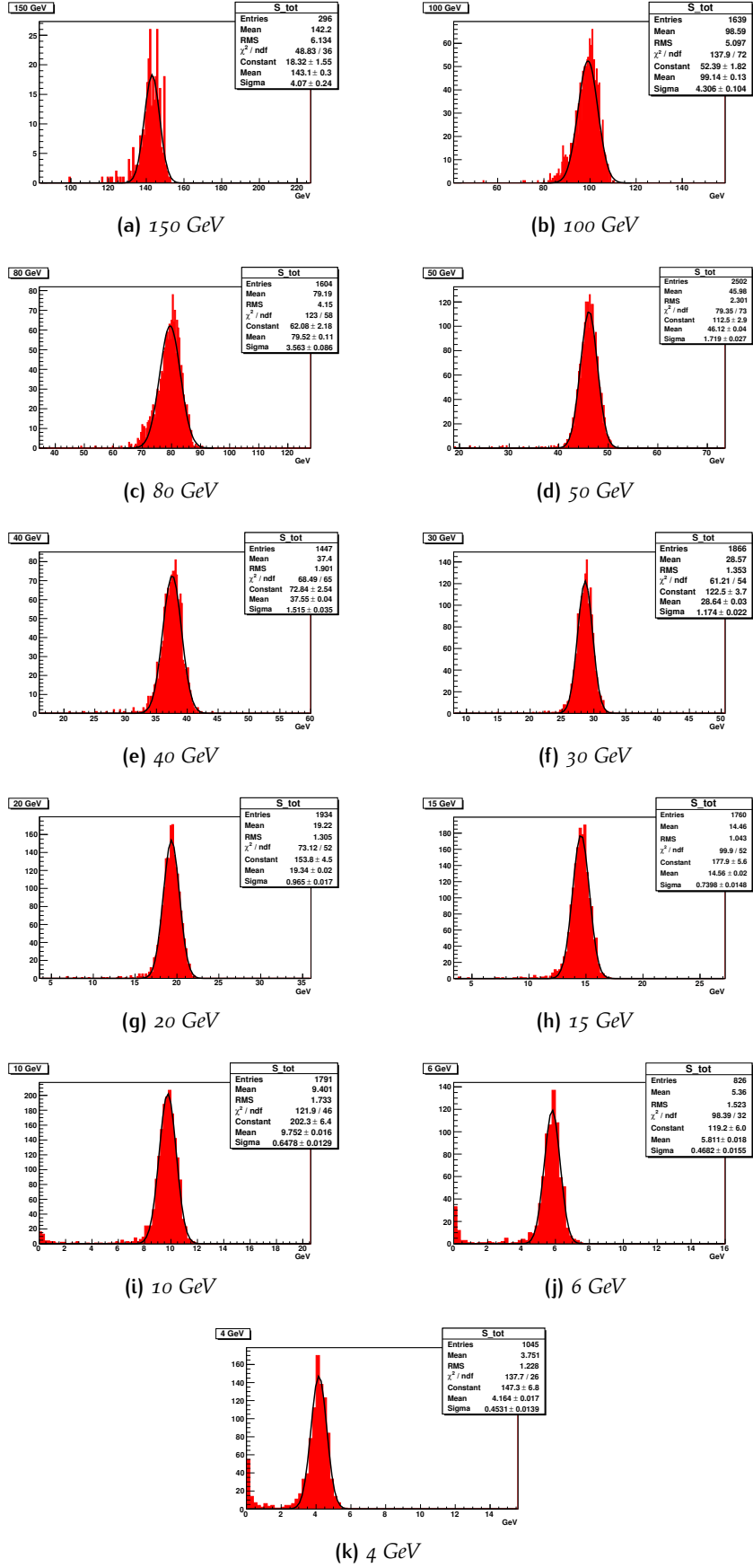


Figure 79: Signal distribution of the scintillation channels for each electron beam energy, fitted with a Gaussian.

The energy resolution for Cherenkov, scintillation and the sum of Cherenkov and scintillation channels is showed in Figure 80. I fitted the data with the usual relation  $\sigma/E = p_0 + p_1/\sqrt{E}$ , where  $E$  is the beam energy, which was explained in Chapter 1. As it can be seen from the plots, the situation is different for the two types of fibers. In the Cherenkov case (Figure 80a), the constant term results to be  $\sim 0$  and the stochastic term  $p_1$  gives an energy resolution of  $\sim 29\%$ . This poor value for the energy resolution is due to the fact that I only considered signals in Tower 4 to derive it. Such signals concern only the 85% of the total calorimeter signal, as previously said, and therefore there is a much more important contribution of leakage fluctuations to the resolution. The reason why I only considered signals in Tower 4 is that, both in the lower (4, 6 GeV) and in the higher (80, 100, 150 GeV) energy runs the resolution got worse when the sum of the four towers signals was considered. In the low energy case this was due to the presence of a non-negligible noise term, while in the high energy case to the presence of terminators (50  $\Omega$  resistors), which were applied in an attempt to reduce the PMTs noise.

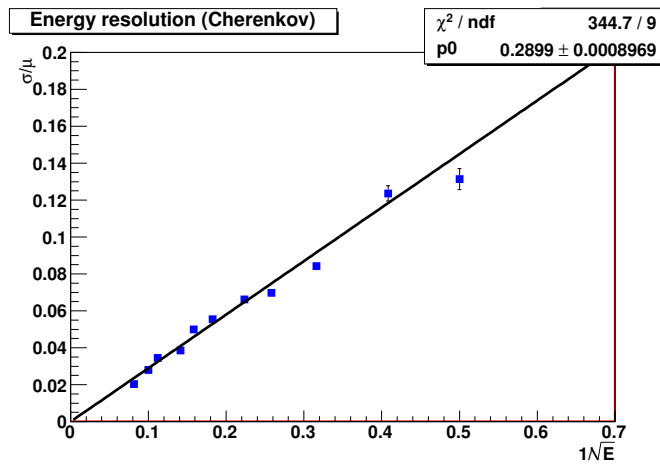
In the scintillation case, a deviation from the  $1/\sqrt{E}$  scaling is evident. In fact, as it can be seen from Figure 80b, the solid line points to a constant term of the order of 3%, which is absent in the Cherenkov data. This behaviour was already observed with the first DREAM copper module, as it was said in Section 2.2.1.1. The difference in the constant term between the two types of fibers will be investigated in the next section.

By adding the Cherenkov and scintillation signals (see Figure 80c), an improvement in the energy resolution is observed, as it was expected since the fluctuations affecting the two types of signals are almost completely independent.

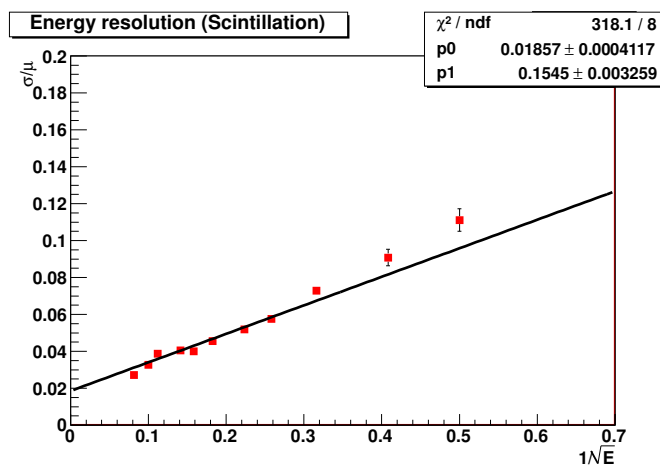
#### 4.1.3.4 Linearity

I also investigated the response linearity. Figure 81 shows the ratio  $\mu/E$  as a function of the beam energy, where  $\mu$  is the average signal detected by the PMTs, obtained from the Gaussian fit of the energy distribution at each energy.

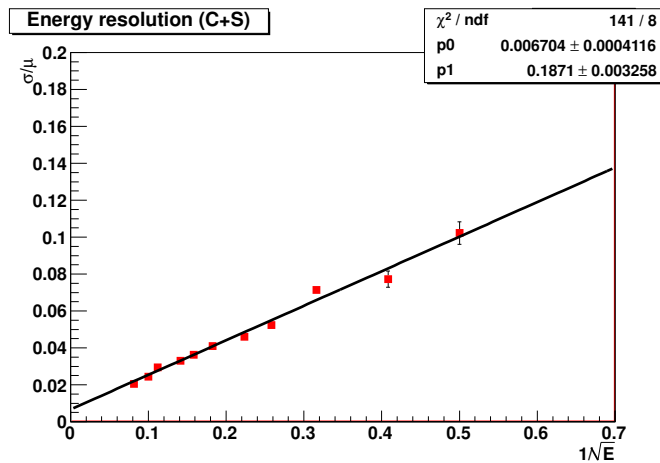
As it can be seen from the plot, there is an evidence of a deviation of the points from the value 1. This is an indication of a non-linearity of the module or readout. The reasons that led to the observed non-linearity and possible improvements in the readout in order to counteract this problem have been described in Section 3.3.1 and tested during the July 2012 testbeam. The results of this test will be given later in this chapter (Section 4.2.2.1).



(a) Cherenkov channels

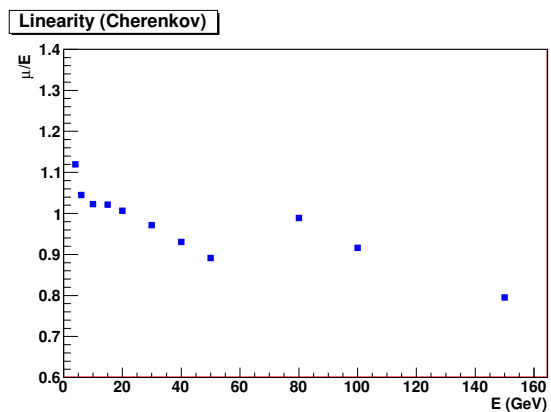


(b) Scintillation channels

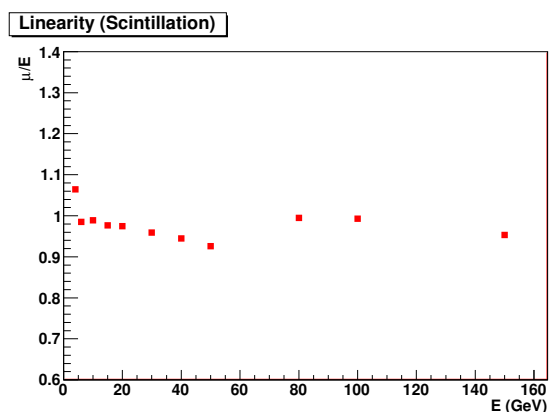


(c) The sum of Cherenkov and scintillation channels

**Figure 80:** The energy resolution for electrons entering in Tower 4 near the center of the Pavia module, as a function of  $1/\sqrt{E}$ . The three diagrams represent the results for Cherenkov (a), scintillation (b) and the sum of all fiber signals (c). The data have been fitted with the relation  $\sigma/E = p_0 + p_1/\sqrt{E}$ .



(a) Cherenkov channels



(b) Scintillation channels

Figure 81: PMTs linearity for Cherenkov (a) and scintillation (b) signals.

#### 4.1.3.5 Non-uniformity in energy resolution

The previous general analysis of the performance of the NewDREAM module gave evidence of the presence of a constant term in the energy resolution, which is considerably larger in the scintillation channel than in the Cherenkov one, as it was observed also with the first DREAM copper module (see Section 2.2.1.1). In order to explain this effect, one must say that the Cherenkov fibers are blind to the early part of the shower before the shower maximum. In fact optical fibers transmit light only if it enters at an angle smaller than the numerical aperture of the fiber. In the early part of the shower the cluster of particles is highly collimated and Cherenkov light is emitted at an angle which is bigger than the numerical aperture, being thus the fiber blind for such light. On the other hand, scintillation light is emitted isotropically and can be transmitted in the fibers. After the first stage, the shower becomes less directional and also the Cherenkov light can enter the fibers. Therefore scintillation signal varies event by event, because it is different if the incident electron produces scintillation in lead or in the fibers, giving rise to fluctuations which are absent in the Cherenkov case. In fact, after the first stage of the shower, much

more particles are present and a mixing of light has occurred.

In conclusion, scintillation signals result to be more sensitive to fiber-to-fiber response fluctuations in the detector area hit by the beam electrons, both because of the previously explained effect and because of the variation of the PMTs collection efficiency with the position of incidence on the photocathode.

In order to verify if these non-uniformities actually contribute to the constant term, I performed a study of the energy resolution in different parts of the beam spot area.

The electron runs I considered in the analysis were the same I used before, that is those at 150, 100, 80, 50, 40, 30, 15, 10, 6 and 4 GeV, with the beam centered on Tower 4.

I subdivided the beam spot, which has an area of  $20 \times 20 \text{ mm}^2$ , in 16 squares of  $5 \times 5 \text{ mm}^2$ , as showed in Figure 82, and I studied the energy resolution for all the beam spot subdivisions.

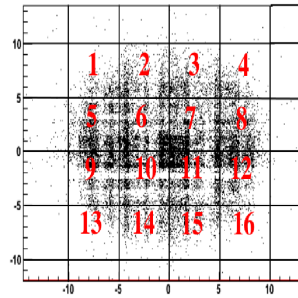


Figure 82: The beam spot suddivision.

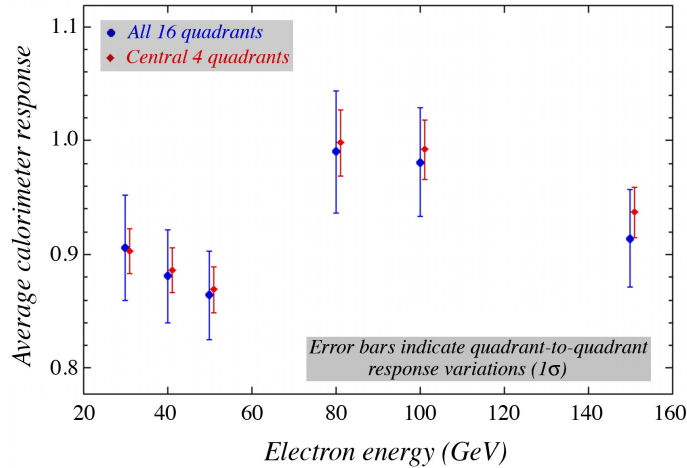


Figure 83: The average calorimeter response for all 16 quadrants (blue circles) and for the four central quadrants (red squares), as a function of the electron energy.

The results of this analysis are summarized in Figure 83 and 84. The former figure shows the calorimeter response ( $\mu$ ) averaged over all the quadrants and over the four central quadrants as a function of electron energy, while the latter one shows the response *vs.* the electron energy for all the 16 quadrants. By observing both figures one can deduce that the response differences measured across the central region of Tower 4 are indeed due to non-uniformities, since the quadrant-to-quadrant differences are very similar for all electron energies. The sigma of these response variations amounts to about 4.5% when considering all 16 quadrants, and about 2.5% if one only considers the 4 central quadrants (6,7,10,11). Therefore, these results are one more indication that the signal uniformity is not good enough in the detector modules constructed in 2011.

As a result of these observations, a study of light guides has been performed. They should be used in order to mix light coming from different fibers, that is from different parts of the calorimeter, before reaching the photocathode. The latter one, as previously explained (see Figure 73), has a more sensitive area at its center and therefore the use of light guides could help avoiding non-uniformities. The results of the test of two types of light mixers, occurred during July 2012 testbeam, will be given in the following (Section 4.2.2.1).

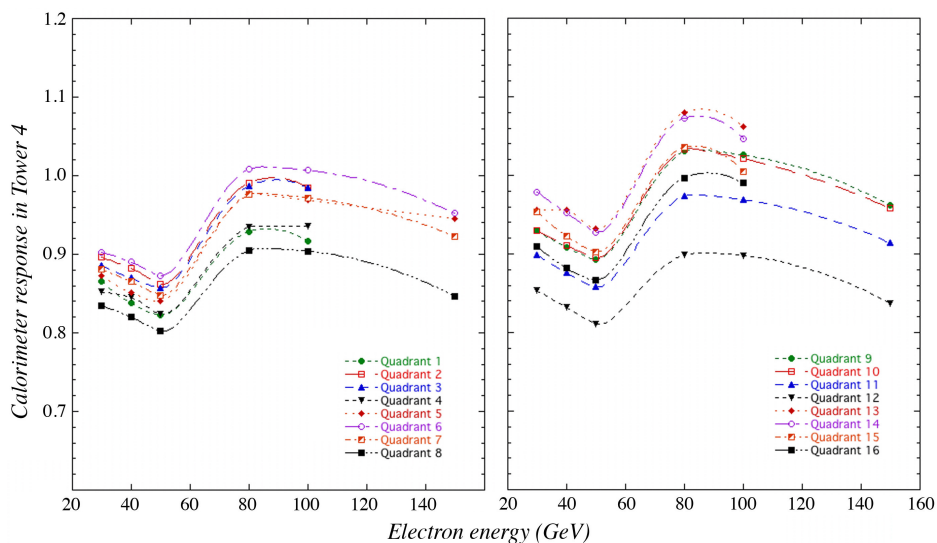


Figure 84: The calorimeter response in Tower 4 as a function of the electron energy, for all 16 quadrants.

## 4.2 JULY 2012 TESTBEAM

The NewDREAM lead/fiber module has been tested also in this occasion at the H8 beam line of SPS (see Section 4.1.1), using the same experimental setup already described in Section 4.1.2. A minor difference concerned the veto counter, which hasn't always been used during data acquisition.

### 4.2.1 Module readout

A major difference between the November 2011 and the July 2012 testbeams concerns the readout of the calorimeter module. As in the previous testbeam, two PMTs (Hamamatsu 8900) for each tower were devoted to readout the fiber signals, but in this occasion the time structure of the calorimeter signals was recorded by means of a Tektronix TDS 7254B digital oscilloscope, which provided a sampling capability of 5 GSamples/s, at an analog bandwidth of 2.5 GHz, over four input channels.

The oscilloscope was chosen after an online check of the response linearity of the module. The latter resulted to improve when the oscilloscope was used to readout the PMT signals instead of the ADC<sup>1</sup>. Therefore the readout with the oscilloscope was chosen this time for the data acquisition.

The oscilloscope has four readout channels and two different configurations have been used during the test beam. This is because one aim of the testbeam, as it was said in Section 3.3.1, was that of assessing the possibility of adding an external amplification stage to the PMTs to readout low-energy signals. Each of the PMTs used had in fact two readout channels, one with unitary gain and the other with a gain of 10.

The two configurations are summarized in the following.

- *Low energy wobbling.* This configuration was adopted for runs with electron beam energies in the range 4-50 GeV. Electrons are derived from pions with an energy of 60 GeV. All four oscilloscope channels were used, two of them devoted to the readout of the low-gain PMT channels (one Cherenkov and one scintillation) and the other two devoted to the readout of the high-gain PMT channels.
- *High energy wobbling.* This configuration was adopted for runs with electron beam energies in the range 20-150 GeV. Electrons

<sup>1</sup> The readout with the oscilloscope, which has only 4 readout channels, can not be used during the November 2012 testbeam, when the 3x3 matrix of lead modules will be tested and 72 PMTs channels should be readout. For this reason, the problem with the ADCs is being investigated, in order to have them available for the next testbeam.

are derived from pions with an energy of 180 GeV. Only two oscilloscope channels were used this time (one Cherenkov and one scintillation), since the high gain PMT channels weren't considered in this case.

All the photomultiplier tubes used for the data acquisition were individually tested before the starting of the testbeam and the 8 PMTs which exhibited the most uniform response were chosen.

Data were acquired by sending electron and pion beams of different energies in the center of Tower 3 or in the center of the calorimeter module. In the latter case, the signals readout by the PMTs, whose gains were previously equalized looking at the online response, were sent into an adder before being readout by the oscilloscope.

The detector was calibrated using a run taken with 10 GeV electron beam for the low energy configuration or with 80 GeV electron beam for the high energy configuration and imposing that the 93% (85%) of the energy was contained in the module, for runs with the beam sent in the center of the module (in the center of Tower 3).

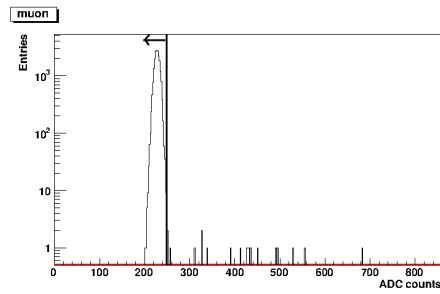
#### 4.2.2 Data analysis

As final part of my thesis work within the DREAM Collaboration, I contributed to the analysis of data taken during July 2012 testbeam. In my analysis I focused on three main topics, which are listed in the following.

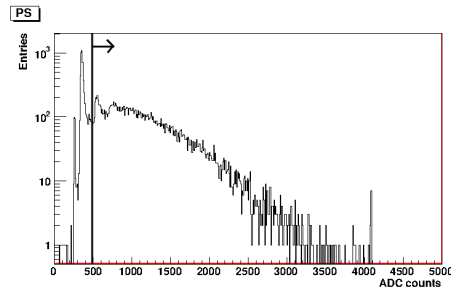
- The study of response linearity using different PMT bases and light mixers, which have been tested in this occasion.
- The study of response uniformity over the module surface.
- A comparative analysis of data taken with different PMT gains.

The event selection criteria I applied in my analysis are the same already explained in Section 4.1.3.2. Figure 85 shows the cuts I applied on the muon counter and the preshower detector.

Figure 86 shows the shapes of the average oscilloscope signals for Cherenkov and scintillation light, obtained by means of both the low and the high gain PMTs channels. In order to get the analogue of the ADC distributions, the pulse shape of the signals have been integrated event-by-event, by choosing a suitable integration gate containing the peak of the pulse shape. Figure 87 shows the integral distributions of Cherenkov and scintillation signals for the run taken at 10 GeV with the beam sent in the center of the calorimeter module.



(a) Muon counter



(b) Preshower detector

Figure 85: ADC distribution of the muon counter (a) and the preshower detector (b) for the run at 10 GeV.

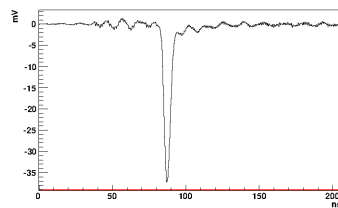
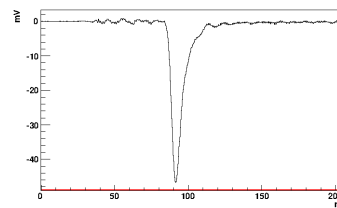
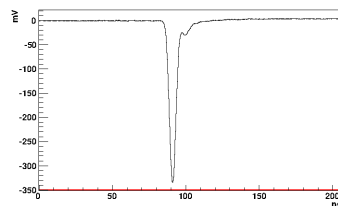
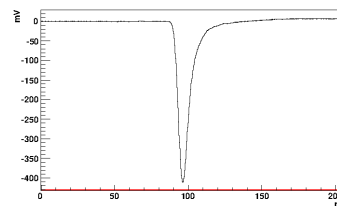
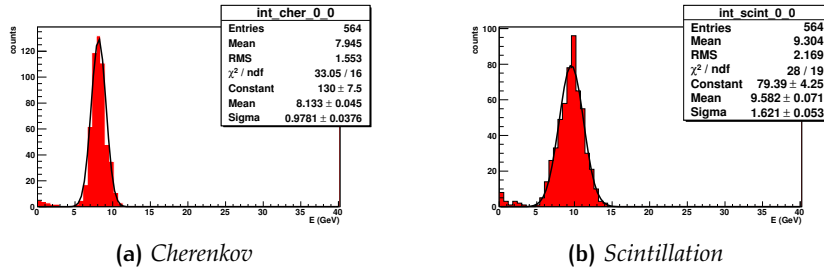
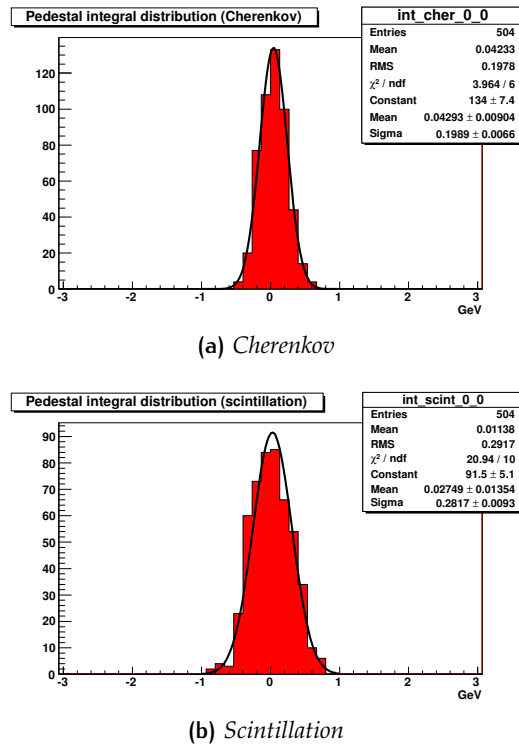
(a) Cherenkov,  $G=1$ (b) Scintillation,  $G=1$ (c) Cherenkov,  $G=10$ (d) Scintillation,  $G=10$ 

Figure 86: Average pulse shapes of the oscilloscope signals obtained with a 10 GeV electron beam sent in the center of the calorimeter module. Shown are the pulse shapes of Cherenkov and scintillation signals readout by the low gain PMT channels ((a) and (b)) and by the high gain PMT channels ((c) and (d)). One may notice that the signal amplitudes for the high gain channels are 10 times those for the low gain channels.



**Figure 87:** Integral distributions of Cherenkov and scintillation signals obtained with a 10 GeV electron beam sent in the center of the calorimeter module for signals readout by the low gain PMT channels, after the calibration.

In order to subtract the effects of electronic noise, which are more crucial at low energies, I evaluated the standard deviation of the integral distribution for the pedestal run taken at the lowest energy (4 GeV). The Gaussian fit of this distribution is shown in Figure 88, both for Cherenkov and scintillation signals. I finally subtracted in quadrature the values of the standard deviation obtained with this fits from those obtained with the fits of the data distributions for all the energies.



**Figure 88:** Integral distributions of Cherenkov and scintillation pedestal channels obtained with a 4 GeV electron beam sent in the center of the calorimeter module.

The results I obtained for each of the previous topics will now be described.

#### 4.2.2.1 *Test of different PMT bases and light mixers*

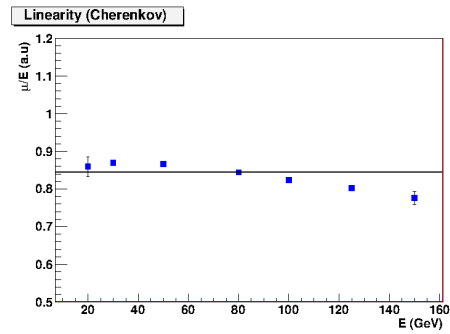
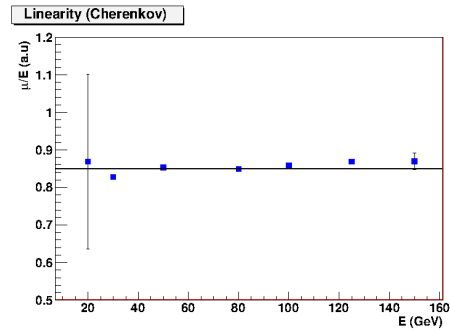
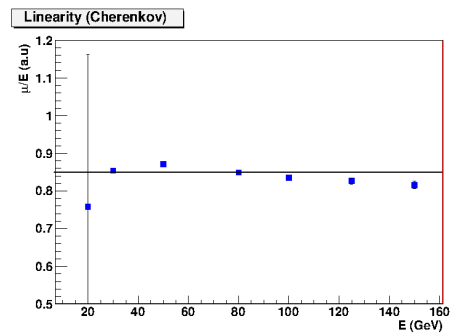
As it was remarked at the end of the previous chapter (see Section 3.3.1), during the July 2012 testbeam some new ideas aimed to optimize the signal readout have been put under test.

The calorimeter performance has been studied using three different PMTs bases, which have been produced by the INFN Pavia electronic workshop:

- the standard Hamamatsu base;
- the so called "tapered" base, *i.e.* the Hamamatsu base with an additional voltage divider aimed to lower the gain of the PMT;
- the tapered base added of an additional removable voltage generator to the last dynode, in order to reduce space charge effects.

Each of the three types of bases has been coupled to the same PMT, in order to better compare the base behaviour, and used to readout the module signal. Each time an energy scan with electron beams of energies ranging from 20 to 150 GeV has been performed. The beams were centered in Tower 3 and the linearity of the response has been measured for all the three different configurations. The results of this test are shown in Figure 89.

As it can be seen from the figure, the configuration with the simple tapered bases resulted the one producing the best linearity. Therefore the tapered bases have been chosen to be used in the following tests of the NewDREAM lead/fibers module and they will be used in the central tower of the 3x3 matrix of lead modules, which will be tested during November 2012. This improvement in linearity represents a very encouraging result, since a considerable response non-linearity was pointed out by the analysis of November 2011 data (see Section 4.1.3.4). The use of tapered bases seems to improve greatly the situation and therefore one may conclude that the previously observed non-linearity was a consequence of problems with the readout, and not with the calorimeter itself, which results instead to be very linear.

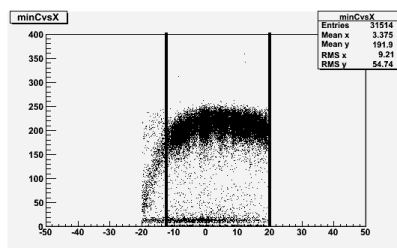
(a) *Standard bases*(b) *Tapered bases*(c) *Tapered bases with independent dynode*

**Figure 89:** Response linearity for Cherenkov signals detected with PMTs equipped with standard bases (a), tapered bases (b) and tapered bases with an independent voltage generator on the last dynode (c). The big error bars for the points at 20 GeV in (b) and (c) are owed to the very low statistics at that energy.

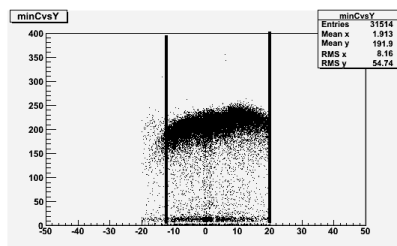
A configuration in which light mixers were added between the fibers and the PMTs has also been tested, in order to verify if light mixing before the readout could actually help in reducing effects of non-uniformities, as resulted from the analysis of November data (see Section 4.1.3.5). Two types of light mixers, 2 cm and 4 cm thick respectively, have been used.

In order to evaluate the effectiveness of this configuration, I analyzed data taken with a 80 GeV electron beam sent in the center of Tower 3, after selecting events by means of cuts on the auxiliary detectors and the DWCs. In particular, I selected an area of the beam spot

after inspecting the plots representing the distribution of the minimum of the signal time structures event-by-event as a function of the x and y coordinates of  $DWC_1$ , as it is shown in Figure 90 (the veto counter wasn't used for this run, as it can be seen from the figure).



(a) Peak vs. x



(b) Peak vs. y

**Figure 90:** Scatter plots representing the distribution of the minimum of the Cherenkov signal time structures event-by-event as a function of the x (a) and y (b) coordinates of  $DWC_1$ .

Then, I divided this area in 9 parts, as it can be seen in Figure 91, and for each part I evaluated the mean value of the integral distribution.

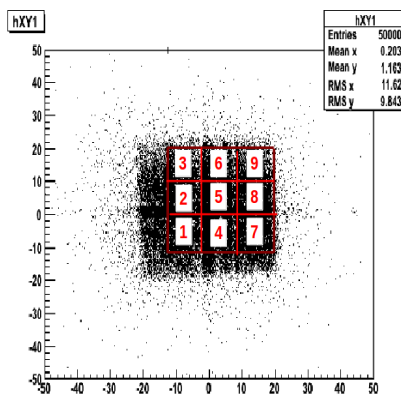
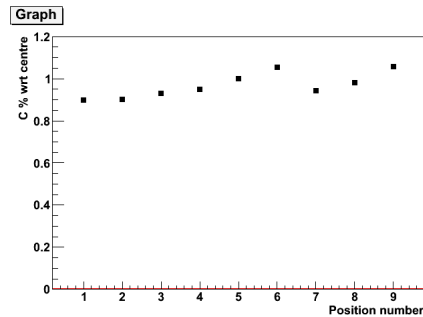


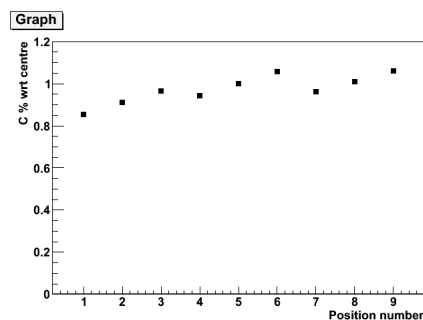
**Figure 91:** Subdivision of the selected area of the beam spot.

This values, normalized to the response in the central area, are shown in Figure 92 as a function of the number the divisions, *i.e.* the one without any light mixers

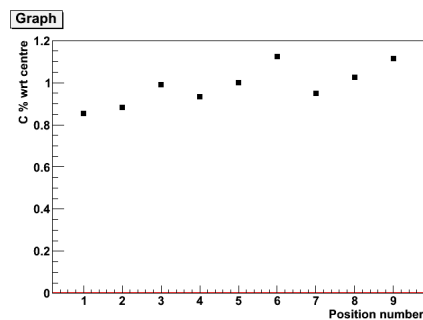
(Figure 92a), the one with the 2 cm mixers (Figure 92b) and the one with the 4 cm mixer (Figure 92c). As it can be seen from the figure, no significant improvements are observed by the comparison of the three plots. This may be owed to the fact that we used the eight PMTs with the most uniform response. Besides, the optical coupling between the fibers and the PMTs changed for each measurement, thus not allowing a good comparison between the different responses. The idea of using light mixers in the readout was therefore discarded in the end.



(a) No mixers



(b) 2 cm mixer



(c) 4 cm mixer

Figure 92: Mean values of the response as a function of the number of the corresponding subdivided area. Results for three readout configurations: without light mixers (a), with 2 cm (b) and 4 cm thick light mixers(c).

#### 4.2.2.2 Study of response uniformity over the module surface

A preliminary analysis I carried on data taken with the beam sent in the center of the calorimeter module and the low energy wobbling revealed poor values of the energy resolution both for the Cherenkov and the scintillation signals. A plausible explanation of this bad behaviour has been found to be the possible incorrect equalization of the response of the four towers. The latter was done online during the testbeam by sending the beam in the center of each of the four towers and choosing the proper high voltage values for the PMTs, before sending their signals to the adder. Unfortunately, with this method, a more careful offline equalization cannot be done anymore.

In order to investigate this hypothesis, I re-analyzed the same runs (which are summarized in Table 4), after selecting four areas in the corners of the beam spot by means of cuts on  $DWC_1$ , as shown in Figure 93. These areas have been selected since they are representative of the signals in single towers, being them far from the 4-corners region.

**Table 4:** Electron beam energies and statistics of the runs used in the analysis, taken with the beam sent in the center of the calorimeter module.

Energy (GeV)	N <sup>o</sup> of events
4	~5000
6	20000
8	20000
10	20000
15	20000
20	20000
30	20000
40	20000
50	20000

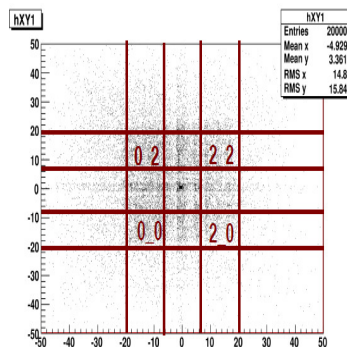


**Figure 93:** The four areas selected by means of  $DWC_1$ .

The results of this analysis strengthened the hypothesis of the incorrect online equalization. In fact, I obtained the gaussian fits of the integral distributions in each of the four areas and their comparison showed big differences in the average responses depending on the impact point of the beam. Table 5 and Figure 94 summarize the mean scintillation signals for the regions 0-2 and 2-2, *i.e.* for a shift of 2 cm of the impact point. It can be seen that going from region 0-2 to 2-2, the mean 50 GeV scintillation signal varies from 41.75 to 65.39, which corresponds to an increase by more than 50%.

**Table 5:** Comparison between mean scintillation signals in areas 0-2 and 2-2, corresponding to a shift of 2 cm of the impact point of the beam.

Energy (GeV)	Mean S, region 0-2 (GeV)	Mean S, region 2-2 (GeV)
4	3.488	4.537
6	4.972	7.019
8	6.533	9.532
10	8.212	12.22
15	12.5	19.05
20	16.57	25.4
30	25.48	38.86
40	32.75	51.62
50	41.75	65.39

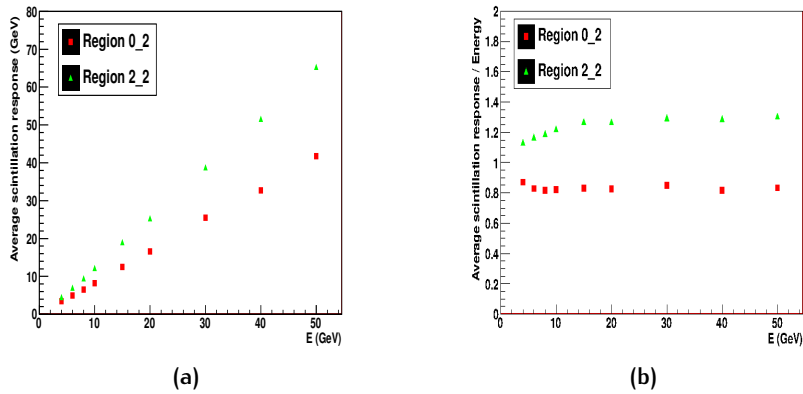


**Figure 94:** The mean scintillation signals (a) and the same signals normalized to the beam energy (b) for regions 0-2 and 2-2 as a function of the beam energy.

In order to get a more detailed picture of the response variations over the surface of the calorimeter module, I analyzed the data from a matrix scan of the lead module. In these measurements, a beam of 20 GeV electrons was steered to 9 different points on the module surface,

with these points spaced by 20 mm. I applied cuts on both the DWC chambers, by subdividing the beam spot into a  $4 \times 4$  grid, each area measuring  $5 \times 5 \text{ mm}^2$ . In this way, I could measure the response of the total calorimeter module in  $9 \times 16 = 144$  different points. Figure 95 gives the contour plots of the response, for Cherenkov and scintillation signals, over the total surface of the lead module. The colour scale represents the values of the average response over this surface. It can be seen from the figure that in some towers (e.g. Tower 2 and 3 in the scintillation case) the high voltage value was chosen too high during the online equalization.

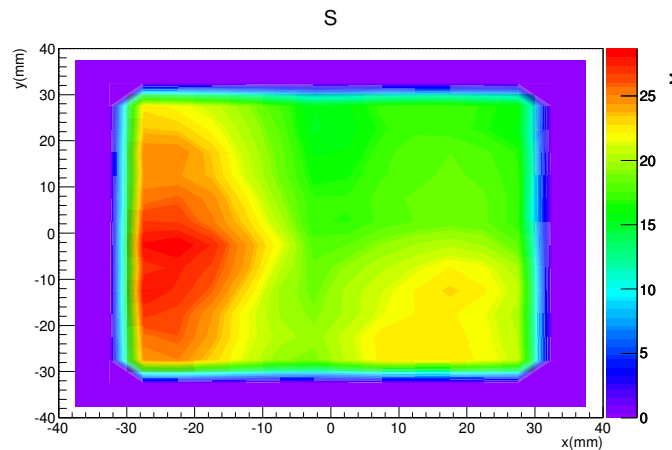
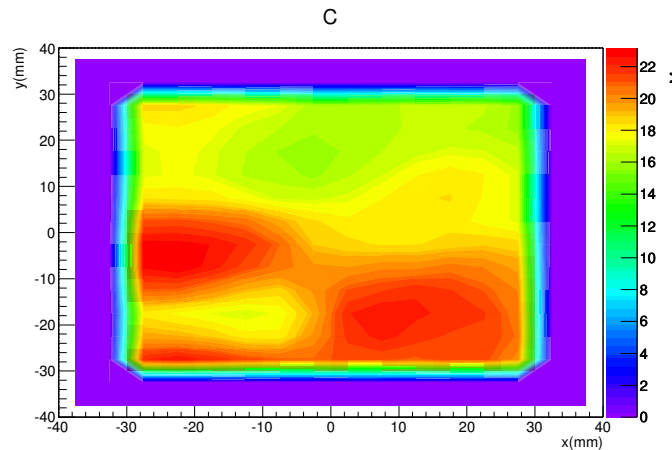


**Figure 95:** Contour plots of the average response over the total surface of the NewDREAM lead/fibers module for the Cherenkov (a) and scintillation (b) channels. The colour scale represents the values of the average response.

#### 4.2.2.3 Comparison between $G=1$ and $G=10$

The last topic I considered in my analysis of July 2012 data concerns the comparison between the performance of the module obtained using two different gains of the PMTs. An additional readout channel with a gain of 10 was in fact considered, besides the channel with  $G=1$ , in an attempt of improving the separation of low energy signals from noise (see Section 3.3.1). A scheme of the electronic board which splits the PMT signal (IN) in a  $G=1$  (OUT 1) and a  $G=10$  (OUT 2) signals is shown in Figure 96. The two output signals are then readout by the oscilloscope.

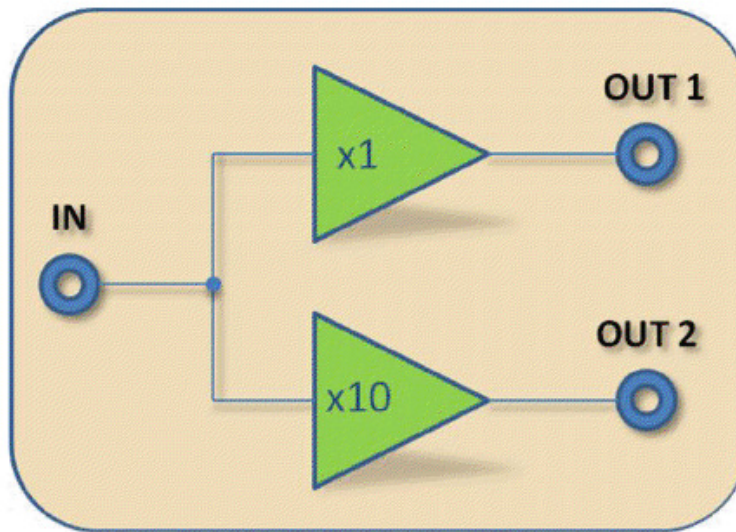


Figure 96: A scheme of the electronic board with the amplifier applied to the readout chain of the PMT.

For this analysis I considered again the runs with the beam sent in the center of the modules with the energies listed in Table 4. I applied cuts on both the two DWCs in order to select a region of the beam spot corresponding to region 2-2 of Figure 93. I chose this region since from the previous analysis it resulted to be the one with the higher statistics and in order to minimize the shower leakage. In fact, this region is the one which minimizes the shower leakage, owing to the fact that we have the calorimeter at an angle with respect to the beam.

Besides comparing the results obtained with different gains, I also compared those obtained using two different integration gates. Figure 97 shows the average time structure of the scintillation signal readout by the  $G=10$  channel. The presence of an overshoot after the peak, due to the presence of a capacitor inserted in the amplifying cir-

cuit, is highlighted in the figure and its effect has to be investigated, in view of coming back to the use of ADCs in the readout of the next testbeam. The latter ones, in fact, are characterized by a fixed integration gate, which we choose large enough to include the effect of the overshoot. I therefore analyzed the data separately using two different integration gates, *i.e.* two different intervals of nanoseconds containing the peak of the signal:

- a *narrow* gate of 13 ns for the Cherenkov signals and 22 ns for the scintillation signals;
- a *broad* gate of 80 ns for both the Cherenkov and scintillation signals.

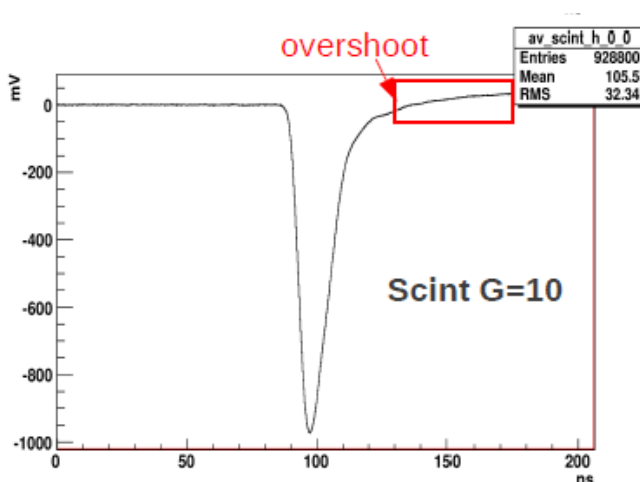
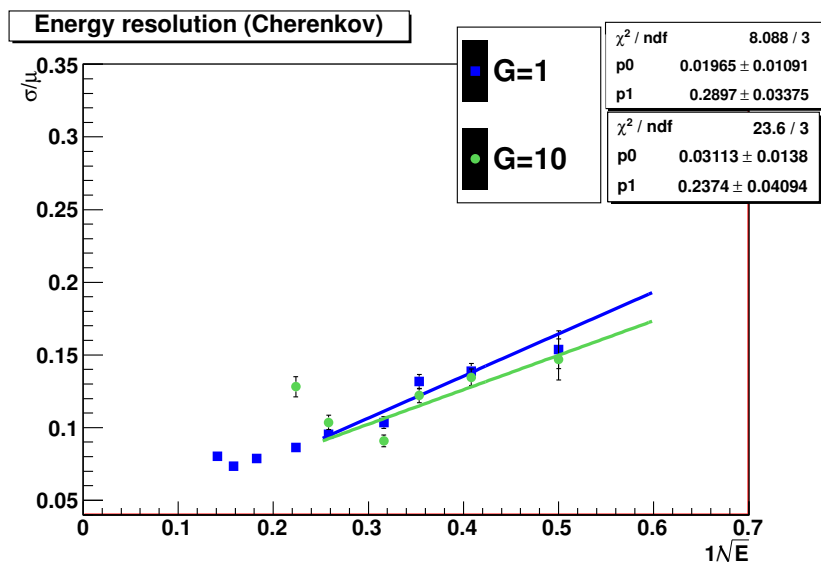


**Figure 97:** The average pulse shape of a scintillation signal readout by the G=10 channel. The presence of an overshoot after the signal peak is highlighted.

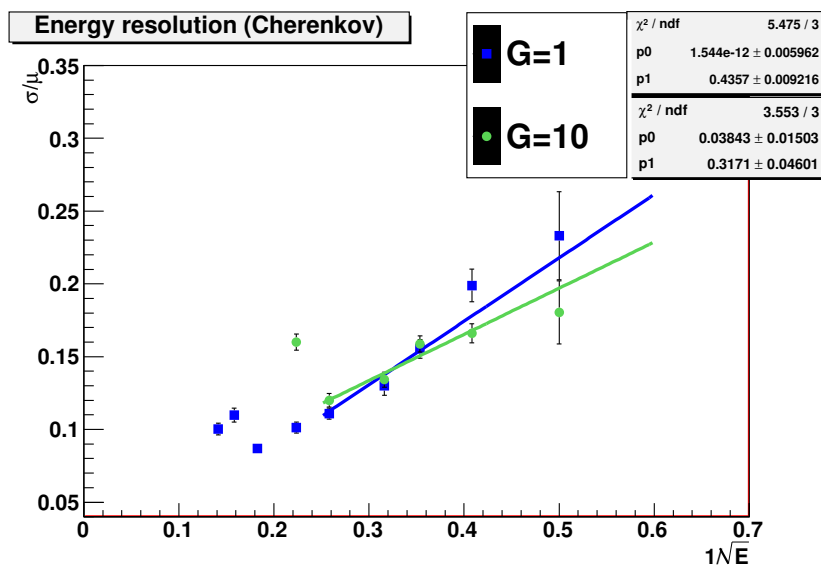
Figure 98 and 99 show the energy resolution as a function of  $1/\sqrt{E}$  for the Cherenkov and scintillation channels. In each of the plots shown in the figure, both the data obtained with the G=1 and G=10 channels are represented. Figure 98a and 98b show the comparison between the Cherenkov energy resolution obtained by integrating the signals over the narrow and the broad gate, respectively. Figure 99a and 99b show the same for scintillation. Only the data points corresponding to energies ranging from 4 to 15 GeV have been fitted with the relation  $\sigma/E = p_0 + p_1/\sqrt{E}$ , since at higher energies saturation effects for the G=10 readout started to occur. The poor values of energy resolution found in this analysis can be again a consequence of the incorrect online equalization which has been carried during the testbeam, before data acquisition.

Finally, Figure 100 and 101 show the same comparisons for the linearity. The drop of linearity which can be observed in this figure for

the high gain points towards higher energies is due to the saturation of the amplifier with increasing energies.

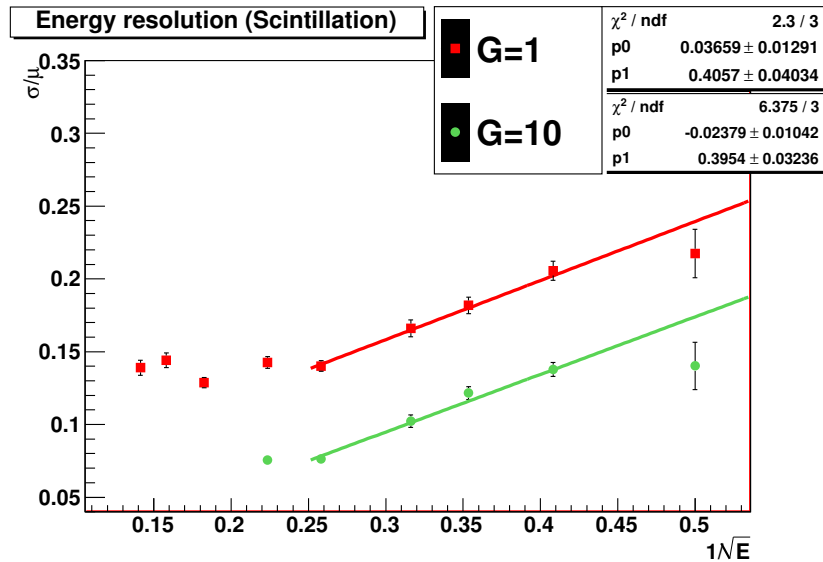


(a) Cherenkov, narrow gate

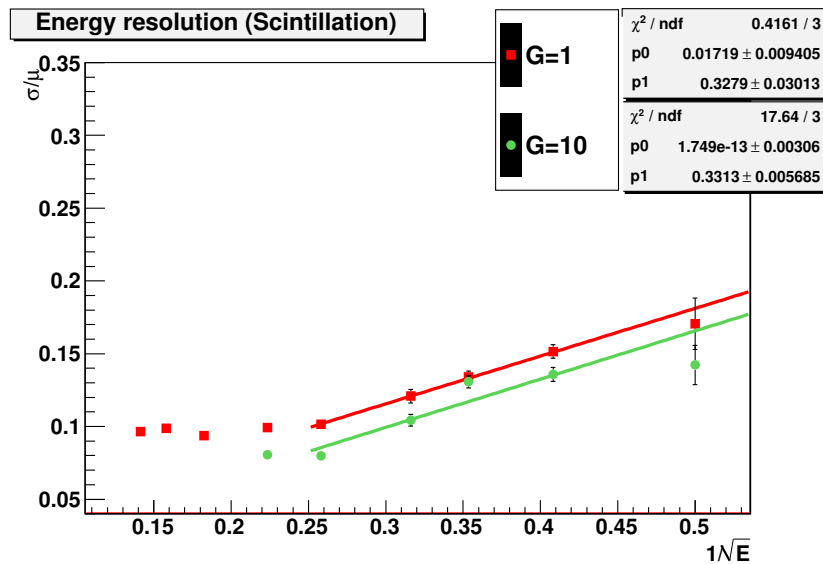


(b) Cherenkov, broad gate

**Figure 98:** Energy resolution for the Cherenkov channels, obtained by integrating the signals over two different ns gates. Data points from 4 to 15 GeV have been fitted with the relation  $\sigma/E = p_0 + p_1/\sqrt{E}$ . Data from G=1 and G=10 channels are plotted.



(a) Scintillation, narrow gate



(b) Scintillation, broad gate

Figure 99: Energy resolution for the scintillations channels, obtained by integrating the signals over two different ns gates. Data points from 4 to 15 GeV have been fitted with the relation  $\sigma/E = p_0 + p_1/\sqrt{E}$ . Data from G=1 and G=10 channels are plotted.

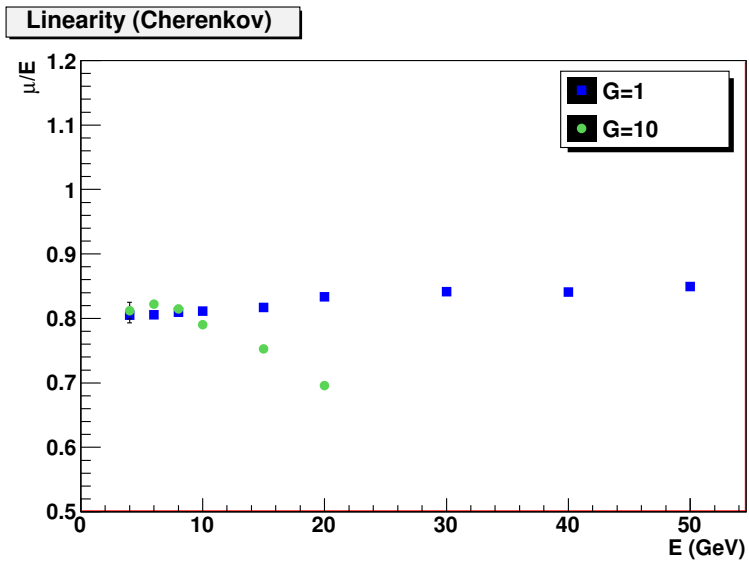
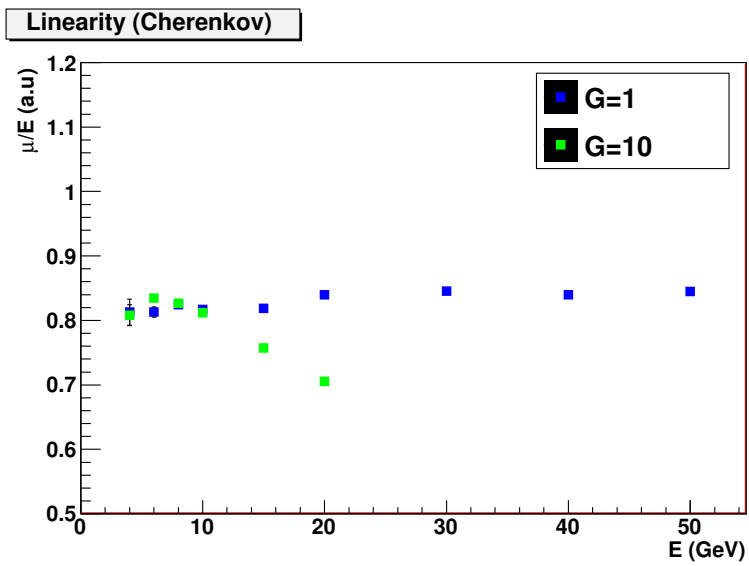
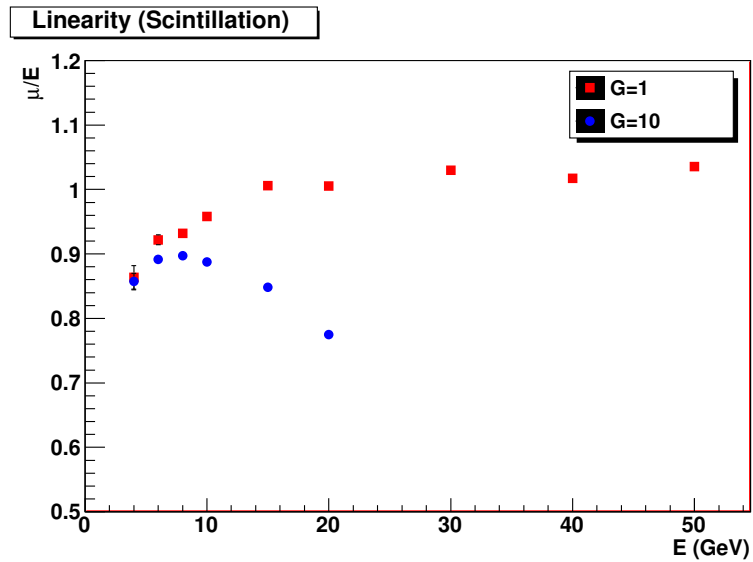
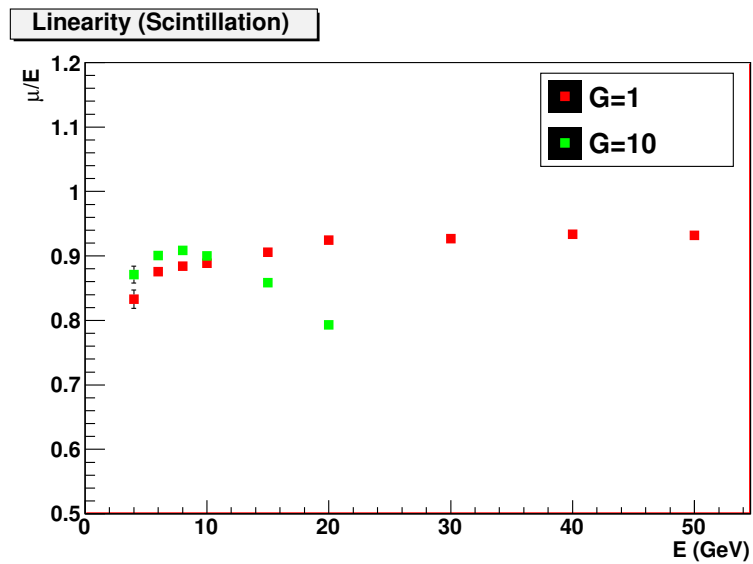
(a) *Cherenkov, narrow gate*(b) *Cherenkov, broad gate*

Figure 100: Response linearity for the Cherenkov channels, obtained by integrating the signals over two different ns gates. Data from G=1 and G=10 channels are plotted.



(a) Scintillation, narrow gate



(b) Scintillation, broad gate

Figure 101: Response linearity for the scintillations channels, obtained by integrating the signals over two different ns gates. Data from G=1 and G=10 channels are plotted.

# 5 | CONCLUSIONS

Thanks to the development of more refined technologies, the energies reached in particle physics experiments have become increasingly higher in the last decades. At the same time, the role played by calorimeters in experiments has progressively grown in importance and, nowadays, calorimetry represents an essential component in almost all high energy physics facilities.

Calorimeters provide crucial information for particle detection and identification but, in the case of hadronic calorimeters, the precision of their measurements is limited by some peculiar effects.

There are several R&D projects devoted to the study and the implementation of possible improvements to the current limits of hadronic calorimetry. One of them, the DREAM Project (or CERN R&D 52 Experiment), has been the R&D activity in which I did my thesis work.

For about ten years, the DREAM Collaboration has been exploring the potential of the dual-readout method, *i.e.* the simultaneous detection of Cherenkov and scintillation light produced by energetic particles passing through an amount of material, finalized to the event-by-event measurement of the electromagnetic shower fraction in hadronic showers. The knowledge of this fraction allows to correct the calorimeter signals for the effects of non-compensation and thus to obtain better energy resolution and response linearity.

The DREAM Collaboration focused initially on the construction and test of a prototype of sampling calorimeter made of copper and optical fibers as passive and active media, respectively. The encouraging results obtained from this first instrument led the Collaboration to investigate the possibility of using homogeneous crystals for dual-readout purposes. In parallel with an intensive study of various types of crystals, the fiber option has been pursued and a prototype of fiber calorimeter with lead as absorber medium has been built in Pavia during the spring of 2011.

In my thesis I present the results of the analysis of data taken with the NewDREAM lead/fibers module during two periods of data acquisition at testbeams, namely in October/November 2011 and in July 2012. Both tests were performed at the H8 beamline at CERN SPS and in the later one I also contributed actively to the data taking.

In the first part of my analysis I mainly focused the attention on the study of the general performance of the calorimeter module, using data taken during the November 2011 testbeam. This analysis highlighted the presence of a strong non-linearity and spatial non-uniformity in the signal response, whose origins have been investi-

gated in order to conjecture possible improvements in the readout electronics.

These improvements, such as new PMTs bases and the use of light mixers to couple the fibers with the PMTs, have been tested during the July 2012 testbeam. The second part of my analysis has been therefore devoted to the study of the new readout configurations. My results allowed to understand which of the different solutions gave the best performance. In particular, one type of PMTs bases resulted to produce the best linearity and was therefore chosen to be used in the next testbeam, which will occur in November 2012. In this occasion nine lead/fibers modules, that have been built with my active participation during 2012 in Pavia, will be arranged to form a  $3 \times 3$  matrix and tested at CERN SPS. The matrix will represent part of a full containment hadronic fiber calorimeter, which is the main goal of the DREAM Project.

In my analysis I also focused on the investigation of some non-uniformities in the signal response over the module surface, which were the effects of an incorrect online procedure of equalization of the response of different readout channels. This analysis emphasized the need of a more careful offline procedure and therefore more attention will be given to this point in the next testbeam.

A chapter of my thesis has to do with the illustration of the procedure that we adopted to build the new modules. Some pictures of the various construction stages and details about the chosen materials are presented in this section.

As a final remark, it is worth to point out that the dual-readout technique is being taken into serious account in view of future collider experiments, owing to its demonstrated effectiveness and its eligibility for high-quality calorimetric measurements.

## RINGRAZIAMENTI

La conclusione della mia tesi di laurea magistrale rappresenta, al di là di un mero traguardo universitario, la chiusura di un capitolo della mia vita, un capitolo intenso ma ricco di gioie e soddisfazioni e che ricorderò per sempre con grande affetto.

Ci sono alcune persone, che ora cercherò di ringraziare singolarmente, a cui devo la mia più sincera gratitudine, poiché hanno avuto un ruolo di fondamentale importanza nella mia crescita sia culturale che umana.

Ringrazio innanzitutto il mio relatore, Prof. Michele Livan, il quale mi ha guidata con grande disponibilità e gentilezza nel mio lavoro e mi ha dato la possibilità di fare il mio timido ingresso nell'affascinante mondo della ricerca nel settore della fisica delle particelle.

Desidero esprimere la mia più sincera gratitudine alla mia correlatrice, Dott.ssa Silvia Franchino, che mi ha seguito con grande pazienza e dedizione, ha corretto la mia tesi con estrema attenzione e mi ha offerto tutto il suo sostegno e la sua amicizia.

Un grande ringraziamento va alla Dott.ssa Gabriella Gaudio per avermi messo a disposizione i suoi consigli e la sua esperienza.

Ringrazio sentitamente tutti i membri della Collaborazione DREAM, con i quali ho avuto il piacere di interagire durante il testbeam e che sono stati estremamente gentili e disponibili nei miei confronti.

Un grazie di cuore ad Angelo, Filippo e Claudio dello staff tecnico dell'INFN di Pavia, per i loro consigli, il loro supporto e per le piacevoli ore trascorse in capannone.

Grazie a tutti i miei "colleghi" che hanno condiviso con me le ansie e le gioie di questi anni universitari e in particolare grazie a Daniele, Davide e Michele.

Grazie a Marta e Ylenia, la vostra amicizia e il vostro sostegno sono stati (e sono) fondamentali per me.

Grazie ai miei amati nonni, perchè il vostro dolce ricordo mi accompagnerà per sempre e mi sarà sempre di conforto.

Grazie alla nonna Assunta, alla zia Linda e allo zio Davide per tutto l'amore che mi date.

Infine, ultimi per ordine ma primi per importanza, grazie a mamma e papà. Niente di tutto ciò sarebbe stato possibile senza il vostro supporto e il vostro amore ed è a voi che dedico questo lavoro.



## BIBLIOGRAPHY

- [1] R. Wigmans, *Calorimetry. Energy measurement in particle physics*, Oxford University Press (2000)
- [2] W. R. Leo, *Techniques for nuclear and particle physics experiments*, Springer-Verlag (1993)
- [3] T. A. Gabriel et al., *Nucl. Instr. and Meth.*, A(338):336 (1994)
- [4] D. Acosta et al., *Nucl. Instr. and Meth.*, A(316):184 (1992)
- [5] G. Gaudio M. Livan and R. Wigmans, *The Art of Calorimetry, Proceedings of the International School of Physics "Enrico Fermi", Course CLXXV "Radiation and Particle Detectors"*, edited by S. Bertolucci, U. Bottigli, P. Oliva (2006)
- [6] D. Green, *Proc. 4th Int. Conf. on Calorimetry in High Energy Physics*, La Biodola, Italy, eds. A. Menzione and A. Scribano, (Singapore: World Scientific) (1994)
- [7] L. Bartoszek et al., *Nucl. Instr. and Meth.*, A(301):47 (1990)
- [8] R. Wigmans, *Nucl. Instr. and Meth.*, A(259):389 (1987)
- [9] D. Acosta et al., *Nucl. Instr. and Meth.*, A(320):128 (1992)
- [10] Y. Galaktionov et al., *Nucl. Instr. and Meth.*, A(251):258 (1986)
- [11] D. Acosta et al., *Nucl. Instr. and Meth.*, A(302):36 (1991)
- [12] V. Nagaslaev et al., *Nucl. Instr. and Meth.*, A(462):411 (2000)
- [13] N. Akchurin et al., *Nucl. Instr. and Meth.*, A(533):305 (2004)
- [14] N. Akchurin et al., *Nucl. Instr. and Meth.*, A(536):29 (2005)
- [15] N. Akchurin et al., *Nucl. Instr. and Meth.*, A(537):537 (2005)
- [16] N. Akchurin et al., *Nucl. Instr. and Meth.*, A(593):530 (2008)
- [17] N. Akchurin et al., *Nucl. Instr. and Meth.*, A(595):359 (2008)
- [18] N. Akchurin et al., *Nucl. Instr. and Meth.*, A(604):512 (2009)
- [19] N. Akchurin et al., *Nucl. Instr. and Meth.*, A(610):488 (2009)
- [20] D. Gingrich et al., *Nucl. Instr. and Meth.*, A(364):290 (1995)
- [21] N. Akchurin et al., *Nucl. Instr. and Meth.*, A(399):202 (1997)

- [22] Livan, M., Vercesi, V. and Wigmans, R. (1995). Scintillating-fiber Calorimetry, *CERN Yellow Report*, CERN 95-02, Genève, Switzerland.
- [23] D. Acosta et al., *Nucl. Instr. and Meth.*, A(308):481 (1991)
- [24] A. N. Diddens et al., *Nucl. Instr. and Meth.*, A(178):27 (1980)
- [25] U. Amaldi, *Phys. Scripta* 23, 409
- [26] N. Akchurin et al., *Nucl. Instr. and Meth.*, A(408):380 (1998)
- [27] The CALICE Collaboration et al., *JINST*, 6 P07005 (2011)
- [28] N. Akchurin et al., *Nucl. Instr. and Meth.*, A(581):643 (2007)
- [29] D. Acosta et al., *Nucl. Instr. and Meth.*, A(308):481 (1991)
- [30] M. Albrow et al., *Nucl. Instr. and Meth.*, A(487):381 (2002)
- [31] N. Akchurin et al., *Nucl. Instr. and Meth.*, A(640):91 (2011)
- [32] N. Akchurin et al., *Nucl. Instr. and Meth.*, A(686):125 (2012)